

**LONG TERM BEHAVIOR OF HYGROTHERMALLY CONDITIONED
CONCRETE-FILLED FIBER-REINFORCED POLYMERIC TUBES
SUBJECTED TO AXIAL LOADS**

By

Victor Alexander Lammoglia Hoyos

A dissertation submitted in partial fulfillment of the requirements for the degree of

DOCTOR OF PHILOSOPHY

in

CIVIL ENGINEERING

UNIVERSITY OF PUERTO RICO
MAYAGÜEZ CAMPUS
2011

Approved by:

Arsenio Cáceres, Ph.D.
Member, Graduate Committee

Date

Ricardo R. López, Ph.D.
Member, Graduate Committee

Date

Paul Sundaram, Ph.D.
Member, Graduate Committee

Date

Felipe J. Acosta, Ph.D.
President, Graduate Committee

Date

Mario Rivera, Ph.D.
Representative of Graduate Studies

Date

Ismael Pagán Trinidad, M.S.C.E
Chairperson of the Department

Date

*To all my family,
especially to my parents, my brothers,
my sisters and my dear wife Jessica.*

ABSTRACT

This study evaluated the behavior of concrete filled FRP tubes (CFFT) subjected to moisture absorption condition. Accelerated aging by means of hygrothermal process was conducted to predict long-term mechanical behavior of FRP material. FRP coupons were submerged in water at three different temperatures: 30°C, 40°C and 50°C. The CFFT and the concrete cylinders were submerged in water only at 30°C. FRP was characterized by means of following tests: axial tension, axial compression, and hoop tension. The CFFT and concrete cylinders were tested under compression load only. FRP coupons, concrete cylinders and the CFFT were tested for the following exposure times: 0 (unaged), 30, 100, 300, and 500 days. Strength degradation of aged FRP, concrete and the CFFT was detected over the exposure period. Results for samples of FRP aged at 40°C and 50°C showed reductions in strength with respect of time between 20% to 30%. In contrast, samples of FRP aged at 30°C showed a less reduction in strength with respect of time of approximately 15%. Based on the Arrhenius assumption and the methodology developed by Barbero and Damiani, predictions were made for residual strength of the FRP after 1000 days of aging. Arrhenius methodology predicts an axial compression strength reduction of 22% and a hoop tensile strength reduction of 19% after 1000 days of aging in water at 30°C. Similarly, Barbero and Damiani methodology predicts a compressive strength loss of 25% for the FRP.

In order to predict the short and long-term response of concrete filled FRP tubes under axial compression load, 2D and 3D non-linear finite element models (FEM) were implemented. A surface contact was established between the concrete core and the FRP tube in both FE models to account for the possibility of separation. The non-linear concrete behavior was modeled using Drucker-Prager plasticity. The 3D FEM showed a better prediction with respect to the 2D model when compared with the experimental data. The FEM results for unaged specimens were obtained from a parametric study to evaluate the sensitivity of the response to the effect of the dilation angles. This procedure consists in using several dilation angles (δ) for the given friction angle in order to obtain the best axial and lateral response. The responses using three different dilation angles (δ) were practically the same for the 2D FEM, having all curves one on top of each other. The best friction angle (β) and dilation angle (δ) combination found using the 3D FEM was 53° and 5° for the axial and lateral response. Similarly, the FEM results for concrete filled FRP tubes after being submerged for 500 days in water were obtained. For this case the best friction angle (β) and dilation angle (δ) combination found was 53° and 50° respectively.

Additionally, close form solution models were evaluated, using the stress-strain model developed by Fam and Rizkalla for concrete filled FRP tubes. The model was modified to include the effect of the confining effectiveness, allowing its application not only to FRP tubes but also to FRP jackets.

RESUMEN

Este estudio evaluó el comportamiento de tubos de polímero reforzado con fibra (FRP) rellenos de hormigón sujetos a condiciones de absorción de agua. Envejecimiento acelerado por medio de un proceso higrotérmico fue conducido para predecir el comportamiento mecánico a largo plazo del material de FRP. Cupones de FRP fueron sumergidos en agua a tres diferentes temperaturas: 30°C, 40°C and 50°C. Los tubos de FRP rellenos de hormigón (CFFT), y los cilindros de hormigón fueron sumergidos en agua a 30°C solamente. El FRP fue caracterizado por medio de las siguientes pruebas: tensión axial, compresión axial, tensión circunferencial. Los CFFT y los cilindros de hormigón fueron probados bajo carga de compresión únicamente. Los cupones de FRP, los cilindros de hormigón, y los CFFT fueron probados para los siguientes tiempos de exposición: 0 (no envejecido), 30, 100, 300, y 500 días. Degradación de la resistencia a carga del FRP envejecido, del hormigón y de los CFFT fue detectada durante el tiempo de exposición. Los resultados de las muestras de FRP envejecido a 40°C y 50°C mostraron reducciones en su capacidad a carga con respecto al tiempo entre 20% a 30%. En contraste, las muestras de FRP envejecido a 30°C mostraron una menor reducción en su capacidad a carga con respecto al tiempo de aproximadamente 15%. Basado en las presunciones del modelo de Arrhenius y la metodología desarrollada por Barbero y Damiani, se realizaron predicciones para la resistencia residual del FRP después de 1000 días de envejecimiento. La metodología de Arrhenius predice una reducción de la capacidad a compresión de 22% y una reducción de la capacidad circunferencial de 19% después de 1000 días de envejecimiento en agua a 30°C. Similarmente, la metodología de Barbero y Damiani predice una pérdida de la capacidad a compresión de 25% para el FRP.

Con el fin de predecir la respuesta a corto y a largo plazo de los tubos de FRP rellenos de hormigón bajo carga axial, se implementaron modelos de elementos finitos en 2D y 3D. Una superficie de contacto fue establecida entre el núcleo de hormigón y el tubo de FRP en ambos modelos para tener en cuenta la posibilidad de separación. El comportamiento no lineal del hormigón fue modelado usando el modelo de plasticidad de Drucker-Prager. El modelo de elementos finitos en 3D mostró una mejor predicción con respecto al modelo en 2D cuando fue comparado con los datos experimentales. Los resultados de los modelos de elementos finitos para especímenes no envejecidos fueron obtenidos de un estudio paramétrico realizado para evaluar la sensibilidad de la respuesta al efecto del ángulo de dilatación (δ). Este procedimiento consiste en usar varios ángulos de dilatación (δ) para un ángulo de fricción (β) dado con el fin de obtener la mejor respuesta axial y circunferencial. La respuestas usando tres diferentes ángulos de dilatación (δ) fueron prácticamente las mismas para el modelo de elementos finitos en 2D, teniendo todas las curvas prácticamente una sobre la otra. La mejor combinación de ángulo de fricción (β) y ángulo de dilatación (δ) encontrado usando el modelo en 3D fue 53° and 5° para la respuesta axial y circunferencial. Similarmente, los resultados del modelo de elementos finitos para los tubos de FRP rellenos de hormigón sumergidos en agua por 500 días fueron obtenidos. Para este caso la mejor combinación de ángulo de fricción (β) y ángulo de dilatación (δ) encontrado fue de 53° y 50° respectivamente.

Adicionalmente, modelos aproximados fueron evaluados, usando el modelo de esfuerzo-deformación desarrollado por Fan and Rizkalla para tubos de FRP rellenos de hormigón. El modelo fue modificado para incluir el efecto de la efectividad de confinamiento, permitiendo su aplicación no solamente para tubos de FRP sino también para chaquetas de FRP.

ACKNOWLEDGMENTS

I would like to express my gratitude to my advisor, Dr. Felipe J. Acosta, for selecting me to participate in this project. His academic support has allowed me to attain a better understanding of composite materials. Also to Dr. Miguel Pando who help us to create this project. His support and collaboration in all the publications presented through this work was really helpful. In addition, I would like to thank the other members of my committee, Dr. Arsenio Cáceres, Dr. Ricardo López, and Dr. Paul Sundaram whom I have had the pleasure of also having as course instructors.

Dr. Jack Lesko of Virginia Tech contributed to this project in many ways including student support, materials, exchange opportunities, etc. I greatly acknowledge the unconditional collaboration from the Materials Response Group at Virginia Tech who collaborated in this study by sponsoring students to work in the project through the Summer Undergraduate Research Programs and the IGERT program in Macromolecular Science & Infrastructure Engineering.

A portion of this project was possible thanks to the financial contribution of the Puerto Rico EPSCoR Office through the Faculty Initiation Grant. Special thanks to Western Ready Mix and CEMEX who donated the concrete and time of their employees to help in the preparation of the concrete cylinders and the CFFRP specimens.

TABLE OF CONTENTS

ABSTRACT	III
RESUMEN	IV
ACKNOWLEDGMENTS	VI
CHAPTER 1	1
INTRODUCTION	1
1.1 INTRODUCTION.....	1
1.2 OBJECTIVES.....	4
1.3 ORGANIZATION OF THE DISSERTATION.....	5
CHAPTER 2	7
LITERATURE REVIEW	7
2.1 INTRODUCTION.....	7
2.2 MECHANICAL BEHAVIOR OF CONCRETE.....	7
2.2.1 Uniaxial Behavior.....	8
2.2.2 Biaxial behavior.....	9
2.2.3 Triaxial behavior.....	10
2.3 CONCRETE FILLED TUBES (CFT).....	11
2.4 CFFT FINITE ELEMENT MODELS.....	17
2.5 FRP DEGRADATION ISSUES.....	18
2.5.1 Degradation of glass fibers.....	21
2.5.2 Degradation of resin.....	22
2.5.3 Degradation of fiber/matrix interface.....	24
2.5.4 Models for predicting service lifetime.....	25

CHAPTER 3	28
EXPERIMENTAL PROGRAM	28
3.1 CONCRETE	30
3.2 FRP TUBE.....	32
3.3 CONCRETE FILLED FRP TUBES (CFFT)	37
 CHAPTER 4	 40
EXPERIMENTAL RESULTS AND DISCUSSION	40
4.1 CONTROL CONCRETE CYLINDERS	40
4.2 CHARACTERIZATION OF FRP TUBES	47
4.2.1 Moisture uptake.....	47
4.2.2 Burst test.....	51
4.2.3 Axial tension test	56
4.2.4 Axial compression test	59
4.3 FRP TUBES COMPRESSION TEST	64
4.4 CFFT COMPRESSION TEST	67
 CHAPTER 5	 75
DURABILITY AND LONG-TERM BEHAVIOR PREDICTION	75
5.1 MACRO-MECHANICAL LONG-TERM BEHAVIOR	75
5.2 MICRO-MECHANICAL LONG-TERM BEHAVIOR.....	80
 CHAPTER 6	 89
2-D NON-LINEAR FEM OF CFFT	89
6.1 INTRODUCTION	89
6.2 CONSTITUTIVE MODELING OF CONCRETE.....	89
6.2.1 Concrete constitutive model with softening.....	90
6.2.2 Concrete constitutive model with perfect plasticity	96
6.2.3 Drucker-Prager model in ABAQUS	97
6.3 FRP TUBE.....	101

6.4	CONCRETE FILLED FRP TUBES (CFFT)	101
6.5	RESULTS	103
CHAPTER 7		105
3-D NON-LINEAR FEM OF CFFT		105
7.1	INTRODUCTION	105
7.2	FRP TUBES MODELING	106
7.2.1	Hoop test	106
7.2.2	Axial test	108
7.2.3	FRP tube compression test	110
7.3	CONCRETE FILLED FRP TUBES (CFFT)	114
CHAPTER 8		120
CONFINEMENT MODEL OF CFFT		120
8.1	INTRODUCTION	120
8.2	FAM AND RIZKALLA (2001A) MODIFIED MODEL	124
CHAPTER 9		129
CONCLUSIONS.....		129
9.1	MAIN CONCLUSIONS.....	129
9.2	ORIGINAL CONTRIBUTIONS OF THIS DISSERTATION	133
9.3	RECOMMENDATIONS FOR FUTURE WORK	133
REFERENCES		135
APPENDIX A: CONCRETE CURVES.....		151
APPENDIX B: COMPOSITE BURST CURVES		153

LIST OF FIGURES

Figure 2-1: Response of concrete under compression loading.....	8
Figure 3-1: Experimental program.	28
Figure 3-2: Elaboration of control concrete cylinders.....	31
Figure 3-3: Instrumented concrete cylinders.....	31
Figure 3-4: Axial compression test of concrete cylinder.....	31
Figure 3-5: FRP tubes.....	32
Figure 3-6: Hoop tension test samples.	35
Figure 3-7: Hoop tension test fixture.....	35
Figure 3-8: Cut fixture for axial test samples.	36
Figure 3-9: Special curved grip.	36
Figure 3-10: ELSS fixture for compression test.....	37
Figure 3-11: Filling of FRP tubes with concrete.....	38
Figure 3-12: Curing of CFFT under laboratory ambient conditions.	38
Figure 3-13: Aging of CFFT in water at 30°C.	39
Figure 4-1: Strength of air cured concrete cylinders.	41
Figure 4-2: Compressive strength versus time for air and moist cured concretes.....	42
Figure 4-3: Baseline stress-strain curve for concrete.	44
Figure 4-4: Concrete average curves.....	44
Figure 4-5: Concrete average strength.....	45
Figure 4-6: Air cured concrete – submerged in water 24 hours before test.....	46
Figure 4-7: Average concrete Poisson’s ratios.	46
Figure 4-8: Moisture absorption curves for FRP tubes samples.....	48
Figure 4-9: Diffusion analyses at 30°C for FRP tubes samples.	50
Figure 4-10: Diffusion analyses at 40°C for FRP tubes samples.	50
Figure 4-11: Diffusion analyses at 50°C for FRP tubes samples.	51
Figure 4-12: FRP tube sample under hoop tension test.....	52
Figure 4-13: Baseline hoop tension stress-strain curve of the FRP tube.....	52
Figure 4-14: Average tension hoop strength at ambient conditions (not submerged).....	53
Figure 4-15: Degradation of tension hoop strength at 30°C.....	54
Figure 4-16: Degradation of tension hoop strength at 40°C.....	54
Figure 4-17: Degradation of tension hoop strength at 50°C.....	55
Figure 4-18: Summary of hoop strength degradation.....	55

Figure 4-19: Baseline axial tension stress-strain curves.....	57
Figure 4-20: Picture of baseline sample tested in axial tension.....	57
Figure 4-21: Comparison of the axial tension stress-strain curve of the FRP tubes.....	58
Figure 4-22: Degradation of axial tension strength at 30°C.....	58
Figure 4-23: Baseline axial compression stress-strain curve of FRP tubes.....	60
Figure 4-24: Picture of baseline sample tested in axial compression.....	61
Figure 4-25: Comparison axial compression stress-strain curve.....	61
Figure 4-26: Degradation of axial compression strength at ambient conditions.....	62
Figure 4-27: Degradation of axial compression strength at 30°C.....	62
Figure 4-28: Degradation of axial compression strength at 40°C.....	63
Figure 4-29: Degradation of axial compression strength at 50 °C.....	63
Figure 4-30: Degradation axial compression strength summary.....	64
Figure 4-31: Baseline axial compression stress-strain curve (tube 1).....	65
Figure 4-32: Baseline axial compression stress-strain curve (tube 2).....	66
Figure 4-33: Baseline axial compression stress-strain curve (tube 3).....	66
Figure 4-34: Typical Load-Strain Curves for CFFT.....	67
Figure 4-35: Example of failure modes of CFFT samples.....	69
Figure 4-36: Typical axial compression load-strain curve.....	70
Figure 4-37: Comparison of the behavior between CFFT and unconfined concrete.....	71
Figure 4-38: Baseline axial compression load-strain curve.....	71
Figure 4-39: Axial compression load-strain curve after being submerged in water for 30 days.....	72
Figure 4-40: Axial compression load-strain curve after being submerged in water for 100 days.....	72
Figure 4-41: Axial compression load-strain curve after being submerged in water for 300 days.....	73
Figure 4-42: Axial compression load-strain curve after being submerged in water for 500 days.....	73
Figure 4-43: Crushing and ultimate loads measured on CFFT.....	74
Figure 5-1: Shifted axial compression strength plot with fit line.....	77
Figure 5-2: Procedure to obtain the activation energy for the compression strength degradation.....	78
Figure 5-3: Shifted hoop strength plot with fit line.....	79
Figure 5-4: Procedure to obtain the activation energy for the hoop strength degradation.....	79
Figure 5-5: SEM image of unaged CFFT specimen.....	84
Figure 5-6: Axial stress at failure for ply 6.....	86
Figure 5-7: Predicted axial strength for ply 6 at different aging states.....	87
Figure 5-8: Shifted axial strength plot compared with Damiani methodology.....	87
Figure 6-1: Parameters of stress-strain curve of concrete.....	91

Figure 6-2: Damage threshold curve.	93
Figure 6-3: Comparison of experimental data and the analytical model.	94
Figure 6-4: Analytical curve for concrete with softening.	95
Figure 6-5: Analytical curve for concrete with perfect plasticity behavior.	96
Figure 6-6: Initial modulus for unaged concrete.	97
Figure 6-7: Yield surface in meridional plane for unaged concrete.	100
Figure 6-8: Drucker - Prager hardening curve.	100
Figure 6-9: Axisymmetric finite element mesh used for the concrete-filled FRP model.	102
Figure 6-10: FEM and experimental results for unaged concrete filled FRP tubes.	104
Figure 7-1: Ply stack plot from Abaqus.	105
Figure 7-2: Finite element mesh used for the Hoop test model.	107
Figure 7-3: Comparison of FEA and experimental results from axial hoop test.	107
Figure 7-4: Finite element mesh used for the axial test model.	108
Figure 7-5: Comparison of FEA and experimental results from axial tension test.	109
Figure 7-6: Comparison of FEA and experimental results from axial compression test.	110
Figure 7-7: Finite element mesh used for the FRP tube model.	111
Figure 7-8: Comparison of FEA and experimental results from FRP tube test.	112
Figure 7-9: Stress S1 on Ply 2 (8°) at experimental failure load.	112
Figure 7-10: Stress S1 on Ply 4 (8°) at experimental failure load.	113
Figure 7-11: Stress S1 on Ply 6 (8°) at experimental failure load.	113
Figure 7-12: Stress S1 on Ply 8 (8°) at experimental failure load.	113
Figure 7-13: Deformed shape at buckling load.	114
Figure 7-14: FRP tube mesh.	115
Figure 7-15: Concrete core mesh.	115
Figure 7-16: Comparison of FEA and unaged experimental results for CFFT.	118
Figure 7-17: Comparison of FEA and 500 days aged experimental results for CFFT.	118
Figure 8-1: Typical Load-Strain Curves for Concrete-Filled FRP Tube.	121
Figure 8-2: Compressive Strength of Confined Concrete.	122
Figure 8-3: Experimental unaged data and proposed model.	128
Figure 8-4: Experimental 500 days aged data and proposed model.	128
Figure A-1: 30 Days aged unconfined concrete.	151
Figure A-2: 100 Days aged unconfined concrete.	151
Figure A-3: 300 Days aged unconfined concrete.	152
Figure A-4: 500 Days aged unconfined concrete.	152

Figure A-5: Burst 10 days 30°C	153
Figure A-6: Burst 100 days base line.	153
Figure A-7: Burst 100 days 30°C	154
Figure A-8: Burst 100 days 40°C	154
Figure A-9: Burst 100 days 50°C	155
Figure A-10: Burst 300 days 30°C	155
Figure A-11: Burst 300 days 40°C	156
Figure A-12: Burst 300 days 50°C	156
Figure A-13: Burst 500 days base line	157
Figure A-14: Burst 500 days 30°C	157
Figure A-15: Burst 500 days 40°C	158
Figure A-16: Burst 500 days 50°C	158

CHAPTER 1

INTRODUCTION

1.1 Introduction

Fiber-reinforced polymer-matrix composite materials (also called fiber-reinforced polymers, FRP) have been utilized in small quantities in the building and construction industry for decades. However, because of the need to repair and retrofit rapidly deteriorating infrastructure in recent years, the potential market for using fiber-reinforced composites and for a wide range of applications is now being realized to a much greater extent. Numerous successful applications using fiber-reinforced polymer matrix composites in the construction industry, such as bridges, piers, building panels, walkways, pipelines and offshore structures, to mention only a few, have been reported in the literature (Holloway, 1990, Holloway, 1993, Eckold, 1994, Holloway and Head, 2001, Tuakta, 2005).

FRP composite systems appear to have a number of advantages when compared with traditional construction materials such as wood, steel and concrete. For example, steel-reinforced concrete piles can fail due to chloride attack on the reinforcing elements and concrete freeze/thaw degradation. Repairing costs of piling systems made with traditional materials in harsh marine environments have been estimated at over \$1 billion dollars annually (Lampo, et al., 1998).

FRP structural elements usually have thin-wall cross section due to their high tensile strength. However, because of their low modulus, such elements suffer from problems of local buckling and large deformations (Fardis and Khalili, 1981). By combining FRP with concrete, it is possible to build structural elements which have high strength in tension and compression and satisfactory overall stiffness and stability. An ideal form of an FRP concrete composite member is when the concrete is encased in the FRP.

The use of fiber reinforced polymer matrix composites in pressure retaining structures such as pressure vessels and piping systems has been confined mostly to low pressure applications. The reason for this limited use is mainly due to the uncertainty with respect to the long-term reliability of polymer matrix composites under moisture, temperature and multi-axial loading (Ellyin and Maser, 2004).

There is data currently available in the literature on concrete confined by FRP composites subjected to axial compression load. However, this data is largely restricted to carbon/epoxy composites and/or to concrete wrapped with FRP sheets. Although the effect of moisture on the performance of FRP has been a widely studied issue, only preliminary studies exist on long-term behavior of concrete filled FRP tubes (CFFT) (Pando, et al., 2002).

Available data in the literature on CFFT under axial compression load is still limited, and with few replicates. This project developed a multi-year experimental program to gather short-term and long-term sets of data. In order to allow the reliable prediction of the long-term behavior of CFFT, sufficient replicates were tested.

The long-term behavior of FRP is usually studied by means of aging testing. To reduce testing time even further, tests can be performed at elevated temperature and the degradation at these elevated temperatures can be measured resulting in a type of test known as accelerated degradation (Bank and Gentry, 1995).

The aging mechanisms in the case of an epoxy matrix composite are divided in two groups (Chateauminois, et al., 1994). The first group is related to aging processes which involve only molecular interactions between water and the epoxy network. This can result in a dramatic decrease in the thermo-mechanical properties of the composites (McKague, et al., 1978, Costa, et al., 2005). The second group involves macroscopic damage such as material cracking and fiber/matrix debonding related to hygrothermal effects (change in properties due to moisture absorption and temperature change).

When considering fiber/matrix debonding, reinforcement fibers become susceptible to direct environmental attack. In the case of glass fibers, such direct environmental exposure has been found to induce drastic losses of static properties due to stress corrosion mechanism (Kajorncheappungam, 1999, Khennane and Melchers, 2003). FRP structural members are susceptible to damage and failure under moist conditions. In recent years, several models to predict long-term behavior of FRP under moist conditions have been developed. These models usually correspond for specific fiber lay-up composites or for unidirectional fiber composites (Barbero and Damiani, 2003).

This research adopted the methodology developed by Barbero and Damiani (2003) to predict the long-term strength of unidirectional E-glass fiber composites subjected to hygrothermal exposure. This methodology was developed for FRP laminate axially loaded

in tension during the time of exposure. This research will study this methodology for FRP laminate axially loaded in compression after the time of exposure.

1.2 Objectives

The objective of this work is to evaluate long-term behavior of CFRP elements subjected to compressive loads focusing on the systems at the constituents level (FRP, Concrete, and the combination).

Specifically:

- Understand the behavior of CFFT under axial compression load based on experimental data and finite element models
- Evaluate long-term properties of submerged GFRP tubes in water at 30°C, 40°C, 50°C.
 - Obtain the diffusivity parameter of GFRP
 - Obtain the FRP residual strength (hoop & longitudinal) after 10, 30, 100 and 500 days of aging time.
- Evaluate long-term properties of submerged concrete infill
 - Track residual strength of concrete
- Evaluate long-term axial compressive behavior of submerged CFFT
- Evaluate influence of material variability
 - Use large number of replicates to obtain reasonable statistics

1.3 Organization of the Dissertation

The research is organized in this document through nine chapters. The first chapter is a general introduction to concrete filled FRP tubes showing how this system has been used and studied through recent years.

Chapter 2 reports a detailed literature review of the concrete filled FRP tubes (CFFT) starting with an introduction to the mechanical behavior of the concrete to understand its behavior under compression loads and confinement pressure. Following is the behavior of the CFFT by analyzing the experimental results obtained from different experimental and analytical studies. This chapter also reviews the finite element models (FEM) developed to understand and predict the behavior of these systems. Finally the FRP degradation issues are reviewed by analyzing the information from the literature that includes: degradation of glass fibers, degradation of resins, degradation of fiber/matrix interface and models developed to predict service life.

Chapter 3 includes a detailed summary of the experimental program developed. A 500 days test matrix was performed. The experimental results are presented and discussed in Chapter 4.

The macro and micro mechanical models were calibrated to predict the long-term behavior of the mechanical properties of the FRP tube based on the results obtained in the experimental program. This methodology and its results are documented in Chapter 5.

A 2D FEM was developed in this study as an initial approach to study the behavior of the CFFT system. In this case the non-linearity of the contact between the concrete core and the FRP shell was considered. The FRP was modeled as an equivalent orthotropic

layer in two orthogonal principal directions with linear elastic behavior. The methodology and the results are documented in Chapter 6.

Chapter 7 presents the 3D FE models performed but in this case the FRP shell was modeled as a laminate. The mechanical properties of each lamina were provided to the shell elements. This FE model also was used to predict the buckling load of the tube. The methodology and the results are documented.

The model developed by Fam (2000) for concrete filled FRP tubes (CFFT) is studied and modified in Chapter 8. The expression proposed by Mander, et al. (1988b) for confined concrete is updated, in order to include the effect of a continued confining pressure and the confining effectiveness in this model. Finally, in Chapter 9 the conclusions obtained are presented.

CHAPTER 2

LITERATURE REVIEW

2.1 Introduction

This chapter presents a literature review of concepts applied to the development of this work. These concepts include: mechanical behavior of the concrete under different loading states, a brief background on studies with concrete filled tubes, the use of fiber reinforced polymer (FRP) in civil infrastructures, and hygrothermal degradation of glass-fiber reinforced polymers.

2.2 Mechanical Behavior of Concrete

Concrete is a heterogeneous material composed of cement with the inclusion of stony aggregate. Its mechanical behavior is complex and it is influenced by formation and development of micro cracks in the mortar and in the interface between the mortar and the aggregate (Sih and DiTommaso, 1985). This cracking generates nonlinear and inelastic behavior, with hardening and later softening by strain due to the growth of distributed cracks that are grouped in bigger cracks up to producing failure. One of the most notable characteristics of this material is that its tensile strength is much smaller than the compression strength. This characteristic is attributed to the low tensile strength of the interface between the mortar and the aggregate.

2.2.1 Uniaxial Behavior

Before entering into the details of the studies, the behavior of concrete when subjected to compression is first described. Figure 2-1 shows a typical stress-strain curve of concrete subjected to compression load. The response of the concrete is essentially linear and elastic until the load reaches approximately 35 % of the peak strength. This response corresponds to a minimal stable crack growth in the transition zone between the aggregate and the cement paste.

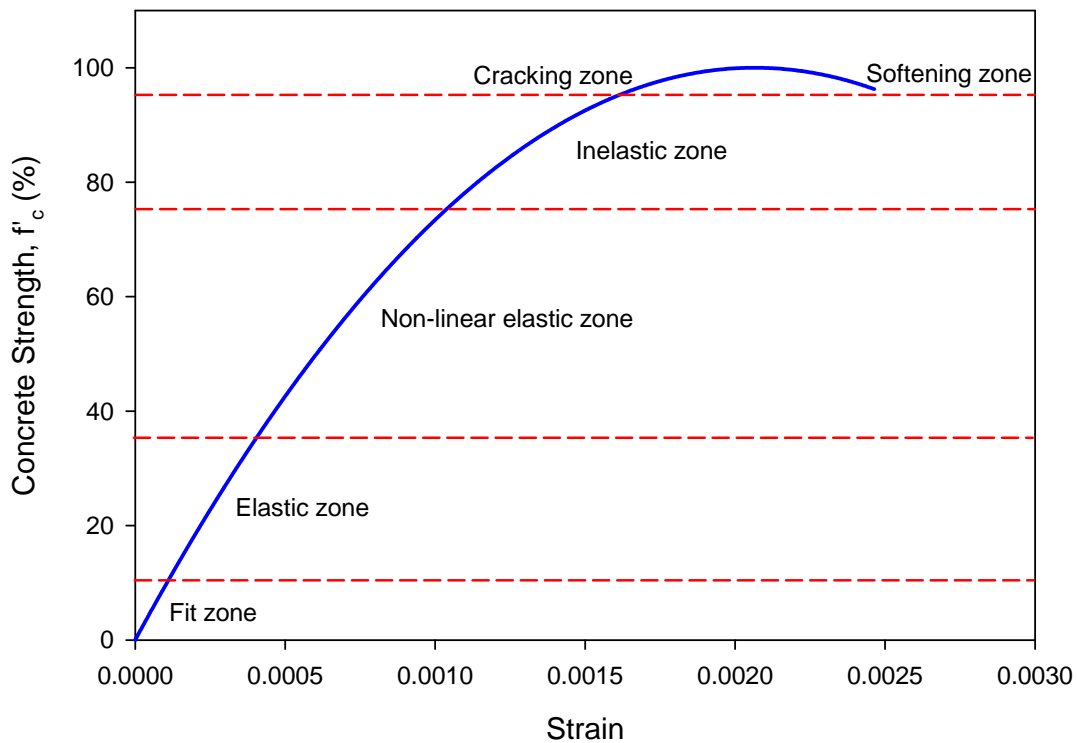


Figure 2-1: Response of concrete under compression loading

The loads that produce compressive stresses between 35 % and 50 % of the peak strength result in a small stiffness reduction of the material. This stiffness reduction results

from a significant increase in the initiation and growth of cracks in the transition zone. This crack growth is stable.

Compressive stresses between 50% and 75% of the peak strength produce additional stiffness reduction of the material. Here, the stiffness reduction is partly attributed to the initiation and growth of cracks in the transition zone and in the cement paste. The strains at this stage are recoverable.

The concrete loaded between 75 % and 95 % of its peak strength responds with permanent large deformations. This state is a consequence of the spontaneous crack growth in the transition zone and in the cement paste, and also by the consolidation of the micro cracks in continuous crack systems. In this zone, the stiffness loss is highly pronounced.

A decrease in stress with an increase in strain is observed once the peak strength is reached. This response, called softening, is the result of the development of multiple crack systems. The peak strength is reached for an axial strain value near 0.002. Also it is known that if the concrete strength is increased, its behavior will be more brittle (Neville, 1995).

2.2.2 Biaxial behavior

The behavior of concrete subjected to biaxial stress is different from the behavior of the concrete under a uniaxial stress. The strength of concrete subjected to biaxial compression may be up to 27 percent higher than the uniaxial strength of concrete. For equal compressive stress in two principal directions, the strength increase is approximately 16 percent (Kupfer, et al., 1969).

Results obtained by several investigators showed that the compressive stress at failure decreases as the simultaneously acting tensile stress is increased. The strength of the concrete under biaxial tension is approximately equal to its uniaxial tensile strength.

2.2.3 Triaxial behavior

Since the pioneering work of Balmer (1949) on strength of concrete under triaxial stress, many researchers have studied the behavior of confined concrete, especially over the last three decades (Kotsovos and Newman, 1978, van Mier, 1986, Wang, et al., 1987, Smith, et al., 1989, Bellotti and Rossi, 1991, Imran and Pantazopoulou, 1996, Li and Ansari, 1999). Generally, cylindrical specimens were loaded axially while subjecting them to constant lateral pressure in a triaxial cell. In most cases, cylinders with diameters of 100 mm or less have been used. Although the reported confining pressures are normally lower than the uniaxial compressive strength (f'_c) of the concrete, several researchers have used pressures up to $5f'_c$.

In triaxial states, failure is modeled by conical surfaces depicting the combinations of stress at which the specimen reached certain critical states (Pantazopoulou, 1995). For stress states in which the lateral confining stress is less than approximately 40% of the axial stress, failure is associated with tensile cracking and subsequent volume expansion (Chen and Han, 1988, Pantazopoulou and Mills, 1995). At the other end of the cone, failure may be closer to plastic flow (Smith, et al., 1989, Imran, 1994).

Several years ago, Sfer, et al. (2002) observed responses qualitatively and quantitatively similar to those of previous experimental studies, most of which used smaller test specimens. In this study the maximum load carrying capacity under axial

compression increases significantly with an increase in the confining pressure. At low confinement, the response exhibits a well-defined peak followed by a smoothly descending curve, while at higher confinement, the response was ductile, with a monotonically increasing load leading to a plateau.

In a similar manner to this research, Flores (2009) tested samples prepared from the same concrete batch used for this research to study the behavior of plain concrete under axial compression load at different levels of constant lateral confinement. Twenty-two mechanical property tests, four unconfined compression tests, and 18 triaxial compression tests, were performed.

One objective of the study performed by Flores (2009) was to determine the material parameters of the plain concrete such as cohesion intercept and angle of internal friction. These properties from ultimate compressive strength data at various confinement stresses were determined using the Mohr-Coulomb failure criterion. The Mohr-Coulomb failure envelope was graphically generated in the study performed by Flores. From the plot presented by Flores, an empirical angle of internal friction was determined to be approximately 34 degrees and a cohesion of approximately 435 psi was also measured. The triaxial compression tests exhibited a continuous increase in ultimate compressive stress and strain at failure with increasing confining stress.

2.3 Concrete Filled Tubes (CFT)

The improvement of the structural properties of the concrete filled tubes is caused by the composite action of its constituent elements. When the compressive longitudinal

strain increases applying compression, the lateral expansion of the concrete is restricted by the tube. Consistently, a radial pressure develops in the interface tube-concrete.

In this state, the concrete core is submitted to a state of triaxial stress and the tube to biaxial stress. Therefore, the corresponding load can be considerably larger than the separate sum from the strengths of the tube and concrete. An increase of strength caused by confinement effect on the concrete core by the tube depends on several factors, such as, thickness of the tube, slenderness ratio and cross section geometry.

In general, the concrete jackets interact with the concrete core in three forms: (1) confines the concrete core, therefore, it increases its compression strength and ductility, (2) provides additional shear strength, and (3) the adhesion between the two materials develops a composite action increasing the flexural strength of concrete. On the other hand, the concrete core helps to avoid buckling.

The first studies in the subject of concrete filled steel tubes was reported by Burr (1912). The carrying capacity was increased through the years with better concretes and thicker tubes (Faber, 1956, Stevens, 1959, Jones and Risk, 1963). Research works on concrete filled steel tubes increased considerably in the last decades because of the need to rapidly repair and retrofit deteriorating infrastructure (O'Shea and Bridge, 2000, Susantha, et al., 2001, Ellobody and Young, 2006, Ellobody, et al., 2006, Teng, et al., 2007, Han, et al., 2008). Most of these studies were carried out on concrete filled thick tubes.

Most of the confinement models used to predict the stress-strain behavior of the confined concrete with steel tubes came from models that originally were developed for confined concrete with steel stirrups (Mander, et al., 1988a, Razvi and Saatcioglu, 1999).

However, these models overestimate the compressive capacity of the system compared with experimental data of confined concrete with steel tube (Samaan, 1997).

The advances in composites materials allowed the development of fiber reinforced polymers (FRP) with several structural properties superior to steel (ACI, 1996, Seible and Karbhari, 1996). These materials have been used successfully in many industries, such as, aerospace, automotive, shipbuilding, among other.

However, the civil engineering community has only recently begun to recognize its advantages, which it is evident from the large number of publications and the growing number of conferences on the topic (Karbhari and Seible, 2000, Lopez-Anido, et al., 2000, Bakis, et al., 2002, Nystrom, et al., 2003) and from the efforts that are dedicated to the development of design norms, especially in the U.S.A. (i.e. ACI, Committee 440, Fiber Reinforced Polymer Reinforcement).

Recently, several types of FRP materials are considered for rehabilitation of concrete structures; the most used are glass-fiber reinforced polymers (GFRP), carbon-fiber reinforced polymers (CFRP), and aramid-fiber reinforced polymers (AFRP).

FRP can be used to confine columns of concrete thus incrementing its compression capacity and ductility (Katsumata, et al., 1987, Priestley, et al., 1992, Saadatmanesh, et al., 1994, Karbhari and Gao, 1997, Larralde, 1997, Mirmiran and Shahawy, 1997, Di Tomaso and Ghinelli, 1998, Saafi, et al., 1999, Toutanji, 1999, Xiao and Wu, 2000). These materials are a new alternative due to their durability when compared with conventional materials. FRP used as reinforcement in concrete structures, such as columns, has increased in Europe, Japan, and the U.S.A. (Katsumata and Kimura, 1990, Kasei, 1993, Picher, et al., 1996).

Proposed expressions to estimate the strength and deflections of concrete confined with FRP is limited due to its inherent anisotropy. Expressions based on models developed for concrete with lateral steel reinforcement results generally in poor comparison between the experimental results and predictions, especially for deflections (Karbhari and Gao 1997) and in many cases have been shown to overestimate the capacity leading to unreliable design (Mirmiran and Shahawy, 1997).

Diverse systems of jackets have been developed and validated in laboratory and field conditions (Matsuda, et al., 1990, Priestley and Seible, 1991, Seible and Priestley, 1993, Xiao, et al., 1996, Xiao and Ma, 1997). In the United States the systems have been used in bridge piles, walls, beams, and slabs (Nanni and Gold, 1998, Karbhari and Seible, 1999). In Canada, they have been used in buildings and bridge foundation piles, and beams (Neale and Laboussi re, 1998, Rizkalla and Laboussi re, 1999). In Japan, they have been used in bridge slabs, tunnels, oil refineries, buildings, chimneys, marine structures, retaining walls, and foundations (Nanni, 1995, Emmons, et al., 1998, Shehata, et al., 1998, Fukujama, 1999). Finally, in Europe, it has been applied to buildings, bridge piles, highways viaducts, and highway bridge beams (Nanni, 1997, Burgoyne, 1999, Taerwe and Matthys, 1999).

Experimentally the concrete filled FRP tubes have been studied using glass and carbon fibers principally, but with different tube thickness, slenderness ratios and cross section geometry. Table 2-1 presents a summary of the sizes of concrete filled FRP tubes studied recently. In most cases, the strength of the concrete used oscillate between 15 and 50 MPa with wraps of 2 or 3 layers of fiber (Nanni, et al., 1994, Picher, et al., 1996, Larralde, 1997, Mirmiran and Shahawy, 1997, Miyauchi, et al., 1997, Di Tomaso and

Ghinelli, 1998, Saafi, et al., 1999, Toutanji, 1999, Xiao and Wu, 2000) although, a concrete strength of 60 MPa was used by Harmon, et al. (1995) and Harmon, et al. (1998) with tubes of 50 x 100 mm.

Table 2-1: Sizes of concrete filled FRP tubes studied recently.

<i>Size (mm)</i>	<i>Study by</i>
50 x 100	Harmon, et al. (1995) and Harmon, et al. (1998)
75 x 152	Larralde (1997)
76 x 305	Toutanji (1999)
100 x 200	Miyauchi (1997) and Fam (2000)
150 x 300	Nanni, et al. (1994), Picher, et al. (1996), Mirmiran and Shahawy (1997), Di Tomaso and Ghinelli (1998), Xiao and Wu (2000).
152.4 x 435	Saafi, et al. (1999)
168 x 336, 219 x 438	Fam (2000)

The literature also shows data from tested concrete confined with fiber-glass with 9 layers (Fam, 2000) and up to 14 layers (Mirmiran and Shahawy, 1997). Most of these studies are for tubes of 150 mm by 300 mm (Nanni, et al., 1994, Picher, et al., 1996, Mirmiran and Shahawy, 1997, Di Tomaso and Ghinelli, 1998, Xiao and Wu, 2000).

Also there are analytic confinement models that confirm increment in strength and ductility of concrete confined with FRP (Fardis and Khalili, 1981, Karbhari and Eckel, 1993, Cusson and Paultre, 1995, Mirmiran and Shahawy, 1997, Miyauchi, et al., 1997, Samaan, et al., 1998, Saafi, et al., 1999, Spoelstra and Monti, 1999, Fam and Rizkalla, 2001b, Teng and Lam, 2004, Moran and Pantelides, 2005, Saenz and Pantelides, 2007). Most of this confinement models came from models originally developed for confined concrete with steel stirrups such as the models developed by Richart, et al. (1928) and

Mander, et al. (1988b) principally. A good comparative study of these models is presented in the work by De Lorenzis and Tepfers (2003).

The analysis of these works permits the establishment of different confinement responses in concretes of low and high strength; the confinement effect is more notable on concretes with low strength. Several studies have employed some of the proposed expressions in the literature with varied success; however, they all coincide in finding similar tendencies (De Lorenzis and Tepfers, 2003, Teng and Lam, 2004).

A recent work carried out by Bruneau and Marson (2004), studied the behavior of concrete filled steel tubes by modeling the steel tubes behavior as a bilinear relationship and the concrete core using seven different concrete axial compression stress-strain models. They are: 1) confined concrete model proposed by Mander, et al. (1988a); 2) unconfined concrete model proposed by Hognestad (1951); 3) confined concrete model suggested by Saatcioglu and Razvi (1992); 4) unconfined concrete model with high ductility; 5) unconfined concrete model from the Canadian Institute of Steel Constructions provisions (Marson and Bruneau, 2000); 6) unconfined concrete model with high ductility from the Canadian Institute of Steel Constructions provisions; and 7) equivalent to model 1 but with arbitrarily reduced confined concrete strength.

According to Bruneau and Marson (2004), the compressive capacity of these systems is overestimated if the strength of the concrete is increased beyond f'_c due to confinement provided by the tube. However, it is conservative if models for unconfined concrete are used. The best results are obtained if the ultimate strength of the concrete is used even for large deformations. This last approach is essentially an elastic-perfectly

plastic model, where the plastic portion results from the confinement provided by the tube. Similar results were obtained by Patsch et al. (2002).

2.4 CFFT Finite Element Models

A nonlinear finite element model with non-associative Drucker-Prager plasticity was implemented by Mirmiran, et al. (2000) to account for restrained pressure sensitivity of concrete. A database from 152.5 by 305 mm cylindrical specimens with three different tube thickness of 1.45, 2.21, and 2.97 mm, with 6, 10 and 14 plies of GFRP, respectively, and with concrete strengths between 80 and 115 MPa was used.

All specimens were grooved at 19 mm from both ends to ensure that they acted only as hoop tension band. For this reason in the FEM the elastic modulus of the FRP was set close to zero in the axial direction. The concrete core was modeled using the Drucker-Prager with elastic-perfectly plastic assumption. Good correlations between the predicted stress-strain curves and the experimental results were obtained, using a zero dilatancy angle.

A perfect bond between the concrete core and tube was assumed for the FE model in a recent work carried out by Ruiz, et al. (2004). For this purpose each of the nodes of the concrete core surface was constrained to have the same value of displacement of the closest point on the tube surface. Good correlations between the predicted curves and experimental results were presented using a zero dilatancy angle and high Poisson's ratios (0.49 and 0.45) for the concrete.

Dávila, et al. (2006) developed a model similar to Ruiz, et al. (2004) but in this case the FE model was calibrated with their own experimental data. Good correlations

between the predicted curves and their experimental results were presented using a zero dilatancy angle and realistic Poisson's ratios for the concrete. To achieve these results the initial concrete modulus was decreased from the experimental results.

2.5 FRP Degradation Issues

Research activity on durability of FRP has been extensive in recent years, and a large number of projects are now in progress in many parts of the world. A part of this activity has been focused on evaluating the effect of environmental degradation on the mechanical properties of the composite and its constituents. Another part has been focused on developing models to predict the long-term behavior of the composites. The present section presents a brief literature review on these two issues.

Reviews of the environmental effect on the long-term durability of fiber reinforced polymeric composites have been given by Schutte (1994) and Liao, et al. (1998). These review articles discuss various aspects, including matrix degradation, fiber degradation, fiber/matrix interface debonding, and temperature and liquid media effect on the composite durability during service life.

The effect of moisture on the performance of FRP for construction has been a widely studied issue. Often the combination of moisture and elevated temperature is used to accelerate the diffusion and reaction with the composite materials or to determine the synergistic effect of moisture and temperature (Bank and Gentry, 1995). Regarding the degradation influenced by water, Glass-FRP (GFRP) is studied because of the susceptibility of glass fibers to water damage (Bank and Gentry, 1995).

Several problems are known to be associated with the presence of water in resins. Moisture can act as a plasticizer in the resin and cause breakage of Van der Waals bonds between the polymer chains (Bank and Gentry, 1995). This can cause considerable changes in modulus, strength, strain to failure, and toughness. These effects may be reversible, but the swelling stresses induced by moisture uptake can cause permanent damage such as matrix cracking, hydrolysis and fiber-matrix debonding (Hayes, et al., 1998).

Hayes et al. (1998) measured a reduction of approximately 26% in tensile strength and Young's modulus for a glass/vinyl ester system after wet/dry cycles at 45°C for 30 days. However, the damage did not appear to accumulate during the following 30-day period. The initial damage was not recovered when the material was dried suggesting that there was permanent damage to the matrix or fiber. Furthermore, the fatigue life of the wet material was reduced by a factor consistent with the reduction in its quasi static strength; i.e. the dry and wet (cyclical stress, S , cycles to failure, N) the fatigue $S-N$ curves possessed the same slope but different intercepts. This conclusion is considered to be of significant importance for simplifying predictive models, as it may be possible to predict the fatigue response of a material saturated at a specific equilibrium moisture condition by simple reduction in quasi-static properties.

Another investigation by Hayes, et al. (1998) refers to a considerable decrease in fatigue life CFRP specimens which were first preconditioned in 80°C deionized water for two months. Degradation of the matrix was considered to be the main cause of the deterioration. When dry, Carbon-FRP (CFRP) specimens were subjected to fatigue cycles in a water cell at 80°C, It was found that the fatigue life increased compared to the control specimens in dry environment. Even for Aramid-FRP (AFRP) specimens, the fatigue life

was found to increase. This was attributed to an increase in matrix ductility and a decrease in the interfacial strength between fibers and the matrix. In addition, one CFRP system also showed an increase in tensile strength.

In another investigation by Bank, et al. (1998), E-glass/vinyl ester rods were immersed in water at temperatures of 23 to 80°C for up to 224 days. At 40 and 80°C, the flexural strength was reduced by 86% and 55%, respectively of the virgin strength. At 23°C no significant reduction was measured after the exposure time. In contrast to the flexural strength, shear was not dramatically influenced. This property was measured using the “*Short Beam Shear Strength Test –D2344*” (ASTM, 2006), which is not a direct shear test. The flexural modulus of the specimens did not appear to be affected by the time of exposure. This was attributed to the fact that the modulus, in contrast to the strength, is insensitive to localized deterioration. An increase in the glass transition temperature (T_g) was detected for the specimen in the 80°C exposure but not at the lower temperatures.

Steckel, et al. (1998) conducted moisture exposure tests on four CFRP and three GFRP systems (systems for column over wrapping). For the GFRP systems, the tensile strength was reduced by approximately 10% after 1000 hours and 15% after 3000 hours, at 38°C and 100% RH, indicating a decreasing deterioration rate with respect to time. One carbon/epoxy system had up to 35% reduction in short beam shear strength and a significant reduction in T_g associated with the moisture absorption. The other systems studied were unaffected by the exposure.

In a study reported by Porter and Barnes (1998), FRP specimens were exposed to air at 100% RH at different temperatures for 200 days. The tensile strength of an E-glass/vinyl ester system was reduced by 40% and 25% at 93°C and 23°C, respectively. The

flexural and tensile modulus for these specimens decreased approximately by 10% for both temperatures.

Pantuso, et al., (1998) conducted durability studies on a glass fiber/polyester rod. After 60 days of 30 wet/dry cycles at 23°C, the Young's modulus and tensile strength were reduced by 7% and 10%, respectively. In addition, a change in failure mode, with tendency to longitudinal delamination, could be observed after the exposure period.

Vinyl ester and polyester films immersed in distilled water at ambient temperature for 54 days did not show any significant reduction in tensile strength in the study reported by Chin, et al., (1997).

2.5.1 Degradation of glass fibers

E-glass (E for electrical grade) is the most widely used general-purpose form of composite reinforcement. It has good mechanical properties and is available at a relatively low price. E-glass contains boric acid (B_2O_3) and aluminates (Al_2O_3), which increase the resistance to water but also increase the susceptibility to acid and alkali degradation (Adams, 1984). Hence corrosion of E-glass at a relative high rate can be expected outside the pH range of 5 to 8.

Corrosion of glass can generally be classified into two processes: etching and leaching. These processes may occur separately or in combination (Adams, 1984). Etching is usually caused by an alkali attack which destroys the silica network. Leaching usually occurs in the presence of an acid solution.

Stress rupture (or static fatigue) is the process that leads to delayed failure in a material subjected to a constant load. Although stress rupture may cause fiber failure at

stresses considerably lower than the ultimate tensile strength, the strength of the fiber (as measured in a short-term test) is usually completely retained until just a short time before stress rupture occurs. The failure is caused by the growth of a crack perpendicular to the direction of the fiber (Charoenphan, et al., 2004). Stress rupture of glass fibers has been shown to occur in shorter times if moisture and water are present in the surroundings of the glass (Metcalf and Schmitz, 1972).

2.5.2 Degradation of resin

The preferred resin type for FRP applications are polyester, epoxy and vinyl ester, which are all thermosetting resins. This section presents several aspects about the durability of resins and their importance in the durability of the FRP composites.

Ferrier and Hamelin (2002) showed that the durability of FRP materials essentially depends on the polymer quality, therefore, a study of resin systems is critical for the durability the FRPs. Polyester resins are characterized by low cost, good mechanical properties, good weathering resistance but less resistance to alkaline environments than epoxy and vinyl ester. Epoxies have better resistance than polyesters to alkalis but cost 2 to 5 times as much. Vinyl esters have the backbone of an epoxy resin but the curing mechanism of polyester. Vinyl ester is known to have good chemical resistance and is often used for chemical storage tanks and pipes (Sheard, 1997).

Resin matrices respond initially to chemical diffusion by delamination, swelling, cracking and plasticization with considerable reductions in their modulus, strength and toughness. Some of these changes (plasticization and swelling) can be reversible (Schutte, 1994, Hayes, et al., 1998). At longer times, chemical reactions occur between the diffused

materials and the polymer structure of the resin system (Lemasçon, et al., 1996). If the temperature range is high, there is a possibility that physical degradation may occur as well. The effect of these physical and chemical degradation mechanisms can be assessed through only a few available mechanical and physical test methods.

Physical degradation of the resin systems may be due to high temperature or moisture exposure. High temperatures, especially when they are very close to the glass transition temperature of the matrix, may cause a thermodynamic imbalance. This results in “free volumes”, which can be filled by other molecules as the polymer attempts to reach an equilibrium stage. Physical degradation occurs during this process that results in changes in the mechanical properties of the materials (Mijovic, 1985, Tuttle, 1996).

Absorbed moisture can cause plasticization of the matrix, which is defined as the reduction of the mechanical properties and glass transition temperature, resulting from the interruption of Van Der Waals bonds between the polymer chains (Wolff, 1993, Bank and Gentry, 1995). Also, absorbed moisture is believed to increase the effective free volumes in the resin system, causing more physical degradation (Buck, et al., 1998). Since the glass transition temperature of polymer matrices is a function of the strength of the chemical bonds existing in the polymer structure and also the amount of free volumes, it can be used to monitor the physical degradation in the resin system due to moisture absorption or chemical diffusion which can damage the bond in the polymer structure.

It has been shown that T_g is a physical property of thermosetting resins. Exposure of the resin to elevated temperatures for short durations increases the T_g , causing additional cross-linking between the polymer chains and making the bond between them stronger. This process is called “postcuring”. T_g values can be used to determine if the postcuring

exists or not. The fact that additional chemical reactions occur between the unreacted groups may also increase T_g . The rate of change of T_g increases with time and temperature (Mijovic and Lin, 1985).

2.5.3 Degradation of fiber/matrix interface

The interface is a heterogeneous region between the homogenous matrix material and the fibers. It is approximately one micrometer thick (Bank and Gentry, 1995). The interface between the fiber and polymer matrix must have good adhesion since it is at a very critical location where the transfer of stresses occurs. Also a strong interface is necessary to develop the composite mechanical properties.

Studies of the characteristics of the interface region conclude that the interface region may possess features such as a finite dimension or thickness, elastic or inelastic response, a degree of anisotropy, bond strength associated with adhesion to the fibers, bond strength associated to the matrix and elastic modulus, coefficient of thermal expansion, Poisson's ratio and cohesive strength (Jayaraman, et al., 1994, Subramanian, et al., 1995).

Although the influence of water and stress on the interfacial region is not fully understood, results of modeling studies suggest that water and swelling stresses and conditions of fatigue (due to stress transfer) will have a significant influence on the strength of the interfacial region (Balmer, 1949, Jayaraman, et al., 1994).

The interface is usually the weak link in the failure of composites (Schutte, 1994). d'Almeida (1991) stated that the weak interface in combination with a wet environment can degrade easily and it is very critical whenever the composite mechanical properties are

dominated by the matrix and/or the interface properties, e.g. in interlaminar shear or transverse tension. The following damage mechanisms that can be observed in interface region degradations (Bradshaw and Brinson, 1997) are: matrix osmotic cracking, and interfacial debonding. These may be induced by differential swelling or by osmotic cracking at the interface and delamination.

2.5.4 Models for predicting service lifetime

To predict the service lifetime of the composites, many mathematical models and test methodologies have been proposed in the literature. All of these mathematical models are just simple mathematical fits to experimental data and use only a relationship between performance, age, and the accelerating variables without getting into the details of the mechanistic models of the degradation. Unfortunately, no atomistic model that relates the molecular scale changes to mechanical properties of the material has been proposed yet.

Arrhenius model is the most used method to analyze the short-term data from accelerated testing. The primary assumption of this model is that the single dominant degradation mechanism of the material will not change with time and temperature during the time of exposure, but the rate of degradation will be accelerated with the increase in temperature.

The most notable application of the Arrhenius concept to civil engineering materials was by Litherland, et al. (1981). In order to estimate the service lifetime of glass-fiber reinforced cement materials, both experimental and analytical components were studied. The work performed by Litherland, et al. (1981) has served as example for other research based on Arrhenius models.

Aindow, et al. (1984) showed that long-term aging predictions of glass reinforced cement (GRC) based on accelerated tests correlated well with real weather aging environments at different locations around the world.

Pritchard and Speake (1987) examined the kinetics of water absorption in polyester resin and glass fiber-reinforced laminates over a temperature range, which included the matrix glass transition temperature (T_g), which was calculated to be 74 °C. They showed that water absorption parameters follow an Arrhenius relationship. Using this relationship and building empirical relationships between the strength loss and the water absorption by curve fitting, the authors concluded that satisfactory predictions for mechanical properties could be made even for much lower temperature ranges. They also showed that experimental data obtained over three years at the lower end of temperature range fit very well the predicted values using the model developed.

Cáceres, et al. (2000) developed another prediction model based on an experimental program by finding a method for correlation and extrapolation of accelerated aging data to estimate the long-term behavior of GFRP materials. The authors used the Arrhenius concept to predict the long-term properties based on short-term measurements of those properties by the use of shift factors. One of the accelerated data sets was selected as a reference set and all other data sets of different temperatures were superimposed on this reference set by shifting along the time axis. In this way, a master curve at the same temperature of the reference curve was obtained.

Barbero and Damiani (2003) developed a time and environment dependent model to predict degradation of tensile strength of unidirectional E-glass fiber composite. That is based on curve-fit of data available in the literature. These include static fatigue, zero stress

aging (reduction of strength when no stress is applied during the time of exposure to a given environment), interface aging, and moisture dependent matrix stiffness. They recommended performing a more extensive series of static fatigue, zero-stress-aging, and debonding length tests in order to further verify the model.

As was shown in this chapter, short term structural behavior of Concrete Filled FRP Tubes (CFFT) is reasonably well studied. But on the other hand, although the effect of moisture on the performance of FRP has been a widely studied issue, only preliminary studies exist on long-term behavior of CFFT (Pando, et al., 2002).

CHAPTER 3

EXPERIMENTAL PROGRAM

Experimental and analytical components were studied to connect well documented strength loss of the FRP tubes to long-term axial capacity of concrete filled FRP tubes (CFFT).

The Experimental program was divided in two parts (see Figure 3-1), axial compression test of CFFT and concrete cylinders were carried out at UPRM facilities, and the FRP tubes characterization under hygrothermal aging was developed at Virginia Tech facilities. The laboratory testing was performed for the following exposure times: 0 (unaged), 10, 30, 100, 300, and 500 days.

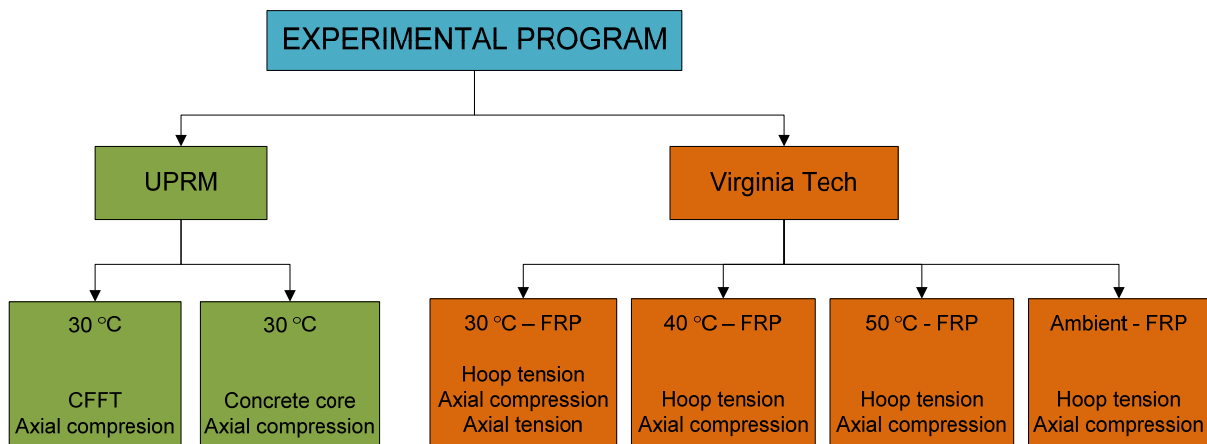


Figure 3-1: Experimental program.

The accelerated aging by means of hygrothermal process was conducted to predict long-term mechanical behavior of FRP material. For this purpose, the FRP tubes were submerged in water at three different temperatures: 30, 40 and 50 °C and the CFFT and concrete cylinders were submerged in water at 30°C only. Table 3-1 shows the test matrix that includes the total number of replicas for each test.

Table 3-1: Test matrix for CFFT, concrete cylinder and FRP material aging study.

Test	Days of Aging					
	0	10	30	100	300	500
CFFT 30°C Water Aging	10	0	10	10	10	10
Concrete Cylinders Aged in Water	0	0	5	5	5	5
Concrete Cylinders Air Aged	5	0	0	0	0	0
Composite 30°C, Water Aging						
Hoop Tension	5	5	5	5	5	5
Axial Tension	25	10	10	10	10	10
Axial Compression	25	10	10	10	10	10
Composite 40°C, Water Aging						
Hoop Tension	0	5	5	5	5	5
Axial Compression	0	5	5	5	5	5
Composite 50°C, Water Aging						
Hoop Tension	0	5	5	5	5	5
Axial Compression	0	5	5	5	5	5
Composite Baseline (Ambient aged)						
Hoop Tension	0	5	5	5	5	5
Axial Compression	0	5	5	5	5	5

3.1 Concrete

Normal weight concrete was used in this research. The maximum size of the aggregate used in the concrete mix was 6 mm (¼ in) crushed stone. Tetragard AS20, a shrinkage reducer admixture from BASF, was incorporated in the mix to reduce the separation of the concrete core and the FRP tube due to drying shrinkage and also to maintain the core and the FRP tube edges flush.

One hundred standard size cylinders (152 mm by 305 mm) of the same concrete were fabricated to be tested simultaneously with the CFFT. Both, concrete cylinders and CFFT, were cured under ambient conditions and then submerged in water at 30°C only (compared with the FRP) to be tested at the scheduled test plan. All the samples were tested at the following schedule: unaged (baseline), 30, 100, 300, and 500 days. Figure 3-2 shows the elaboration process of the control concrete cylinders at UPRM facilities.

The average measured compressive strength of the concrete cylinders was about 17 MPa, and a Poisson's ratio of 0.2. Concrete cylinders were instrumented with four strain gauges of 2 inches of length, two oriented in the axial direction and two in the hoop direction located at opposite sides.

The concrete cylinders were sanded and then cleaned in the location of the gauges. A layer of epoxy resin was applied over the cleaned area; it was sanded carefully to obtain a smoother layer in order to install the gauges. A photo of instrumented concrete cylinders is shown in Figure 3-3. The instrumented concrete cylinders were tested in axial compression with speed load control. Figure 3-4 shows a cylinder ready for testing.



Figure 3-2: Elaboration of control concrete cylinders.

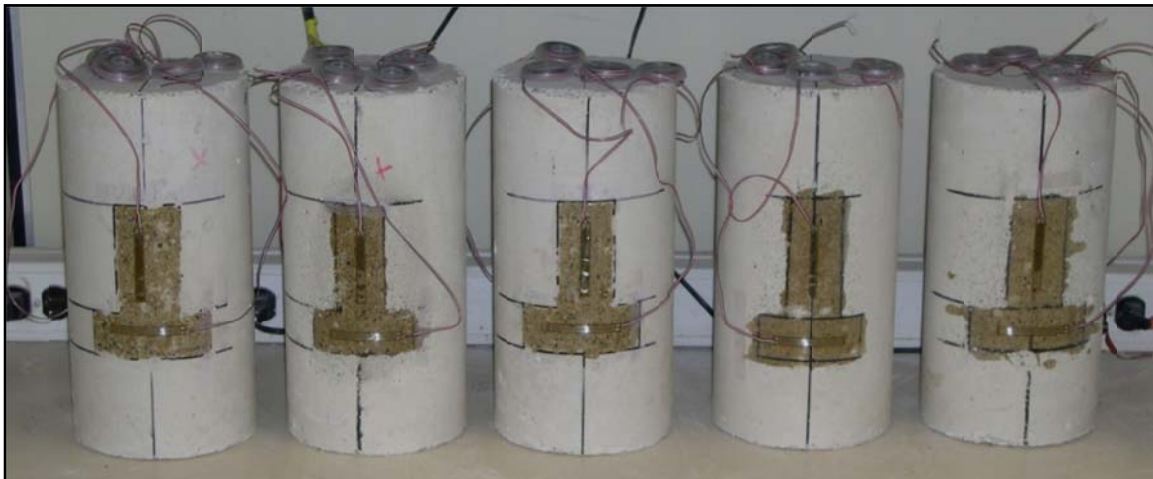


Figure 3-3: Instrumented concrete cylinders.



Figure 3-4: Axial compression test of concrete cylinder.

3.2 FRP Tube

FRP tubes used in this research and shown in Figure 3-5 are commercially available from Ameron International Fiber Glass Pipe Group. According to a datasheet provided by the manufacturer, the outside diameter is 168 mm (6.63 in) with an inside diameter of 162 mm (6.39 in) and a wall thickness of 3.0 mm (0.119 in). The tubes are filament wound, composed by E-Glass fiber, epoxy resin (Shell Epon 826) with hardener (Ancamine DL 50) mixed with Ethacure 100 (Davila, 2008).



Figure 3-5: FRP tubes.

The fiber is oriented in the following pattern $[-88 / 8 / -88 / 8 / -88 / 8 / -88 / 8 / -88]$. The zero direction is parallel to the tube axis. The micro-mechanical composition of the FRP tubes is shown in Table 3-2. This composition was obtained by means of burn out test (Davila, 2008).

Table 3-3 shows the mechanical properties computed for each layer of the FRP tube using micromechanical models (Rule of mixture and elasticity models), where E_i is the Young's modulus along axis i , G_{ij} is the shear modulus in direction j on the plane whose normal is in direction i , and ν_{ij} is the Poisson's ratio that corresponds to a contraction in direction j when an extension is applied in direction i .

Table 3-2: FRP tube composition, adapted from (Davila, 2008).

Layer	Thickness		Volume fraction	Angle
	(%)	(mm)	(%)	
liner	8.6	0.26	3.14	-
1	12.8	0.38	29.71	88°
2	14.8	0.44	26.94	8°
3	16.8	0.50	56.14	88°
4	5.9	0.18	70.44	8°
5	11.5	0.35	51.32	88°
6	5.4	0.16	77.90	8°
7	7.6	0.23	83.17	88°
8	7.7	0.23	51.90	8°
9	8.8	0.26	73.99	88°

Table 3-3: Theoretical properties of each lamina.

Layer	E_1^*	E_2^*	ν_{12}	G_{12}^*	G_{13}^*	G_{23}^*
0	--	--	--	--	--	--
1	23880	6962	0.33246	1722.49	1722.49	2023
2	21974	6528	0.33690	1660.84	1660.84	1924
3	42106	13163	0.29018	2667.08	2667.08	3499
4	51965	19599	0.26730	3792.29	3792.29	5181
5	38783	11647	0.29789	2424.60	2424.60	3126
6	57108	24937	0.25536	4862.46	4862.46	6708
7	60742	30225	0.24693	6073.17	6073.17	8357
8	39183	11817	0.29696	2451.42	2451.42	3167
9	54412	21896	0.26162	4235.93	4235.93	5822

*Units: MPa.

The measured glass transition temperature (T_g) in FRP coupons was 170°F by means of DMA analysis using a frequency of 1 Hz. The tubes were subsequently post-cured and cut into test specimens. The post-curing consisted of a 4-hour heat treatment at 180°F, and it was

undertaken in an attempt to minimize material property changes as a result of advancing cure of the matrix (Cain, et al., 2006a).

To characterize the FRP tubes, samples were cut axially and cylindrically from composite cylinders typical of those used as CFFTs. Compression strengths in the axial direction and tension strength in the hoop direction were measured for samples for three different water temperatures (30°C, 40°C, and 50°C). The measures were taken periodically over the course of a 500 day test. All tests of this research were carried out with sufficient repetitions to develop reasonable statistics.

Three aging temperatures (30°C, 40°C, and 50°C) were used to develop Arrhenius acceleration factors for long term predictions. To assess changes in mechanical properties and strength under hygrothermal loading required as input to the analytical models, the FRP was characterized by means of following tests: Axial Tension (ASTM, 2000b), Axial Compression (ASTM, 1995), and Hoop Tension as described below.

Short cylindrical samples of 25.4 mm (1 in) along the cylinder axis (Figure 3-6) were used for hoop tension tests, in which a specially-designed fixture shown in Figure 3-7 allows the sample to be loaded outward radially to simulate an internal pressure load. For further details on this fixture please see Cain, et al., (2006b). The traditional split disk tension test (ASTM, 2000a) can induce bending stresses while applying tension. The new fixture used provides a realistic testing method without having to perform a full size burst test.



Figure 3-6: Hoop tension test samples.

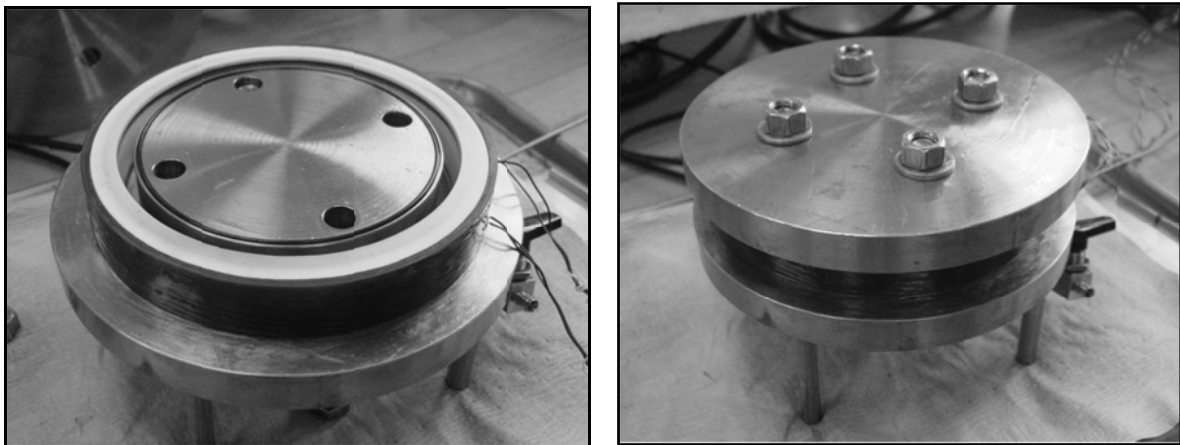


Figure 3-7: Hoop tension test fixture.

Axial tension specimens, which were 25.4 mm (1 in) wide (measured across the outside edges of the cylindrical section) and 165.1 mm (6.5 in) long, were cut from the cylinders using a custom fixture that allowed for cuts to be made in the plane of the centerline of the cylinder (Figure 3-8). The curved shape of the specimen necessitated special grip inserts which allowed them to be gripped in the loading frame without introducing unwanted bending moments (Figure 3-9).



Figure 3-8: Cut fixture for axial test samples.



Figure 3-9: Special curved grip.

Axial compression specimens were cut in a similar manner to the axial tension tests, but were sized 12.7 mm (0.5 in) wide and 139.7 mm (5.5 in) long. The samples were end-loaded, with a gage length of 12.7 mm (0.5 in), in compression using an End-Loaded Side-Supported (ELSS) fixture manufactured by Wyoming Test Fixtures, Inc (Figure 3-10).

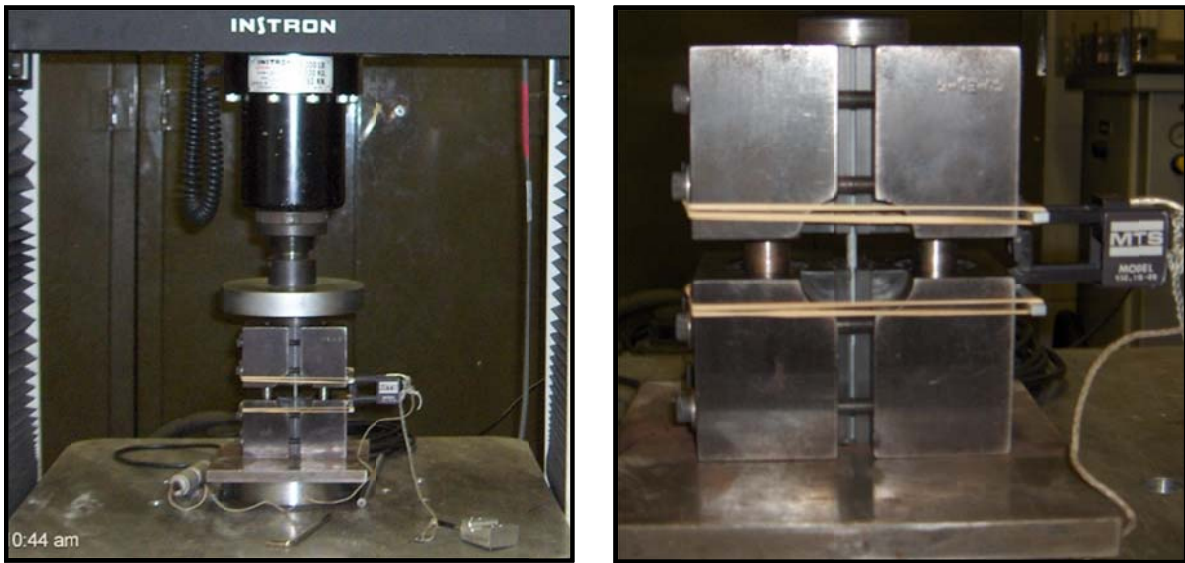


Figure 3-10: ELSS fixture for compression test.

3.3 Concrete Filled FRP Tubes (CFFT)

One hundred concrete filled FRP tubes (CFFT) of the same concrete were fabricated. Both, concrete cylinders and CFFT, were cured under ambient conditions and then submerged in water at 30°C to be tested later following the schedule. Standard procedures to fill the tubes with the same concrete batch were carried out. In order to allow moisture diffusion into the concrete, the end of the CFFT was not sealed.

Figure 3-11 to Figure 3-13 show the elaboration and curing process of the CFFT at the UPRM facilities.

CFFT were aged in water after the air curing period to prevent unrealistic aging of the concrete (Figure 3-13). The aging fluid was maintained at 30°C (held slightly above ambient temperature) to ensure a uniform aging temperature with time. No special treatments were made to the cylinder ends to allow saturation of the FRP as well as the concrete.

Sanding of the CFFT ends was carefully performed to level the surfaces prior to testing. The axial compression test on CFFT was carried out ensuring centricity of load. Instrumentation included three sets of axial and hoop strain gauges locations to allow corrections due to centricity of load.



Figure 3-11: Filling of FRP tubes with concrete.



Figure 3-12: Curing of CFFT under laboratory ambient conditions.



Figure 3-13: Aging of CFFT in water at 30°C.

CHAPTER 4

EXPERIMENTAL RESULTS AND DISCUSSION

This chapter presents the experimental results from tests described in Chapter 3 in Table 3-1. The results presented initially are from compression tests of control concrete cylinders, followed by those from the tests developed to characterize the FRP, and finally the results from compression tests on concrete filled FRP tubes (CFFT).

4.1 Control Concrete Cylinders

Normally, moist curing consists of a continuous storage of samples in a moist room with a nominal temperature of 23°C and 100% relative humidity. On the other hand, air curing normally consists of moist curing for seven days followed by an indoor storage at nominal temperature between 21°C and 24°C with a relative humidity of 50% (ASTM, 2007). In this research the air cured concrete cylinders and the concrete filled tubes (CFFT) were stored indoor for six months approximately at an ambient temperature near 30°C with a relative humidity between 70% and 90% as reported by the National Weather Service.

The strength of concrete is traditionally characterized by the 28 day value. However, strength of concrete is expected to increase with time at a continuously diminishing rate as long as there is moisture and unhydrated cement.

Unaged concrete cylinders cured in air were tested at 7, 28 and 155 days. The average strength obtained from five air cured concrete cylinders at 28 days was 12.8 MPa, reaching compression strength near to 17 MPa at 155 days. Concrete cured for 155 days was used as baseline.

Additionally, in order to verify the long-term strength of the air cured concrete, three control cylinders were tested at 900 days. Figure 4-1 shows a continuous increase in the compression strength of the unaged concrete through time.

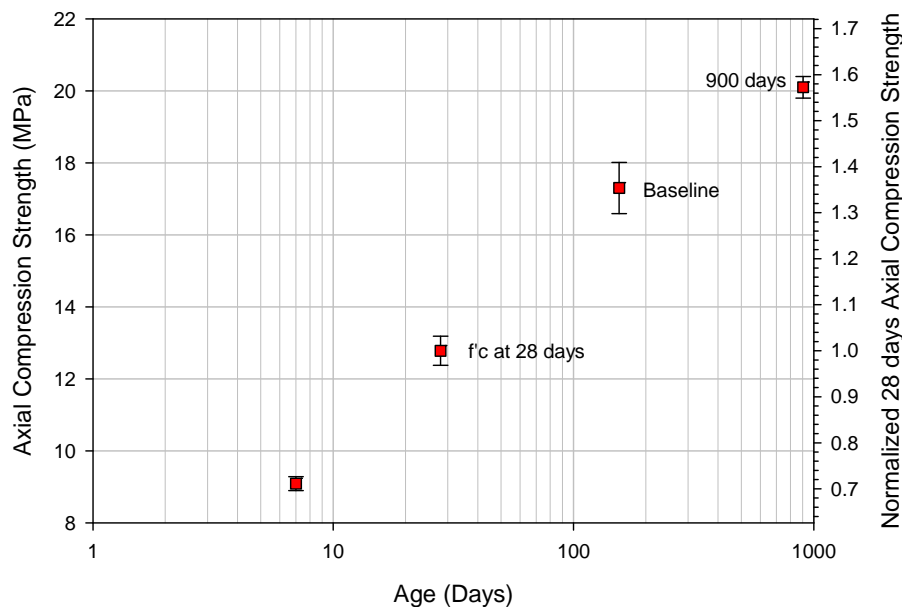


Figure 4-1: Strength of air cured concrete cylinders.

Although the strength gain obtained for the concrete after 900 days is high, it is still within normal ranges. Similar results were obtained by Lange (1994) for long-term strength of concrete under different environmental conditions. Figure 4-2 shows the axial compression strength results obtained by Lange (1994) for air and moist cured concrete cylinders.

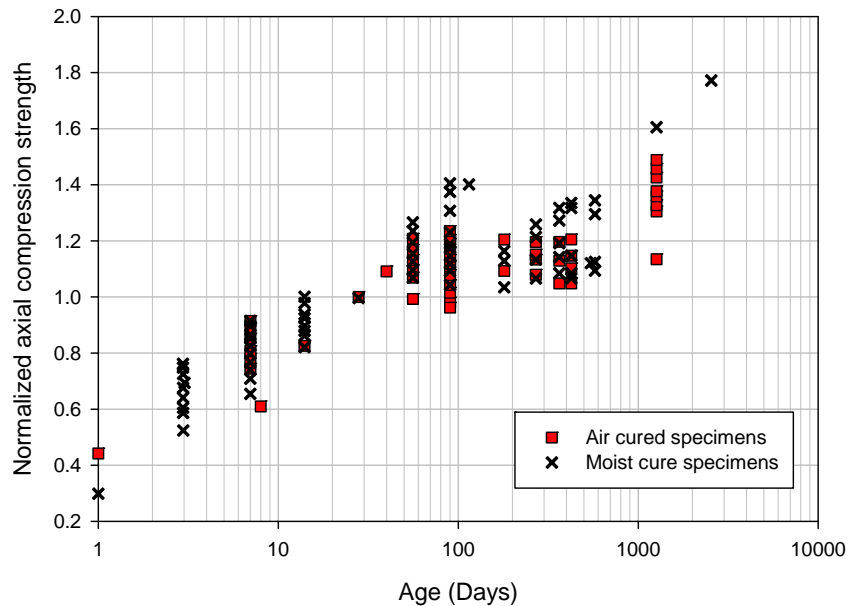


Figure 4-2: Compressive strength versus time for air and moist cured concretes. Adapted from Lange, (1994).

After 155 days of air cured time, the concrete cylinders and the concrete filled FRP tubes (CFFT) were submerged in water at 30°C. Five concrete cylinders randomly chosen were instrumented and then tested at four different submerged ages (30, 100, 300 and 500 days). These tests were performed at UPRM facilities.

The concrete cylinders and the concrete filled FRP tubes (CFFT) were tested under compression after about 155 days of air cured time. These results were used as baseline values. Compression test results from the baseline samples are summarized in Table 4-1. The stress-strain curves obtained for these samples are shown in Figure 4-3.

The concrete modulus was calculated from the slope of the axial stress-strain curve between 50 micro-strains and 40% of the concrete strength (ASTM C469). Baseline concrete reaches the peak strength near 0.003 (mm/mm) of axial strain. The peak strength was reached

for values between 0.0018 and 0.0025 for aging concretes submerged in water at 30°C. All these strain values are considered typical for a normal weight concrete (ACI 318-05).

Table 4-1: Baseline concrete properties.

Property	Average	Standard Deviation
Compressive strength (MPa)	17.30	0.71
Peak axial strain	0.0030	0.0002
Initial modulus (MPa)	14282	512

Additionally, the compression test results for the aged concrete are summarized in Table 4-2. Figure 4-4 compares the average stress-strain curves obtained for baseline and aging concrete compression tests. The complete concrete curves obtained from the compression tests are available in the Appendix A.

Table 4-2: Aged concrete properties.

Property	30 days		100 days		300 days		500 days	
	Average	SD	Average	SD	Average	SD	Average	SD
Compressive strength (MPa)	15.53	0.26	15.78	0.58	13.98	0.86	14.35	0.51
Peak axial strain	0.0024	0.0005	0.0025	0.0003	0.0020	0.0004	0.0016	0.002
Initial modulus (MPa)	15176	899	14754	236	14444	1898	15567	1334

Submerged concrete after a prolonged air cured period showed a minor compression strength gain when compared with the baseline cylinders, although both types of concrete reached strength values over f'_c as seen in Figure 4-5. This strength reduction has been attributed to the formation of secondary ettringite (Day, 1992, PCA, 2001) but this phenomenon is still under study.

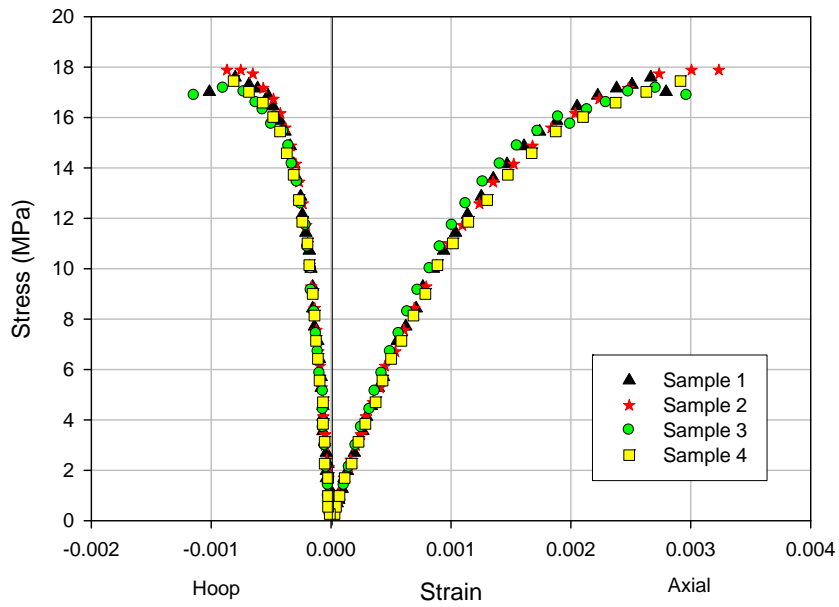


Figure 4-3: Baseline stress-strain curve for concrete.

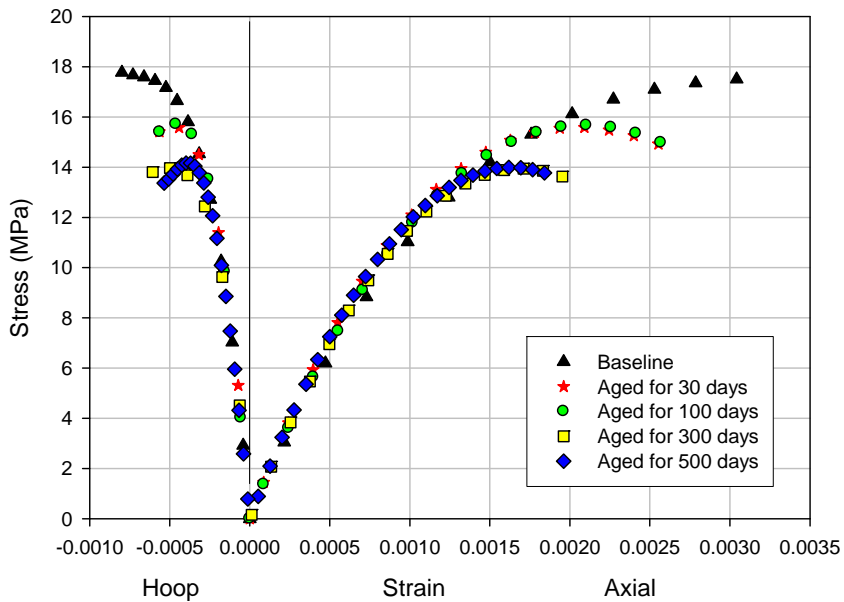


Figure 4-4: Concrete average curves.

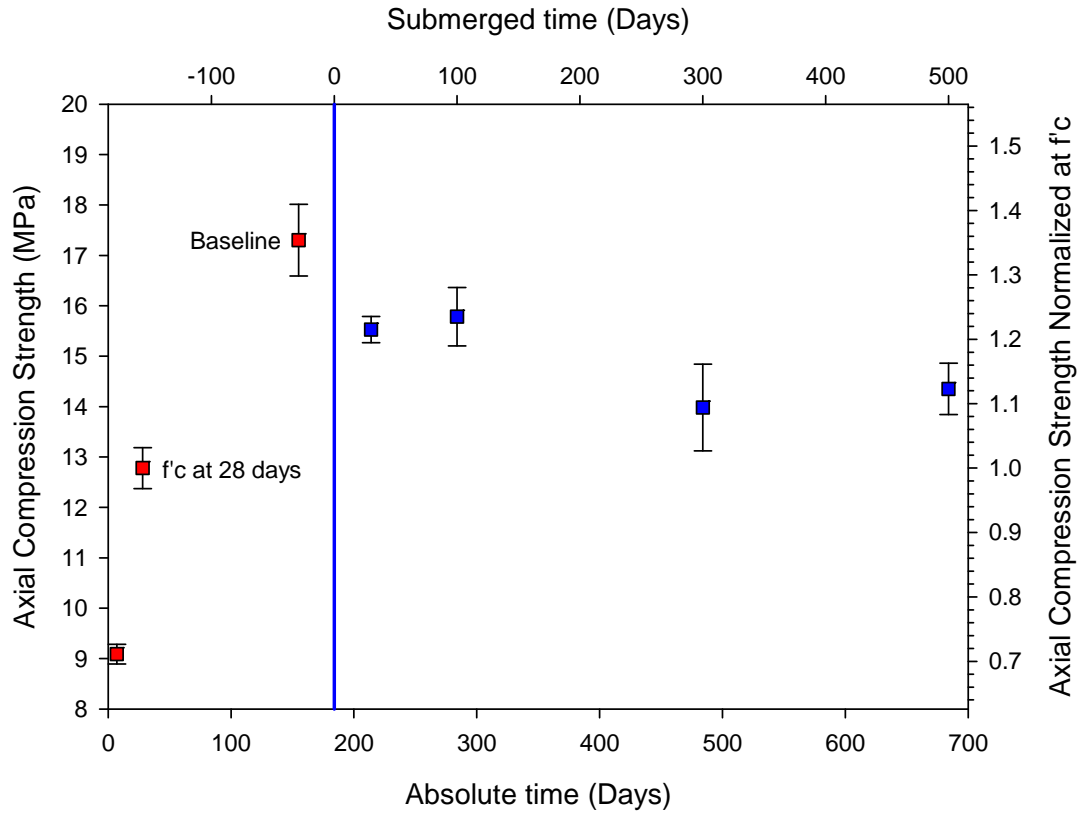


Figure 4-5: Concrete average strength.

Long-term concrete strength was studied by Wood (1992). Results from more than 6500 concrete specimens cured under different conditions and tested at ages between 1 day and 34 years are presented by Wood (1992). The results obtained by Wood (1992) for air cured concrete but submerged in water few hours prior to testing are presented in Figure 4-6. The results obtained by her show a similar behavior to the results presented in Figure 4-5.

Additionally, Figure 4-7 shows the average Poisson's ratios for baseline concrete and aging concrete submerged in water at 30°C. Baseline concrete (unaged) has an initial Poisson's ratio of 0.2, which is a normal value.

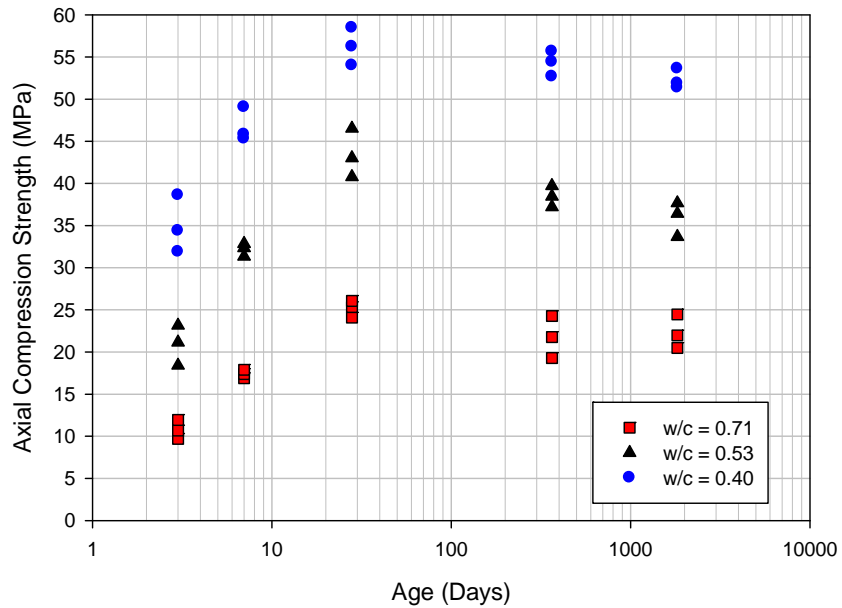


Figure 4-6: Air cured concrete – submerged in water 24 hours before test. Adapted from Wood (1992).

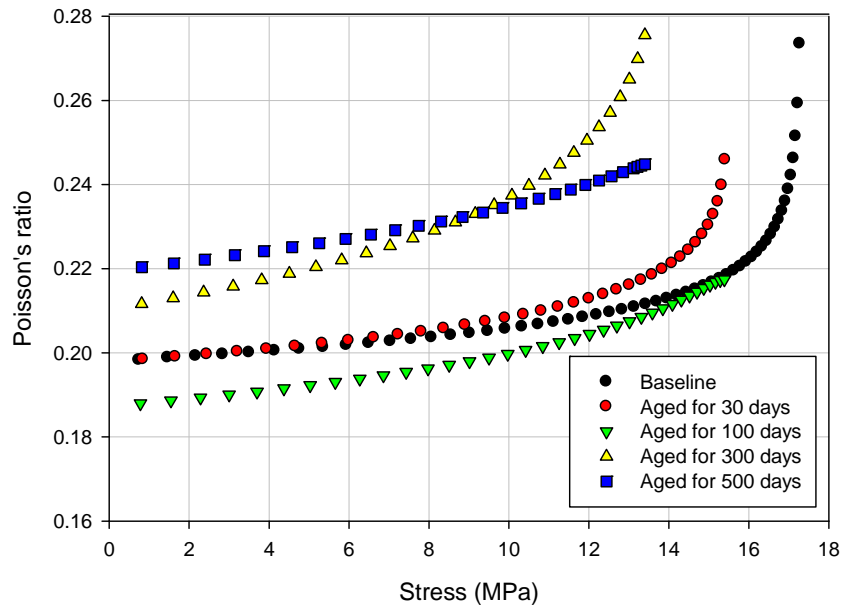


Figure 4-7: Average concrete Poisson's ratios.

4.2 Characterization of FRP Tubes

Test results for the FRP samples are presented in this section. The characterization of the FRP tubes was performed at Virginia Tech facilities. Strength degradation of FRP tubes subjected to hygrothermal conditions for extended periods of time was detected.

4.2.1 Moisture uptake

The effect of moisture on the performance of FRP for construction has been a widely studied issue (Otto, 1965, Rao, et al., 1981, Theocaris, et al., 1983, Wolff, 1993, Hayes, et al., 1998, Roy, et al., 2001, Fam, et al., 2002, Abdel-Magid, et al., 2005, Ray, 2005). Often the combination of moisture and elevated temperature is used to accelerate the diffusion and reaction with the composite materials or to determine the synergistic effect of moisture and temperature (Bank and Gentry, 1995).

In this section, strength degradation influenced by FRP water uptake is the principal mechanism studied because previous studies have shown the susceptibility of FRP to water damage (Rao, et al., 1981, Barton and Greenfield, 1986, Harper and Naeem, 1989, Schutte, et al., 1994, Hayes, et al., 1998, Roy, et al., 2001).

Average moisture uptake measurements for the FRP over approximately 200 days are shown in Figure 4-8. Over this period, saturation was not reached. However, it was estimated from a Fickian diffusion model. The Fickian diffusion model is commonly used to predict moisture absorption of composite materials due to reasonable estimates.

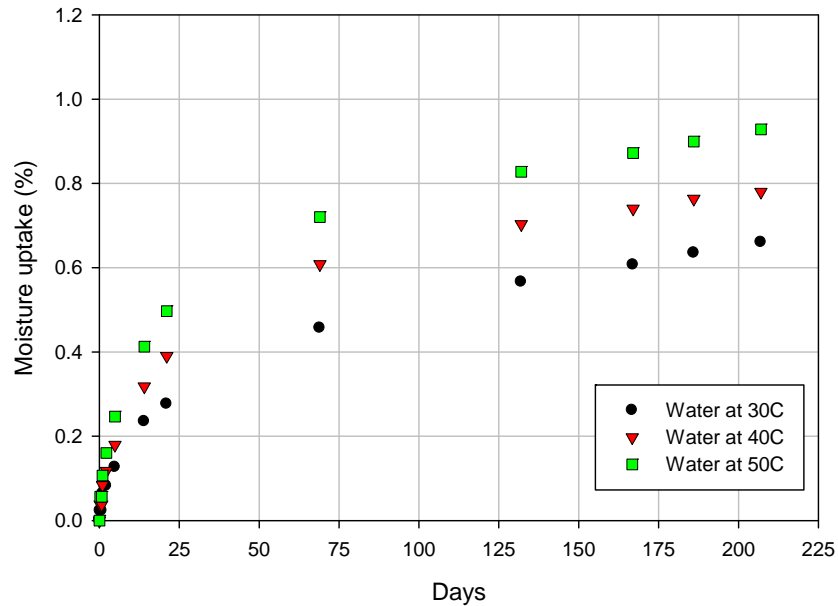


Figure 4-8: Moisture absorption curves for FRP tubes samples.

The Fickian model assumes (Shen and Springer, 1976):

- Constant diffusivity (D_x)
- A value for saturation moisture (M_{MAX}). It can be estimated to best fit the model to the experimental data if saturation state has not been reached.
- One dimensional problem. When the material is exposed to the environment on one side only, or on two parallel sides.
- Initial uniform temperature and moisture distributions inside the material
- Constant environment moisture and temperature

The expression for Fickian diffusion of a thin plate of thickness, h , during both adsorption and desorption is given by the following expression (Shen and Springer, 1976).

$$M = M_{MAX} \left[1 - \exp \left(-7.3 \left(\frac{D_x \cdot t}{h^2} \right)^{0.75} \right) \right] \quad [4.1]$$

where:

M = moisture content of the FRP specimen at submergence time, t

M_{MAX} = moisture content at saturation

t = time of submergence

D_x = diffusivity through the thickness of the FRP specimen

h = thickness of FRP specimen

Curve fitting using the Fickian model were performed using the experimental moisture absorption data gathered for the FRP. The fitted curves for moisture absorption at water temperatures of 30°C, 40°C, and 50°C are presented in Figures 4-9 to 4-11. The diffusion coefficient D_x and the saturation moisture content M_{MAX} obtained by the use of Fickian diffusion model are summarized in Table 4-3. An increase in the saturation moisture due to an increase in the water temperature was observed.

Table 4-3: Fickian diffusion parameters of the FRP tube.

Water temperature (°C)	Diffusivity, D_x (mm ² /day)	Saturation Moisture, M_{MAX} (%) ⁽¹⁾
30	0.011	0.70
40	0.014	0.80
50	0.016	0.95

Note: (1) Did not stabilize at the end of test, the showed value is predicted using Fickian model.

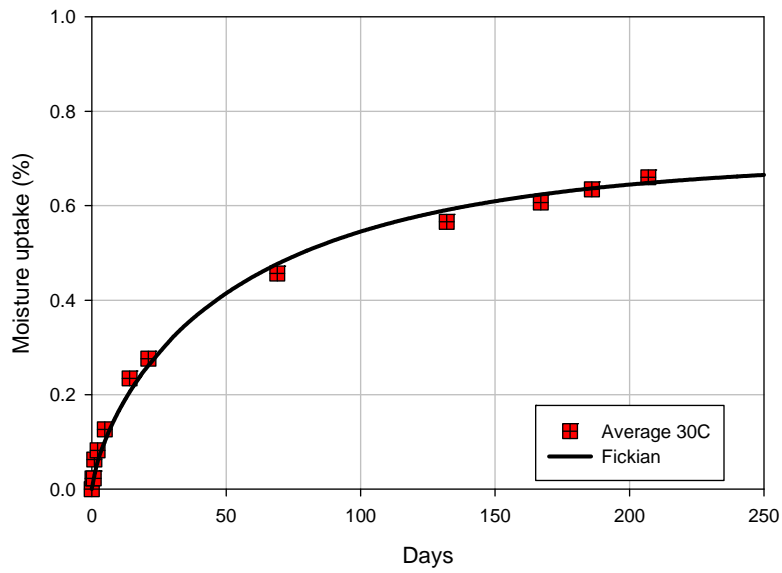


Figure 4-9: Diffusion analyses at 30°C for FRP tubes samples.

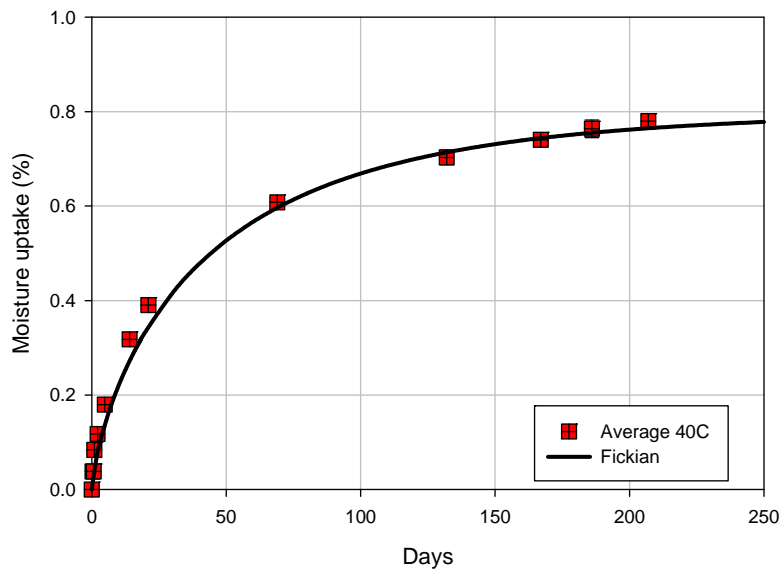


Figure 4-10: Diffusion analyses at 40°C for FRP tubes samples.

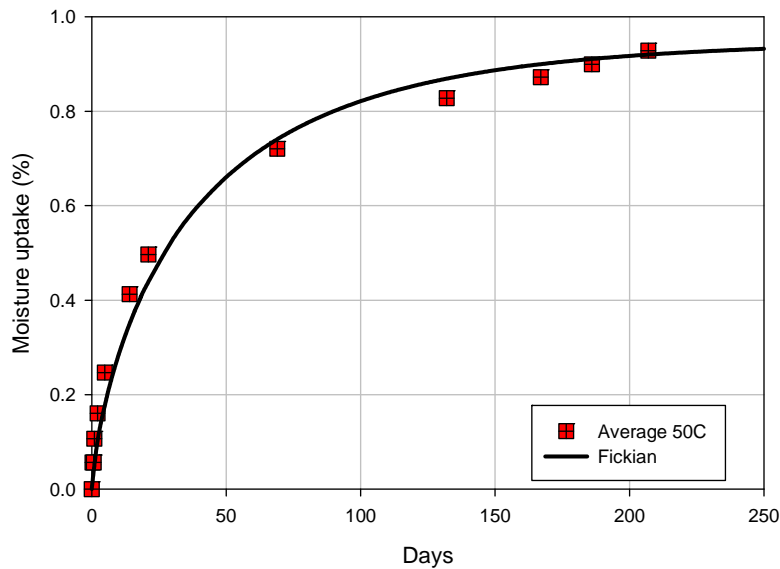


Figure 4-11: Diffusion analyses at 50°C for FRP tubes samples.

4.2.2 Burst test

To study the durability and long-term performance of FRP composite piles, it was necessary to establish the baseline mechanical properties of the FRP shell. The baseline properties are those obtained for the unaged FRP. The mechanical properties of the FRP tube were obtained using a new test fixture presented in Chapter 3. An example of a baseline sample under hoop tension test is presented in Figure 4-12. The hoop tensile properties obtained for the FRP are summarized in Table 4-4. The stress-strain curves obtained from tests are shown in Figure 4-13.

Table 4-4: Baseline hoop tensile properties of the FRP tube.

Property	Average	SD
Tensile strength (MPa)	390.27	42.84
Peak strain	0.0160	0.0022
Initial modulus (MPa)	26221	3216

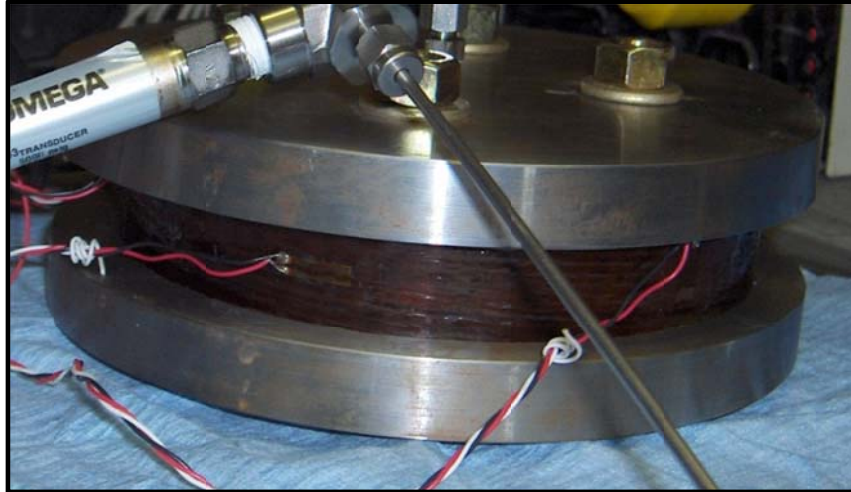


Figure 4-12: FRP tube sample under hoop tension test.

Figure 4-14 shows data from samples not submerged in water after 1, 100 and 500 days in a semi-logarithmic graph. Additionally, the strength normalized to the baseline strength is reported. The hoop strength is relatively unchanged through the 500 days.

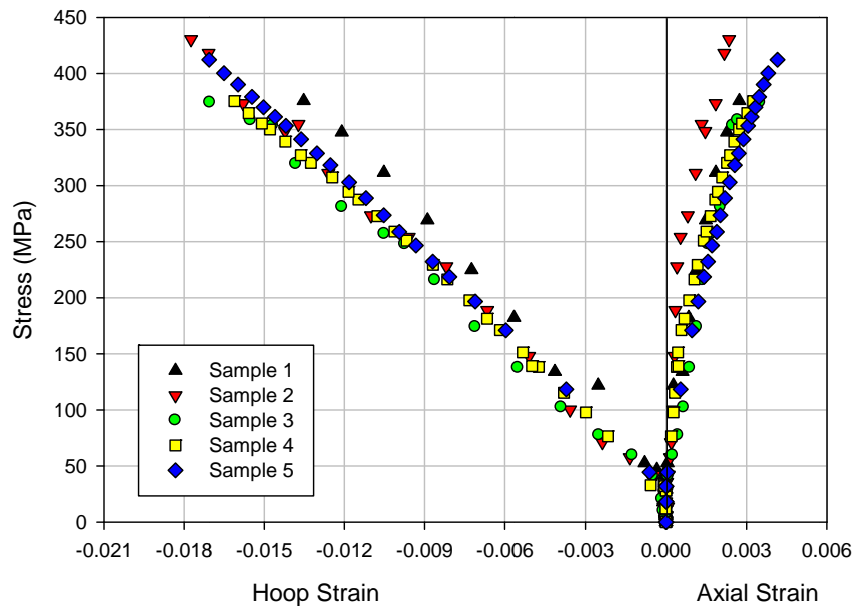


Figure 4-13: Baseline hoop tension stress-strain curve of the FRP tube.

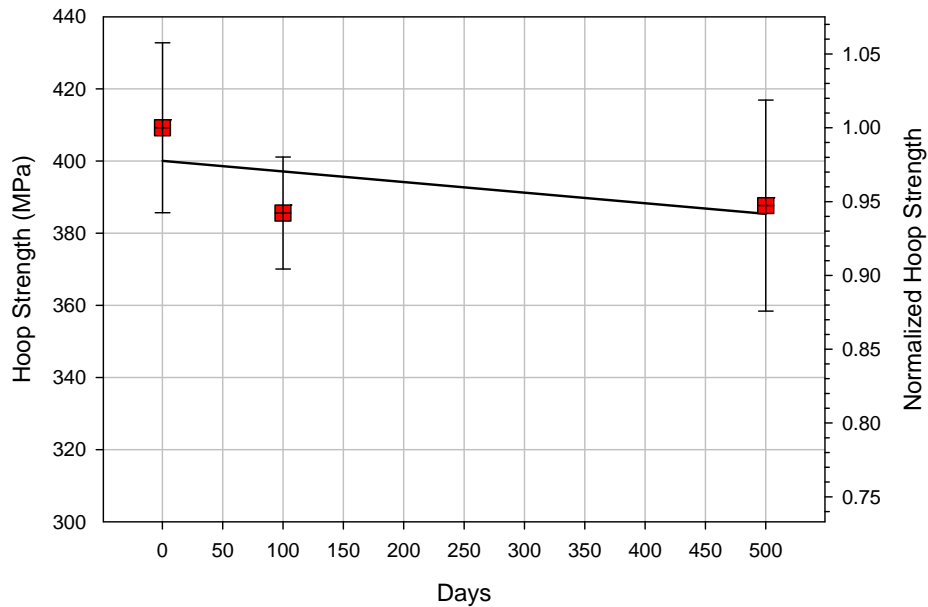


Figure 4-14: Average tension hoop strength at ambient conditions (not submerged).

The strength degradation in the hoop direction over 500 days was approximately 20% for samples submerged at 30°C, 40°C and 50°C. The degradation along this period of time for samples submerged at 30°C, 40°C and 50°C is presented in semi-logarithmic graphs in Figure 4-15 to Figure 4-17 respectively. Additionally, the strength normalized to the baseline strength is reported. A summary of these results is presented in Figure 4-18, and the complete stress-strain curves obtained are available in the Appendix B.

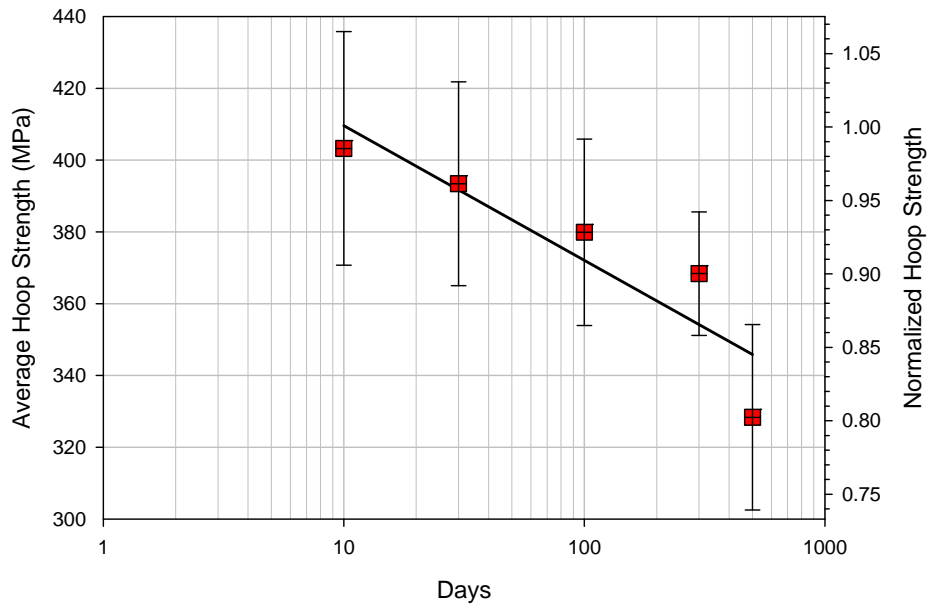


Figure 4-15: Degradation of tension hoop strength at 30°C.

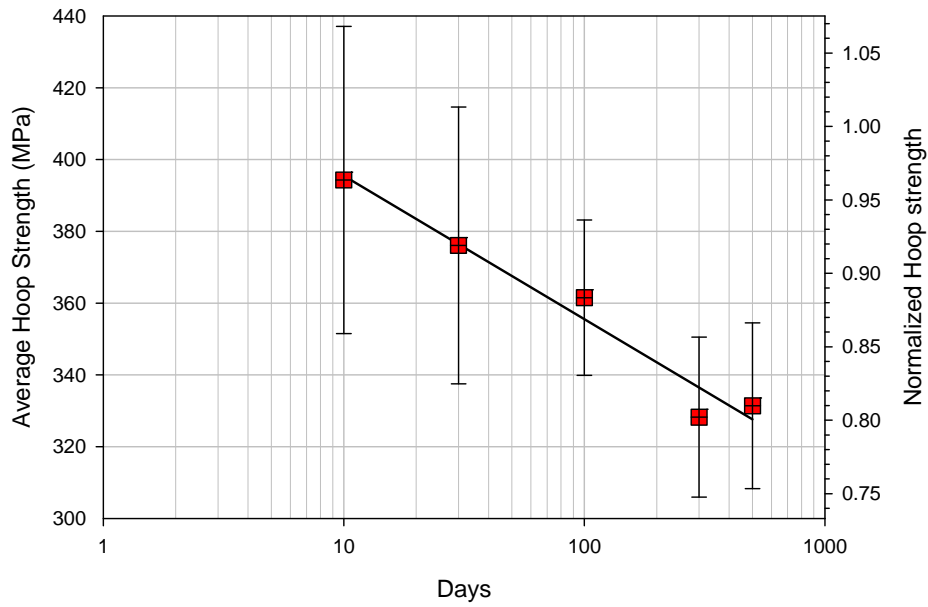


Figure 4-16: Degradation of tension hoop strength at 40°C.

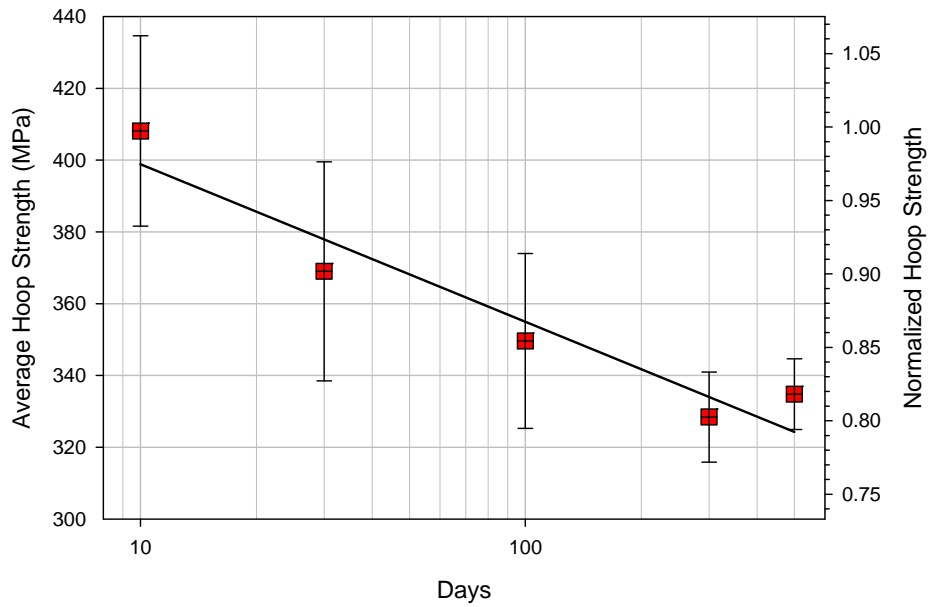


Figure 4-17: Degradation of tension hoop strength at 50°C.

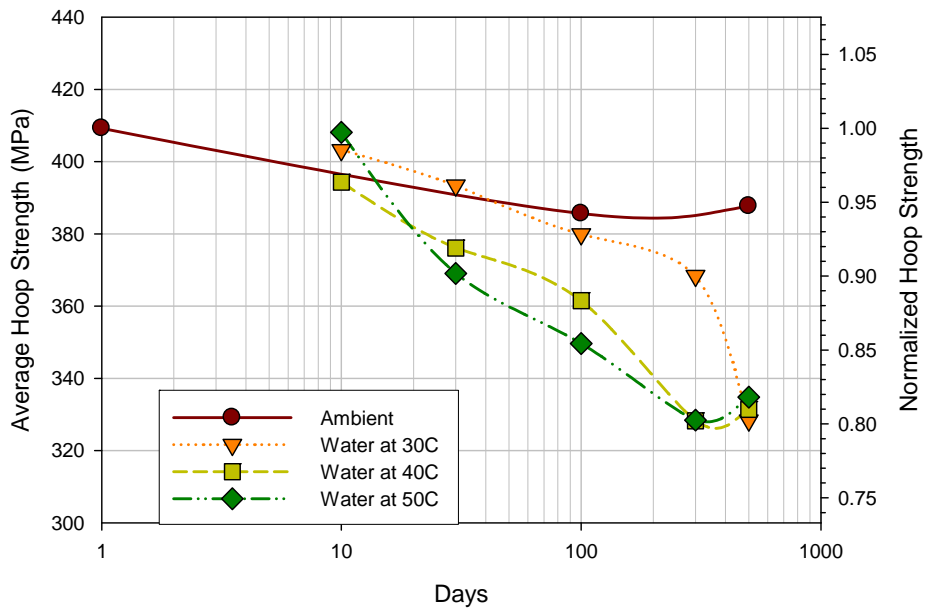


Figure 4-18: Summary of hoop strength degradation.

4.2.3 Axial tension test

The baseline axial tensile properties for the composite tubes are summarized in Table 4-5. Selected stress-strain curves obtained from 25 tests are shown in Figure 4-19. Figure 4-20 shows a picture of a baseline sample tested in axial tension. No evidence of change in the elastic modulus over 500 days of aging at 30°C was observed as seen in Figure 4-21.

Axial tension strength data obtained for samples submerged in water at 30°C for the first 500 days are given in Figure 4-22. These samples show approximately a 15% decrease in strength over this period. Additionally, the strength normalized to the baseline strength is reported.

Table 4-5: Baseline axial tension properties.

Property	Average	SD
Tensile strength (MPa)	184.51	17.11
Peak strain	0.0183	0.0046
Initial modulus (MPa)	18228	2899

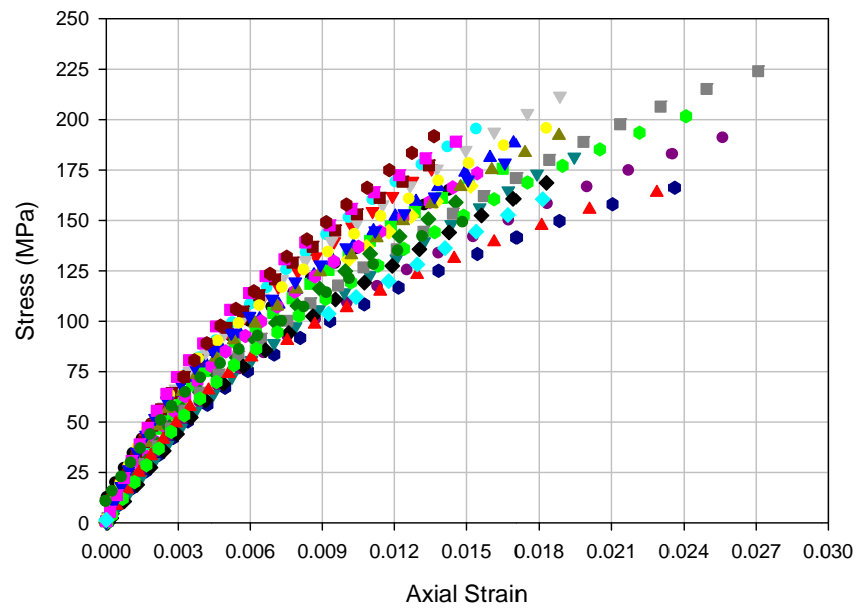


Figure 4-19: Baseline axial tension stress-strain curves.



Figure 4-20: Picture of baseline sample tested in axial tension.

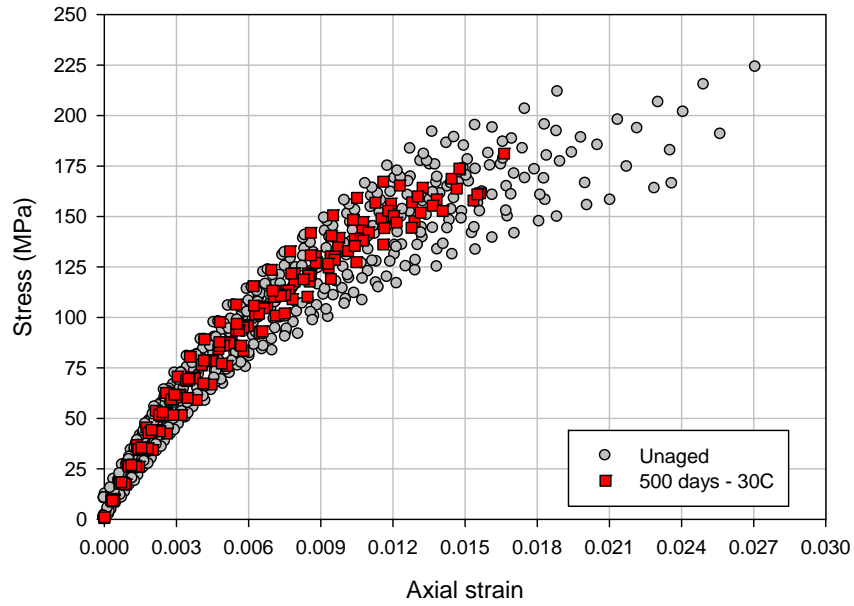


Figure 4-21: Comparison of the axial tension stress-strain curve of the FRP tubes.

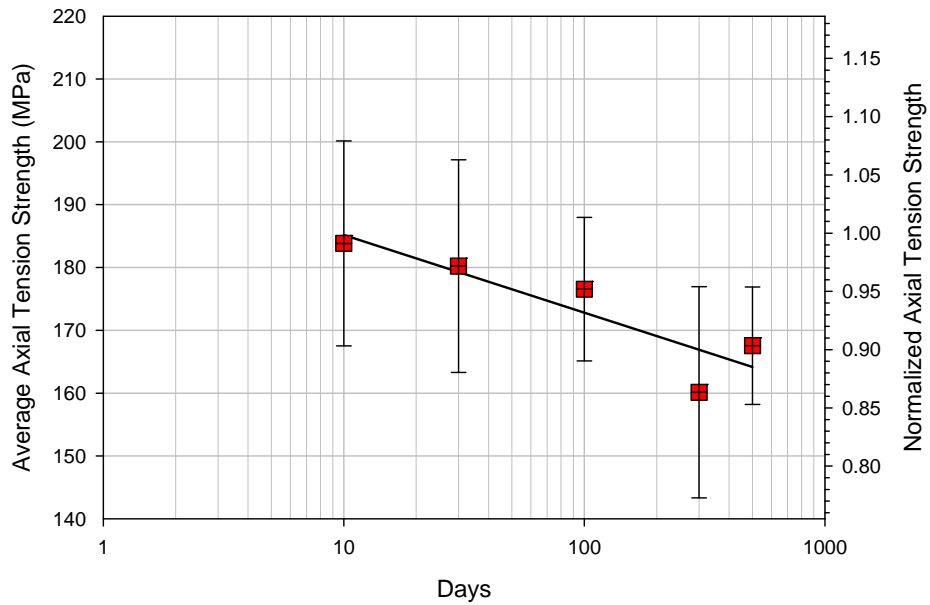


Figure 4-22: Degradation of axial tension strength at 30°C.

4.2.4 Axial compression test

The baseline axial compression properties for the FRP are summarized in Table 4-6. Stress-strain curves of selected samples from the 25 tests are plotted in Figure 4-23. Figure 4-24 shows a picture of a baseline sample tested in axial compression after failure. No evidence of change in the elastic modulus over 500 days of aging was obtained, as seen in Figure 4-25.

Table 4-6: Baseline compression properties.

Property	Average	SD
Compressive strength (MPa)	275.43	23.78
Peak strain	0.0164	0.0019
Initial modulus (MPa)	22418	8273

The ambient-aged data are relatively unchanged over the course of 500 days with the exception of day 30 and 500 as seen in Figure 4-26. Data from day 30 shows a temporary increase in the compression strength, which over the next 70 days disappears as the measured strengths return to the initial strength. Data from day 500 shows a decrease in the compression strength, with a similar magnitude similar obtained for day 30.

Axial compression data obtained in samples submerged in water at 30°C, 40°C and 50°C for the first 500 days of aging are given in Figure 4-27 to Figure 4-29. Additionally, the strength normalized to the baseline strength is reported. A summary of these results is presented in Figure 4-30.

Compression data from all three hygrothermal aging conditions suggest the samples suffered certain degree of strength reduction over the first 500 days. However, the 50°C samples exhibited a significant amount of strength reduction, in the order of 30 %. The 30°C

samples, however, showed smaller decrease (approximately 20%) in compression strength over 500 days.

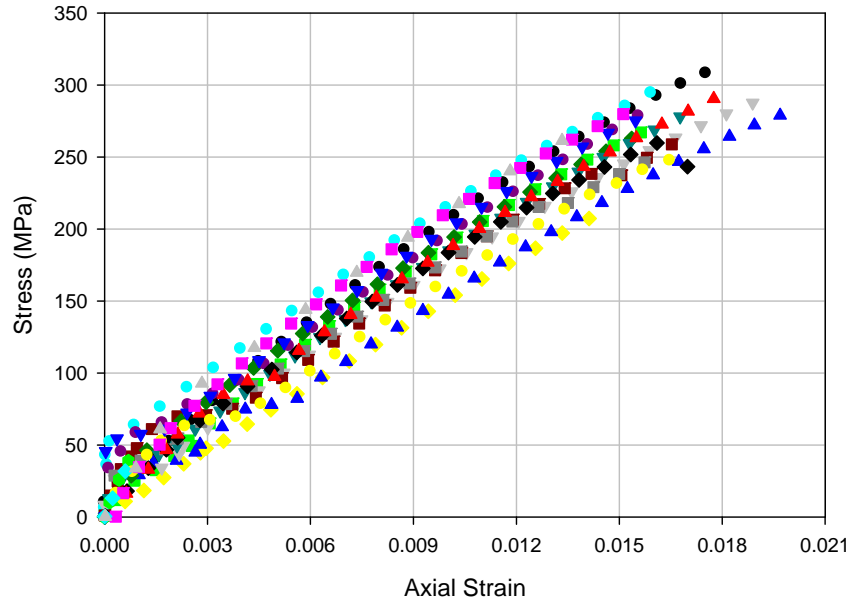


Figure 4-23: Baseline axial compression stress-strain curve of FRP tubes.

After 500 days of aging, tension strength was 70% of the compression strength. However, the dimensions of the compressive and tensile samples were considerably different; the tension sample widths and gage lengths were larger by factors of 2 and 6, respectively. Furthermore, the compression samples were end-loaded, while the tension specimens were gripped on the face.

It has long been assumed that the models for longitudinal strength cannot be used for compressive strength because the modes of failure are different. This assumption has been supported by observed differences in measured tensile and compressive strengths (Gibson, 1994). Accurate measurement of the intrinsic compressive strength has proved to be very difficult. However, test results to date typically depend on specimen geometry and/or test method (Whitney, 1991).



Figure 4-24: Picture of baseline sample tested in axial compression.

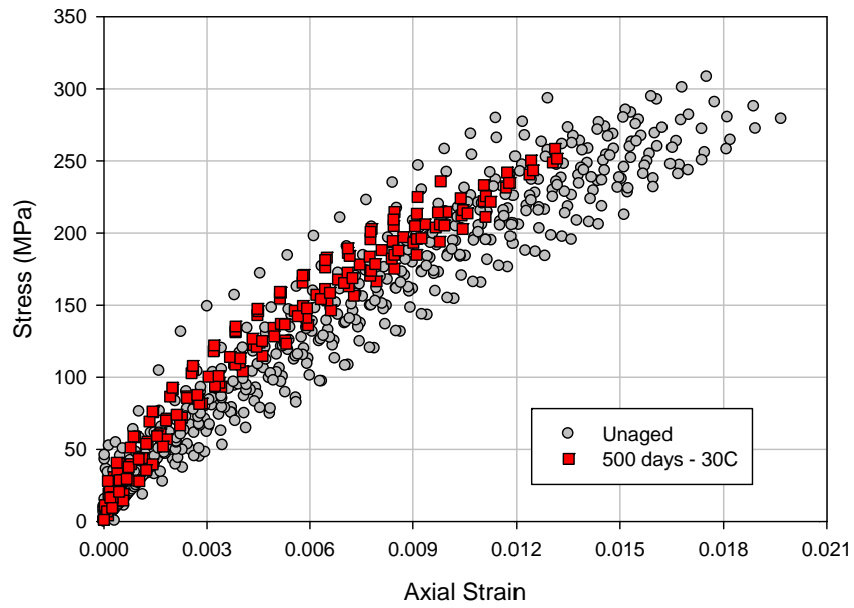


Figure 4-25: Comparison axial compression stress-strain curve.

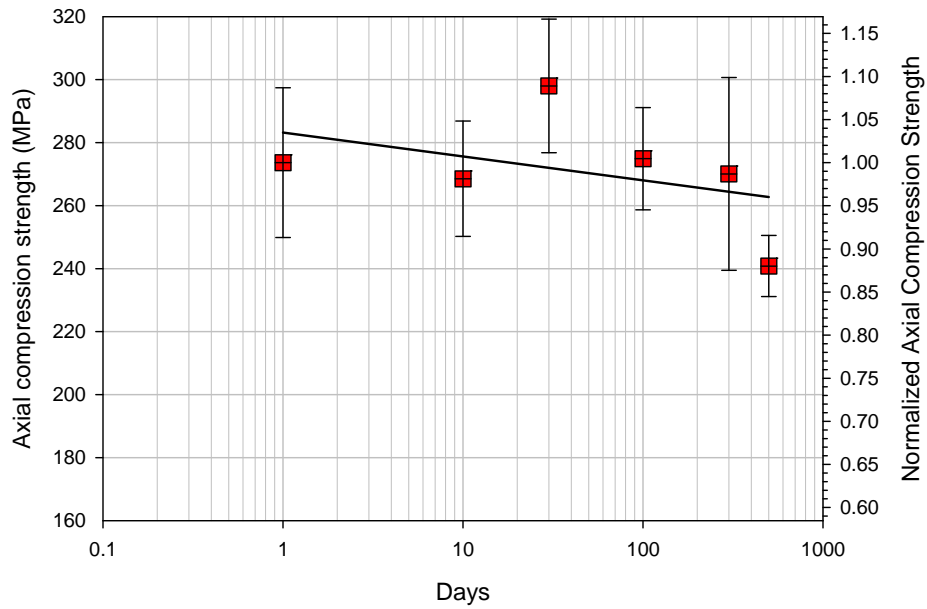


Figure 4-26: Degradation of axial compression strength at ambient conditions.

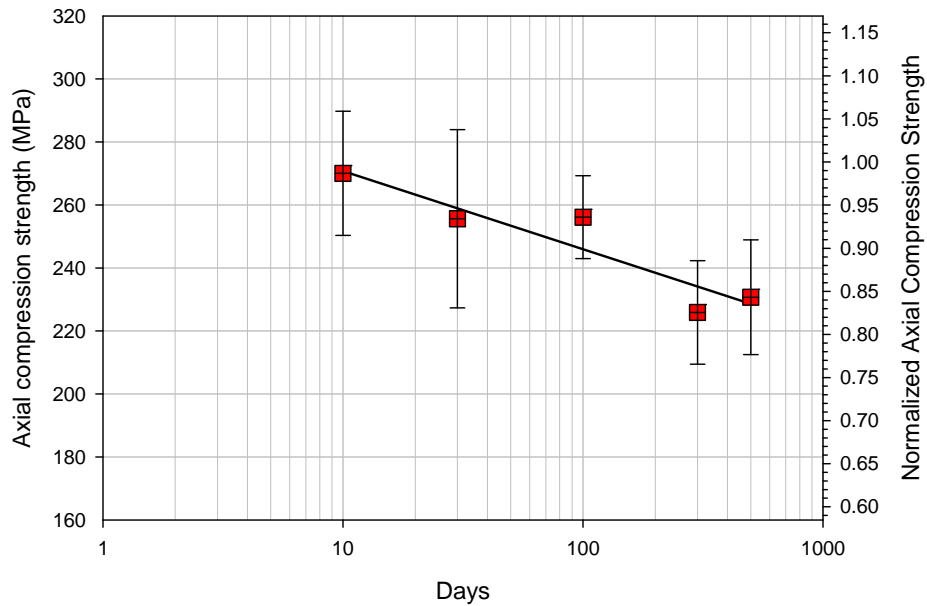


Figure 4-27: Degradation of axial compression strength at 30°C.

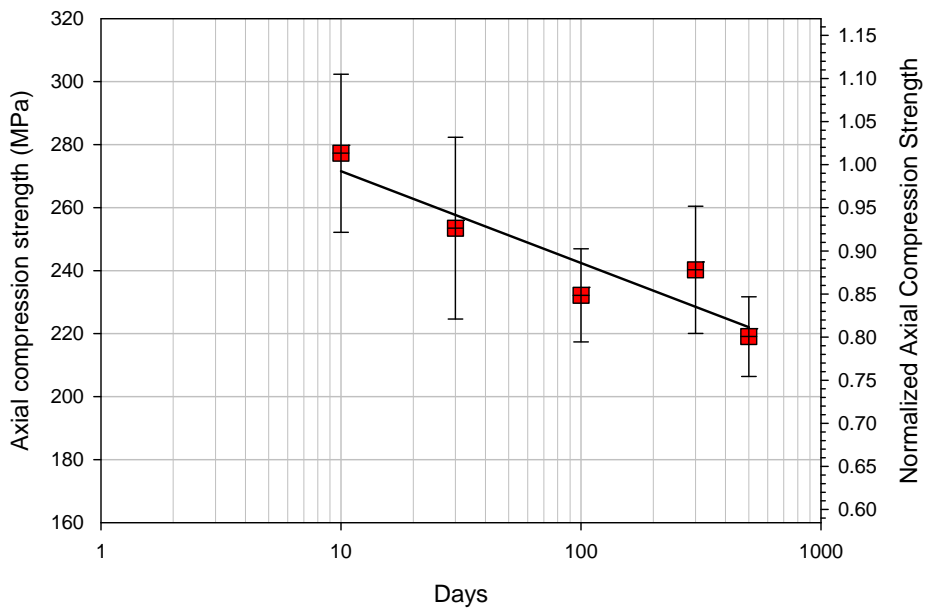


Figure 4-28: Degradation of axial compression strength at 40°C.

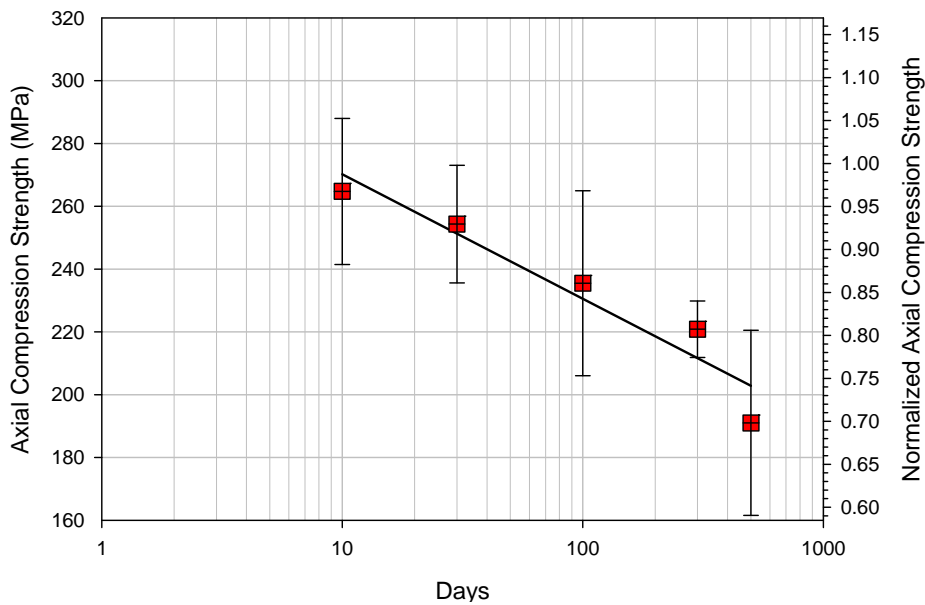


Figure 4-29: Degradation of axial compression strength at 50 °C.

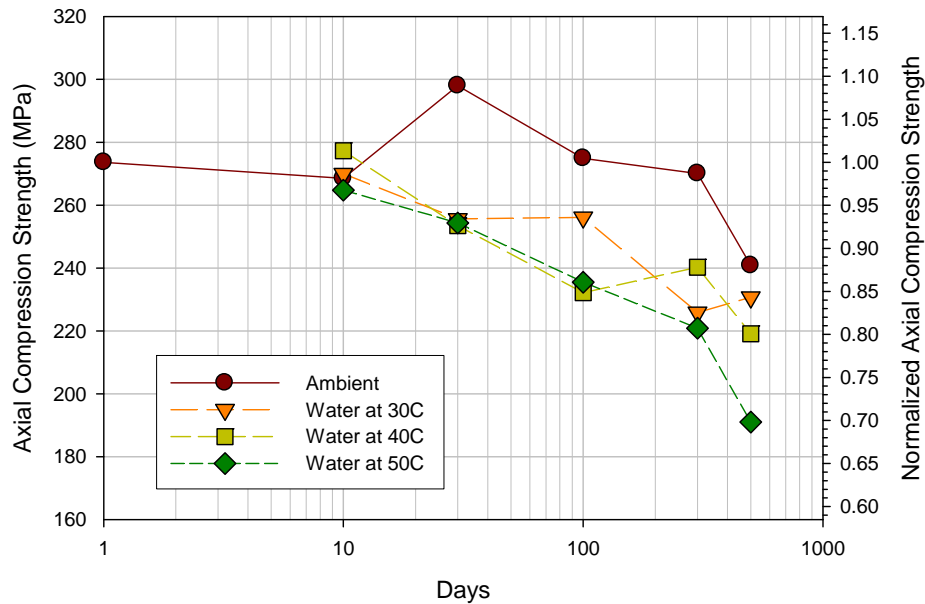


Figure 4-30: Degradation axial compression strength summary.

4.3 FRP Tubes Compression Test

Additionally, the FRP tube compression test was performed at UPRM facilities. These tests allowed to perform the calibration of the 3-D concrete filled FRP tube finite element model. Similarly to the CFFT, FRP tube ends were carefully sanded to level the surface prior to testing. The axial compression test on FRP tubes was carried out ensuring centricity of load. Instrumentation included three sets of axial and hoop strain gauges inside and outside of the tube. Strain gauges were located at the mean length of the tube and distributed evenly.

Most composites tubes are made from high strength, high stiffness fibers, embedded in rigid cross-link thermosetting resins such as epoxy. Unlike ductile metals and thermoplastics, the fibers and resins are brittle and they fail by fracture after an initial elastic deformation. Depending on the geometry, composite material and loading conditions, there

are two possible modes by which a tube under axial compression may fail globally, in addition to the overall Euler-type buckling exhibited by metal tubes. It can fail by sudden fracture around the center of a tube or by progressive type of crushing (Lu and Yu, 2003). A progressive crushing at tube ends with the subsequent formation of crush zone was observed similar to the results obtained from the CFFT compression tests.

Ultimate axial strain obtained from these results is similar to the results obtained from the CFFT compression tests. Figures 4.30 to 4.32 show the results obtained from three tested tubes under compression load. Differences between the obtained data from inside and outside gauges were not detected in the tests.

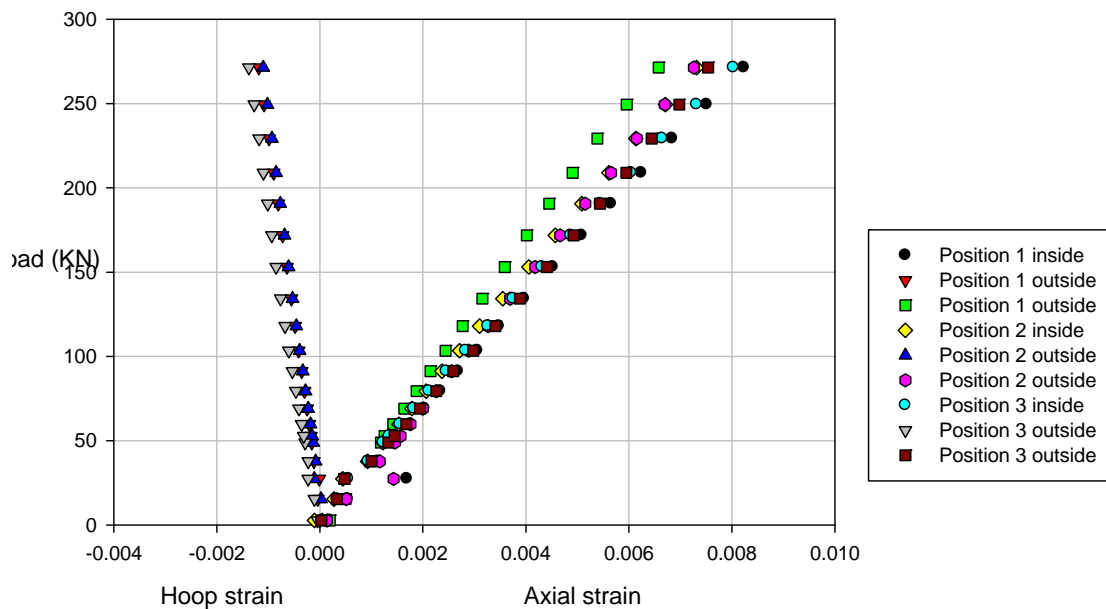


Figure 4-31: Baseline axial compression stress-strain curve (tube 1).

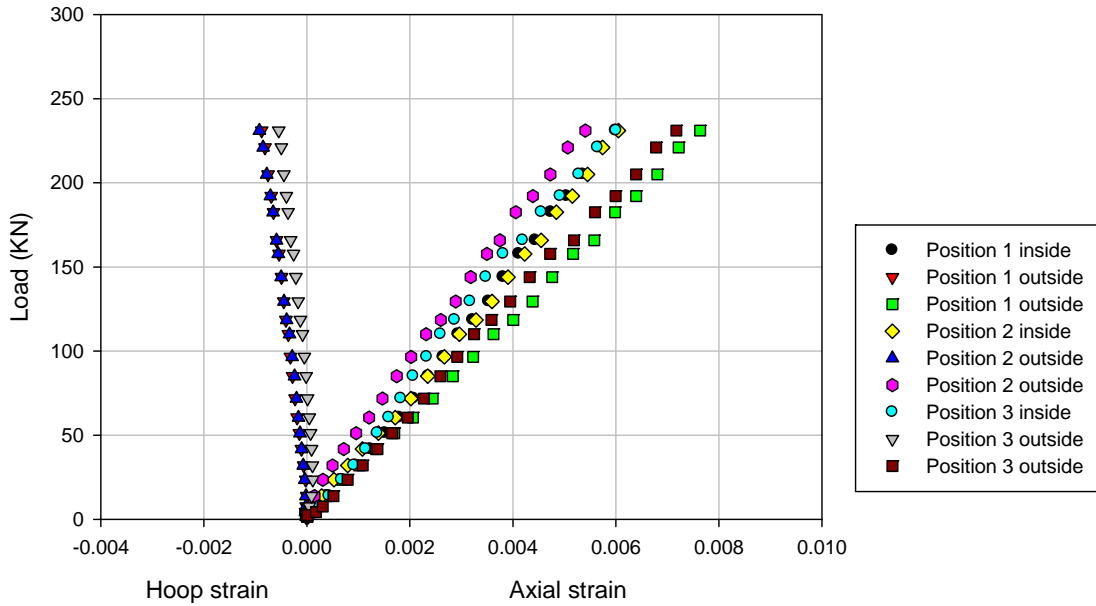


Figure 4-32: Baseline axial compression stress-strain curve (tube 2).

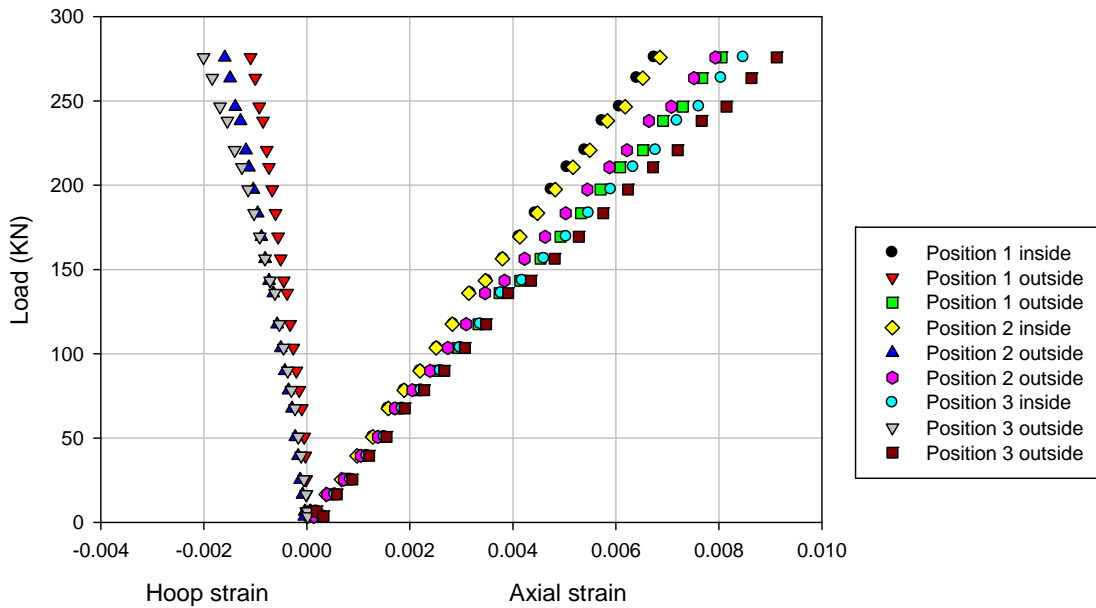


Figure 4-33: Baseline axial compression stress-strain curve (tube 3).

4.4 CFFT Compression Test

The typical axial load-strain curve of a CFFT is shown in Figure 4-34. This figure illustrates how both the axial and lateral responses are approximately bi-linear. The initial portion of the curves is controlled by the axial stiffness of the concrete core. Then, the transition zone between the two slopes generally corresponds to the peak strength of unconfined concrete core. Finally, the second portion of the curves has a slope mainly related to the hoop properties of the FRP tube. Failure is usually reached when the FRP tube fails under hoop tension. Several models have been proposed to predict the response of axially load CFFT (e.g. Spoelstra and Monti 1999 and Fam 2000). Similarly, predictive tools for CFFT in bending and combined bending and compression have been developed by Mirmiran and Shahawy (1997), and Fam (2000).

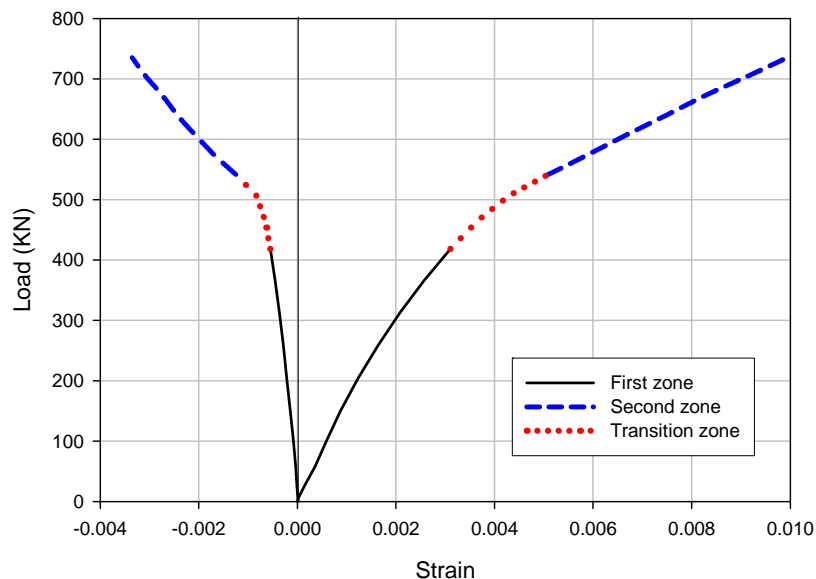


Figure 4-34: Typical Load-Strain Curves for CFFT.

The suitability for the capping method of CFFT specimens subjected to compression load was evaluated (Davila, 2008). An early failure was obtained for all the capping systems evaluated by Davila (2008). Therefore, Davila (2008) concluded that the best option was not to use any capping for the CFFT ends.

CFFT samples were carefully sanded at the ends to ensure uniform contact with the machine heads. Photos of CFFT failed specimens are shown in Figure 4-35, showing the typical failure modes. From the photos it is observed that the FRP tubes failed by tension generated in the hoop direction due to the confinement effect to the concrete core. The typical mode of failure is characterized by the crushing and splitting at the ends when the FRP tube reaches its compression axial strength. This mode is clearly observed in the specimen shown in Figure 4-35a.

Following that there is a spiral (Figure 4-35a) or vertical path of rupture (Figure 4-35b) or a combination of both (Figure 4-35c) on the FRP Shell when the tension lateral (hoop) strength is exceeded. The behavior observed in the load-strain response of the composite system is approximately bilinear as reported in the literature (Samaan, et al., 1998, Harries and Kharel, 2003).

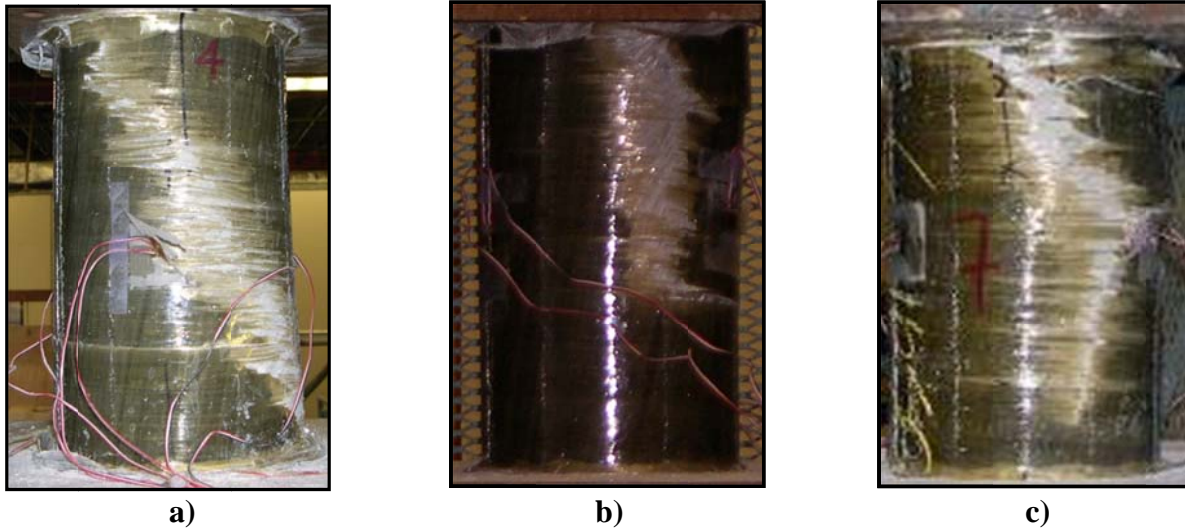


Figure 4-35: Example of failure modes of CFFT samples.

Figure 4-36 shows typical experimental load-strain curves for axial and hoop directions including a schematic description of the typical failure mode. Even though both the concrete and the FRP core are loaded simultaneously, the first part of the curve approximately coincides with the curve of the unconfined concrete indicating that the confinement effect is activated once the strength of the unconfined concrete is reached (Figure 4-37). The core sustained additional load beyond the unconfined failure stress thanks to the confinement provided by the FRP shell. The observation of the failed samples after the test revealed fragmentation of the concrete core.

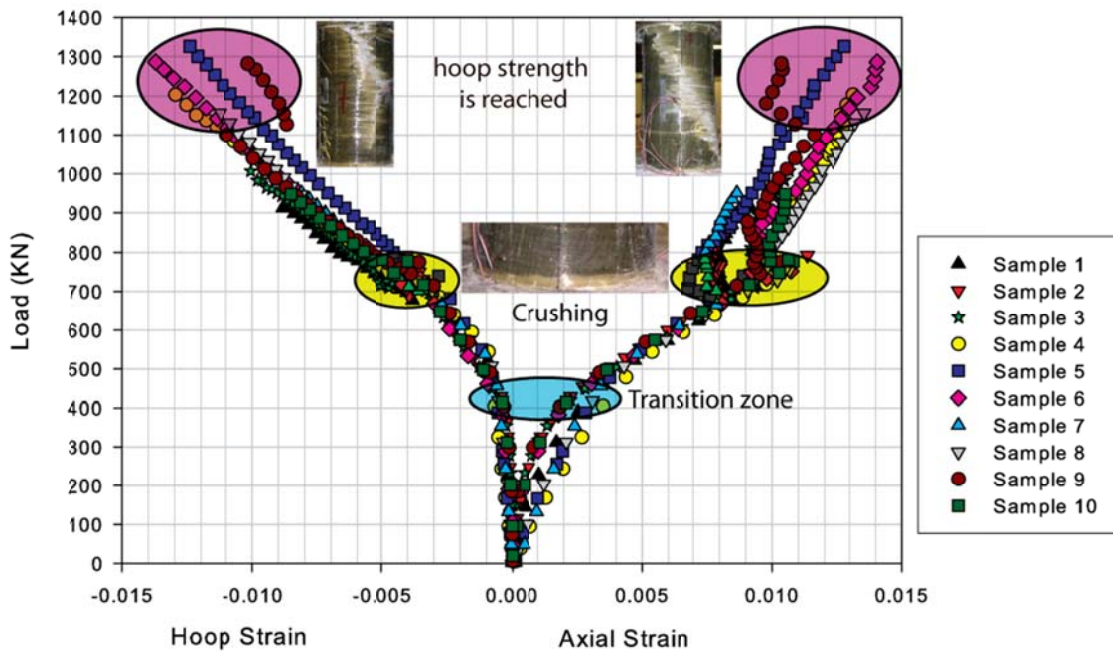


Figure 4-36: Typical axial compression load-strain curve.

Axial compression data of CFFT from fifty tests are given in Figure 4-38 to Figure 4-42. The data presented show up to 500 days of aging in water at 30°C. The stiffness and crushing load are relatively unchanged over the course of 500 days.

Figure 4-43 shows the loads and the standard deviations observed on CFFT specimens before the crushing and the ultimate state. The crushing load value obtained for all ages were similar. This failure is possibly due to stress concentrations at the end of the tube (local damage). This effect is studied in another chapter using a 3-D finite element model. A reduction in the ultimate strength of approximately 20 % over 500 days was observed. This decrease of strength is similar to that obtained in the mechanical properties of the FRP.

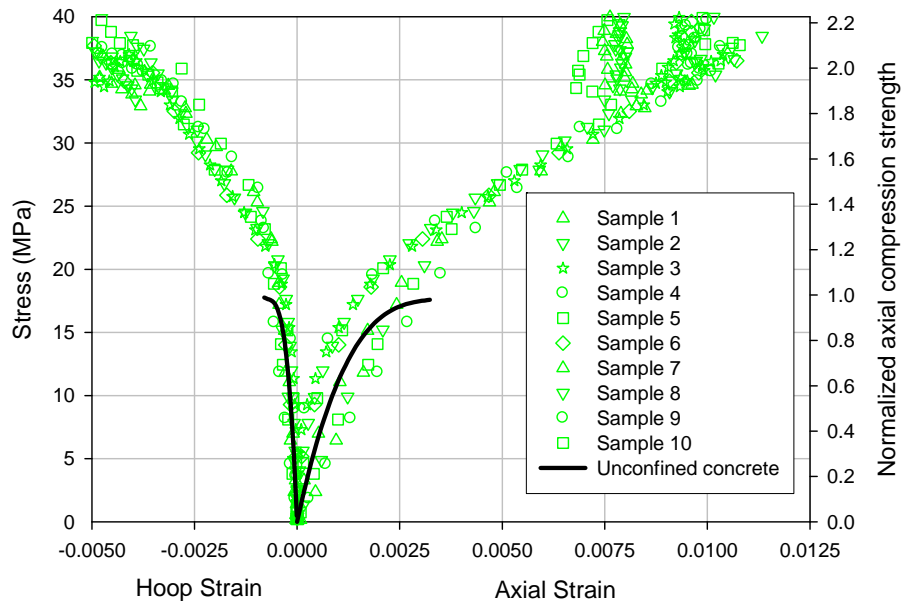


Figure 4-37: Comparison of the behavior between CFFT and unconfined concrete.

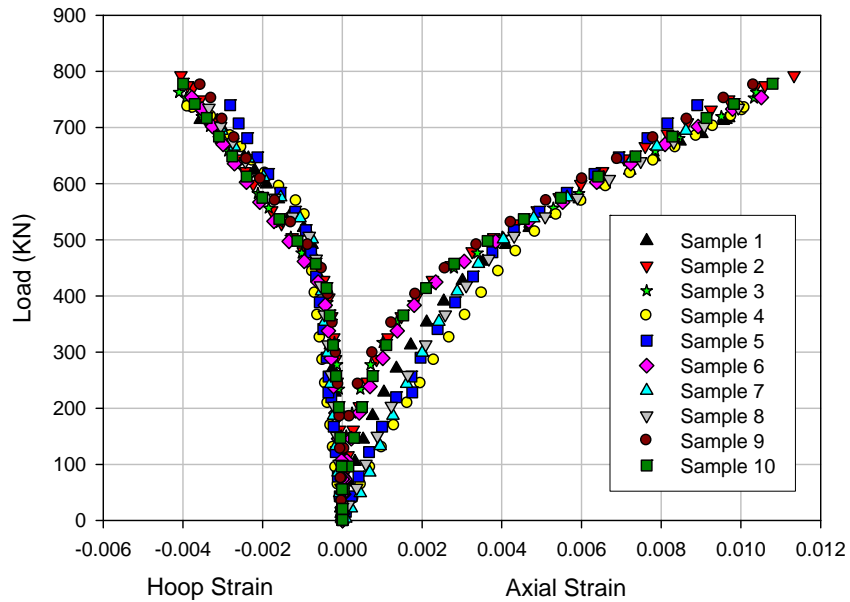


Figure 4-38: Baseline axial compression load-strain curve.

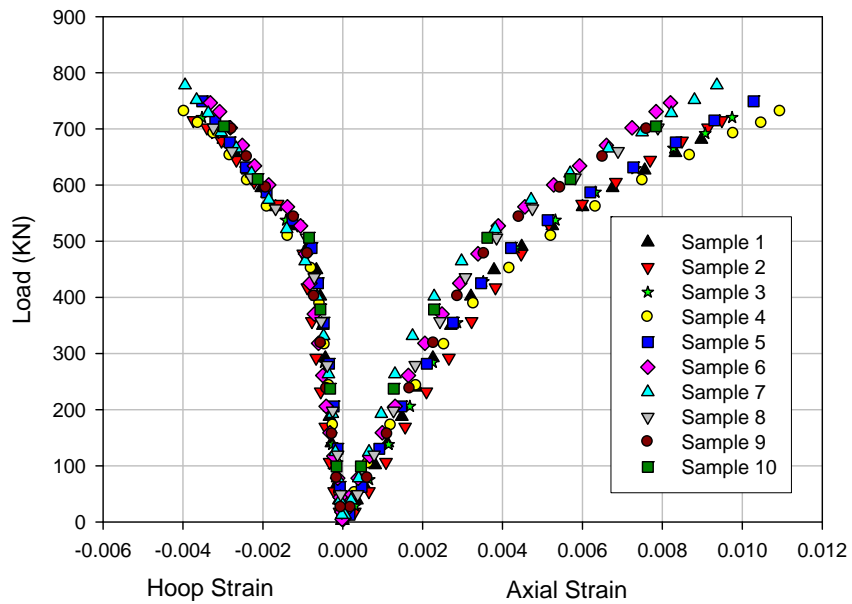


Figure 4-39: Axial compression load-strain curve after being submerged in water for 30 days.

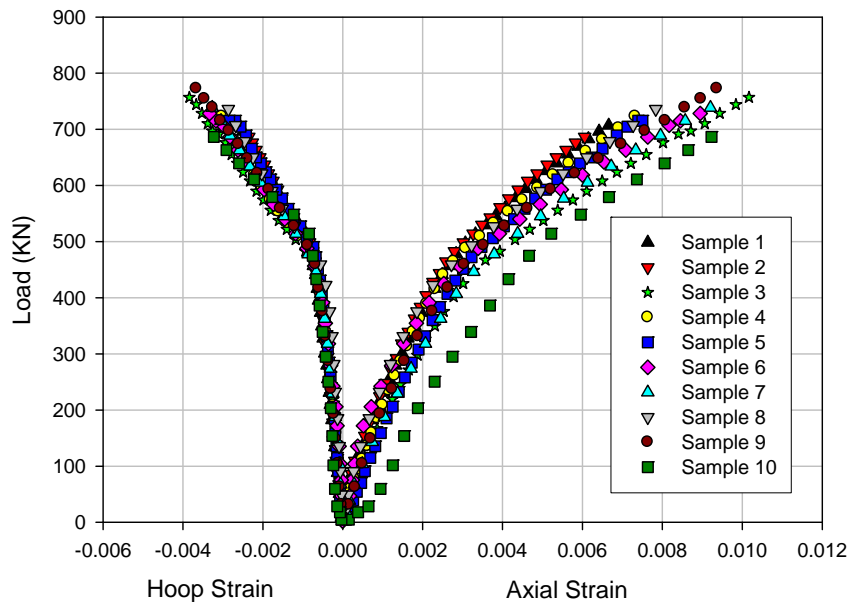


Figure 4-40: Axial compression load-strain curve after being submerged in water for 100 days.

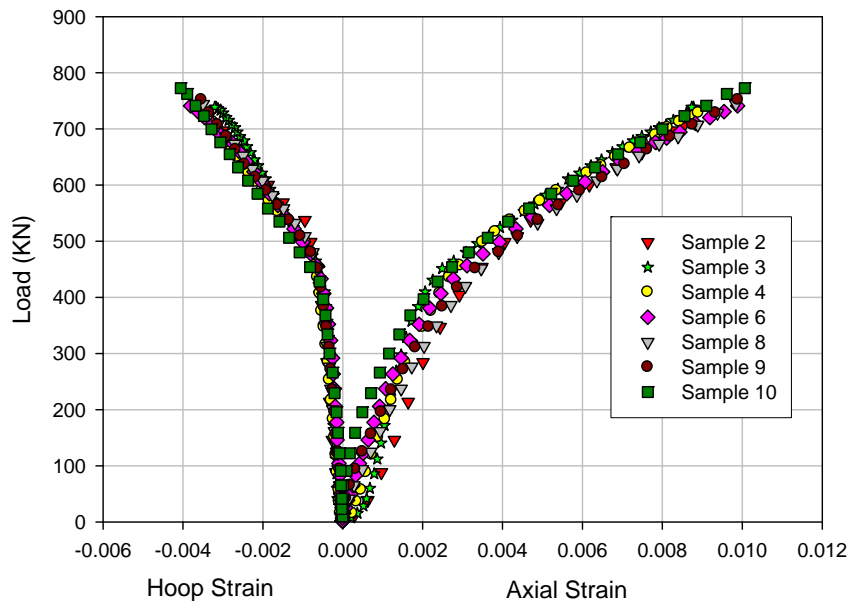


Figure 4-41: Axial compression load-strain curve after being submerged in water for 300 days.

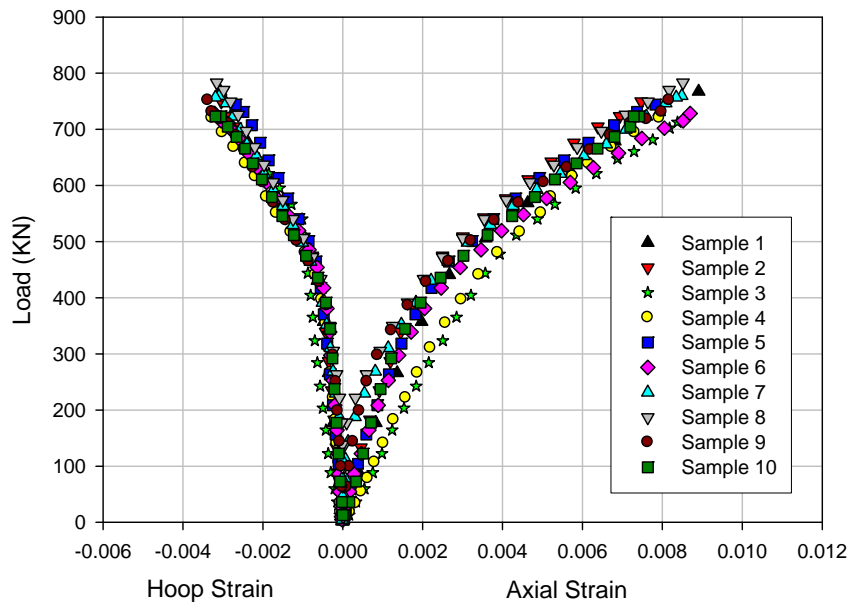


Figure 4-42: Axial compression load-strain curve after being submerged in water for 500 days.

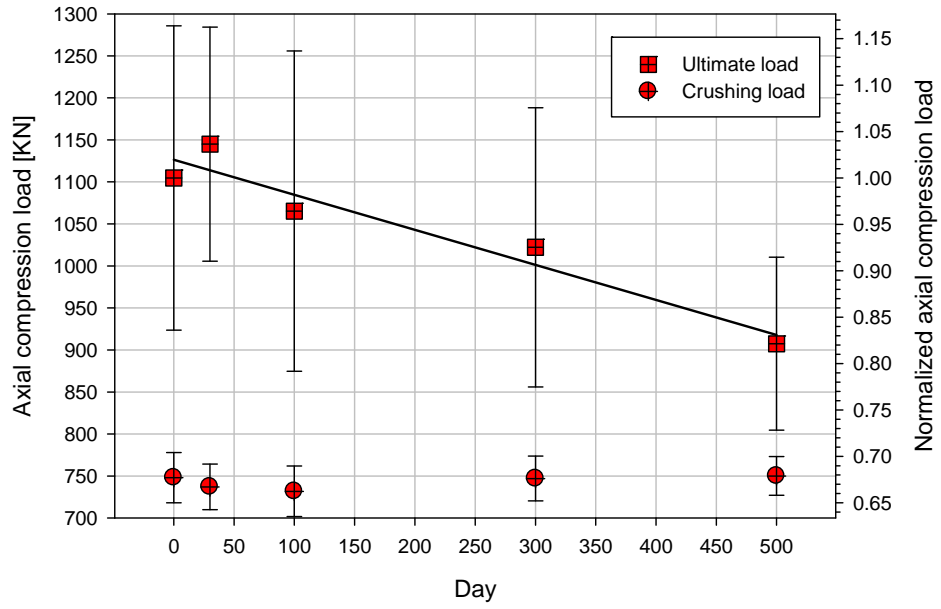


Figure 4-43: Crushing and ultimate loads measured on CFFT.

CHAPTER 5

DURABILITY AND LONG-TERM BEHAVIOR PREDICTION

A methodology to predict the long-term strength of composites is studied in this chapter. The predictions are based on macro-mechanical and micro-mechanical models developed in recent years to predict the long-term strength of unidirectional composites and its constituents.

5.1 Macro-mechanical Long-Term Behavior

This section presents a procedure based on the Arrhenius relation to predict the long-term behavior of glass fiber-reinforced polymer, based on short-term data from accelerated aging tests. FRP coupons were exposed to simulated hygrothermal aging at 30, 40, and 50°C. The tensile strengths of the FRP coupons determined before and after exposure were considered a measure of the durability performance of the specimens.

Based on the short-term data, a detailed procedure is developed and verified to predict the long-term durability performance of FRP tubes. The accelerated test and prediction procedures can be a reliable method to evaluate the durability performance of FRP composites exposed to hygrothermal conditions.

The rate of a reaction depends on the temperature at which it is run. As the temperature increases, the molecules move faster and therefore collide more frequently. The molecules also carry more kinetic energy. Thus, the proportion of collisions that can overcome the activation energy for the reaction increases with temperature. The only way to explain the relationship between temperature and the rate of a reaction is to assume that the rate constant depends on the temperature at which the reaction is run (Bodner, 2011).

In 1889, Svante Arrhenius showed that the relationship between temperature and the rate constant for a reaction obeyed the equation 5.1, where E_a is the activation energy, a_T is the time-based shift factor, R is the universal gas constant, and T is the temperature.

$$\log(a_T) = \left(\frac{-E_a}{R \cdot T} \right) \quad [5.1]$$

Activation energy term from the Arrhenius equation is an experimentally determined parameter that indicates the sensitivity of the reaction rate to temperature (Bodner, 2011). Because the relationship of reaction rate to activation energy and temperature is exponential, a small change in temperature or activation energy causes a large change in the rate of the reaction. The primary assumption of Arrhenius model is that the single dominant degradation mechanism of the material will not change with time and temperature during the exposure, but the rate of degradation will be accelerated with the increase in temperature.

The shift factors for the FRP coupons exposed to hygrothermal aging were found by minimizing the R^2 value for a least squares fit through the strength versus $\log(t a_T)$ data. This method yielded the shift factors reported in Table 5-1. Shifting the data in this way resulted in the graph of Figure 5-1, in which the predicted strength is plotted as a function of the shifted time and displayed on a semi-log graph. Taking the slope of a line fitted through the a_T versus

$1/T$ data (see Figure 5-2), we find that an estimate of the activation energy for the compression strength degradation is $E_a=41.5 \text{ kJ/mol}$.

Table 5-1: Time-based shift factors for axial compression strength

<i>Aging water temperature</i>	<i>Shift factor, a_T</i>
30°C	1
40°C	1.32
50°C	2.85

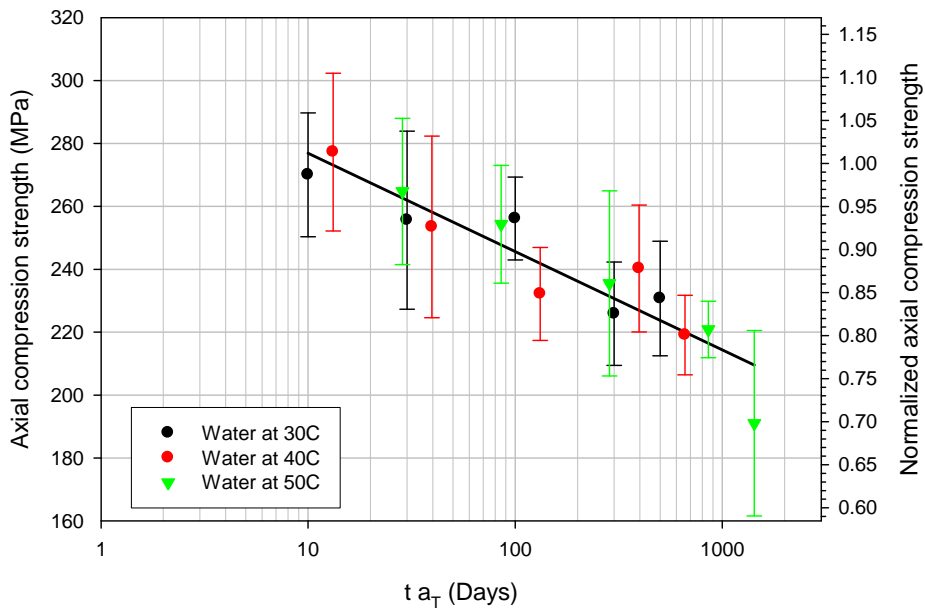


Figure 5-1: Shifted axial compression strength plot with fit line.

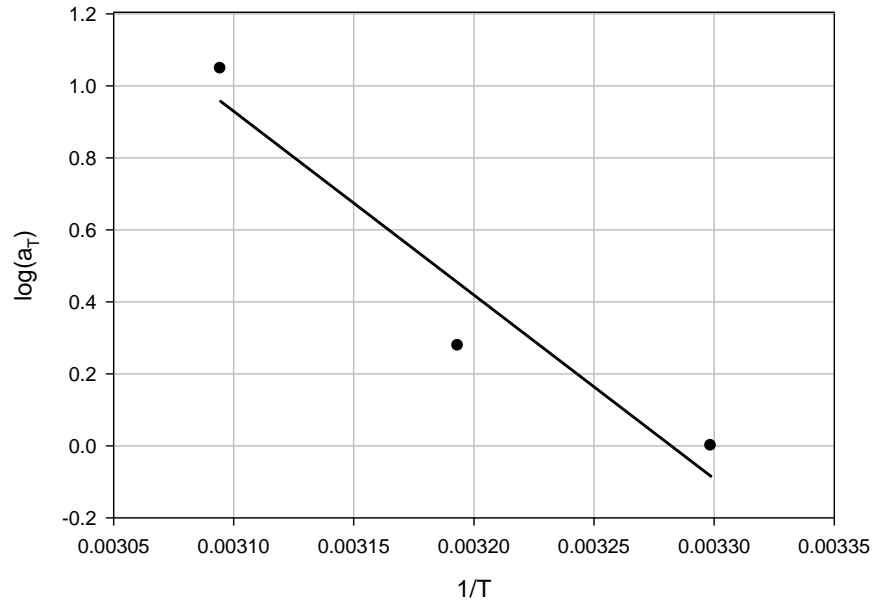


Figure 5-2: Procedure to obtain the activation energy for the compression strength degradation.

Similar to axial compression data, it was assumed the hoop tensile strength data could be modeled by the Arrhenius equation. Following the same procedure mentioned previously, we find the shift factors for hoop strength reported in Table 5-2.

Table 5-2: Time-based shift factors for axial compression strength

<i>Aging water temperature</i>	<i>Shift factor, a_T</i>
30°C	1
40°C	2.54
50°C	2.59

With these shift factors, the data is plotted in Figure 5-3. It is clear the Arrhenius fit proved to be effective in modeling either the axial compression or hoop tension data over extended periods. Again taking the slope of a line fitted through the a_T versus $1/T$ data (see Figure 5-4), we find that an estimate of the activation energy for the hoop tension strength degradation is $E_a=38.3 \text{ kJ/mol}$.

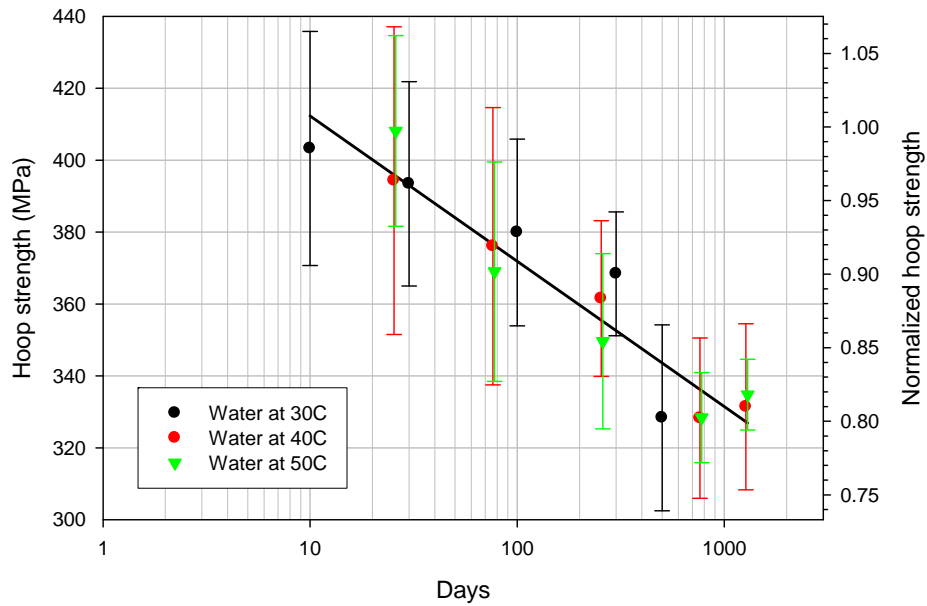


Figure 5-3: Shifted hoop strength plot with fit line.

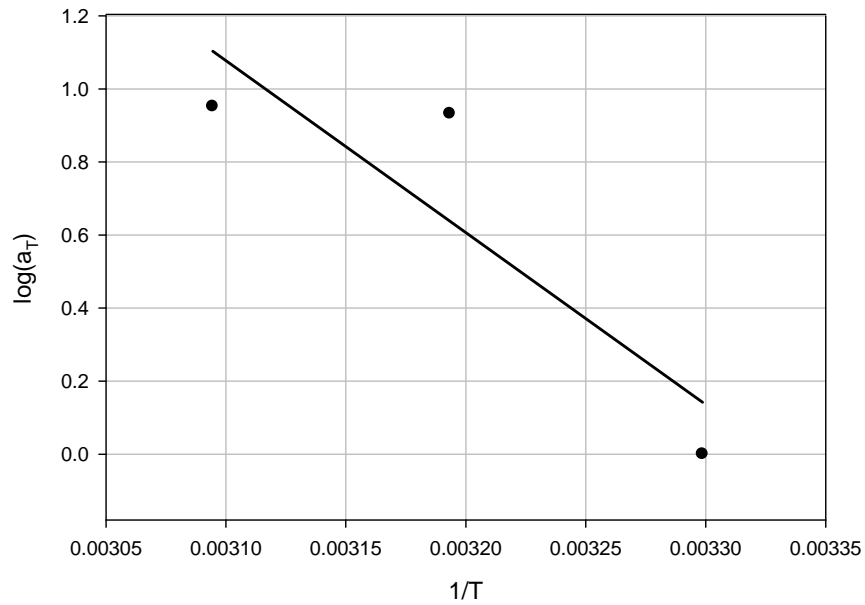


Figure 5-4: Procedure to obtain the activation energy for the hoop strength degradation.

Figure 5-1 and Figure 5-3 predict a strength reduction near to 20% after 1000 days of aging in water at 30 °C. The strength degradation level can be calculated for any period of time if it is assumed that activation energy is a constant value.

The hoop data shows a similar degradation behavior for the high temperatures, of 40°C and 50°C. Because the FRP composition is different in the axial and the hoop direction, different degradation levels for each case is expected. The comparison between the axial and hoop data showed more strength degradation in the axial direction.

5.2 Micro-mechanical Long-Term Behavior

Numerous studies are being carried out to assess the effect of aging and environmental exposure on the strength of composites. The studies had combined different types of fiber/matrix, laminate stacking sequences and hybrid systems of components with conventional materials (Thomas, 1960, Otto, 1965, Metcalfe and Schmitz, 1972, France, et al., 1983).

Most studies report a small number of parameters that can be measured. These include the age, conditions of exposure, and remaining strength after exposure. In addition, the type of fibers, matrix, and processing technique used to manufacture the samples has been reported by these studies. More sophisticated data, such as variability of Weibull modulus with age are not available nor are feasible to measure because of the complexity of the material and structural systems being studied (Barbero and Damiani, 2003).

In view of this, models that do not require such detailed knowledge are useful even if they are approximate. The model proposed by Barbero and Damiani (2003) provides a reasonable interpretation of the available data while using nominal values taken from the

literature for parameters such as the Weibull dispersion. This approach does not neglect such refined quantities but incorporates their effect via curve-fitting of observed behavior for each degradation mechanism. The resulting model evaluates their combined effect on the life of the composite.

The model assumes that the fiber strength data follows a Weibull distribution with a dispersion m and characteristic value μ . The characteristic value μ of the Weibull distribution is related to the average strength σ of the fibers by the Gamma function [Equation 5.2] as

$$\mu = \frac{1}{L} \left[\frac{\Gamma\left(1 + \frac{1}{m}\right)}{\sigma} \right]^m \quad [5.2]$$

where L is the fiber length used while testing for average strength σ and Weibull dispersion m . The Weibull dispersion for E-glass recommended by Barbero and Damiani (2003) is $m=8.89$. Table 5-3 shows the average strength values for different gauge lengths by Phani (1988). The average strength expression developed by Barbero and Damiani (2003) as function of time is presented later in Equation 5.8.

Table 5-3: Average strength values of E-glass fibers.

Type of glass fiber	Gauge length	Measured values	Standard deviation
	(mm)	10 ³ psi	10 ³ psi
E	15	292	57.8
	30	277	40.1
	60	227	50.6
	120	233	39.8
	240	227	45.3

According to Barbero and Damiani (2003), the debonding length $2L_d$ increases the ineffective length to $\delta + L_d$. Using the weakest-link model (Kelly and Barbero, 1998) with

provision for the debond length, yields a prediction for the strength of the composite lamina as

$$F_{1t} = [\mu(\delta + L_d)me]^{-\frac{1}{m}} \quad [5.3]$$

where e is the base of the natural logarithms. For an elastic matrix with shear modulus G_m , the ineffective length can be estimated as (Rosen, 1964):

$$\delta = \frac{d_f}{2} \left[\left(\frac{1 - \sqrt{V_f}}{\sqrt{V_f}} \right) \left(\frac{E_f}{G_m} \right) \right] \cosh \left[\frac{1 + (1 - \phi)^2}{2(1 - \phi)} \right] \quad [5.4]$$

where d_f is the diameter of the fiber, V_f is the fiber volume fraction of the composite, E_f is the modulus of elasticity of the fiber, G_m is the shear modulus of the matrix, and ϕ is defined as the fraction of the far field stress associated with δ . ϕ was considered in Rosen's analysis to be 0.9, meaning that δ is the distance at which 90 % of the far field stress is recovered. It can be inferred from the model that the longer the ineffective length the lower the composite strength.

As shown in Kelly and Barbero (1998), the ineffective length can increase due to the viscoelastic reduction of G_m with time, so the long-term modulus $G_{m\infty}$ should be used in conjunction with long-term tests. Another cause for increase of δ is the reduction of shear modulus with moisture.

The retention factor $\left(\frac{T_{gw}-T}{T_{gd}-T_0} \right)^{\frac{1}{2}}$ can be used to modify the shear modulus on account

of temperature and moisture content as

$$G_m = \left(\frac{T_{gw} - T}{T_{gd} - T_0} \right)^{\frac{1}{2}} G_{m\infty} \quad [5.5]$$

where T_0 is the reference temperature, T_{gd} is the glass-transition temperature of the dry matrix.

The glass-transition temperature of the wet polymer can be estimated as:

$$T_{gw} = (1 - 0.1m_{sat} + 0.005m_{sat}^2)T_{gd} \quad [5.6]$$

in terms of the saturation moisture content, which can be estimated by a power law of the relative humidity RH as:

$$m_{sat} = a \left(\frac{RH}{100} \right)^b \quad [5.7]$$

where $a=0.018$ and $b=1$ for Epoxy matrix composites, $m_{sat}=0.0053$ is a recommended value for E-glass/epoxy under water immersion.

Figure 5-5 shows a microscope observation of longitudinal fibers near the failure surface of the unaged CFFT specimens. Based on this observation can be assumed that the e-glass fibers have a diameter d_f , between 10 μm to 20 μm . These two values were used to predict the residual strength of the composite. The diameter of transverse fibers is assumed equal to the longitudinal fibers.

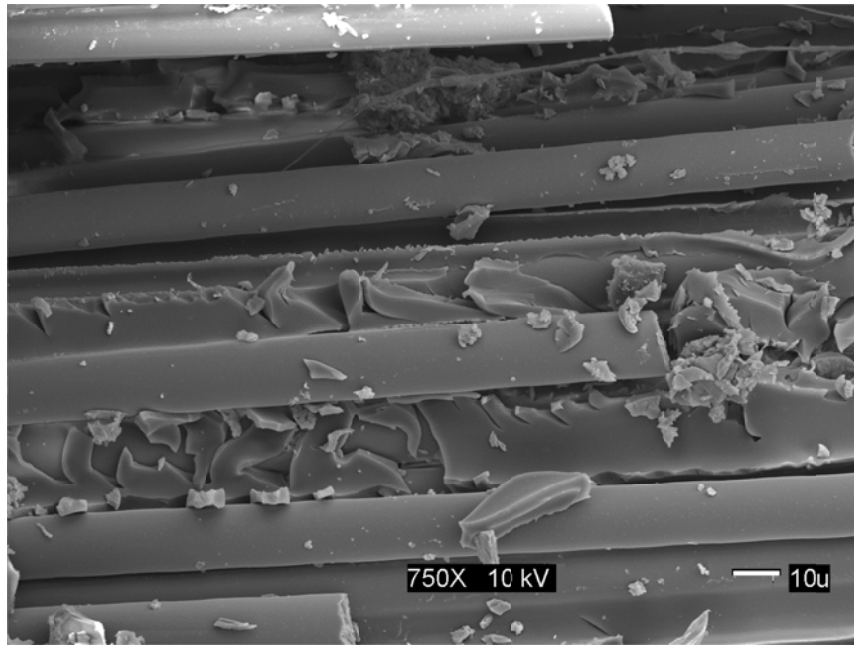


Figure 5-5: SEM image of unaged CFFT specimen.

Zero-stress aging is defined as the reduction of strength when no stress is applied during the time of exposure to a given environment. For determination of zero-stress aging, samples are aged in a given environment at constant moisture, and temperature, and then load-tested for strength. No load is applied during the time of exposure. The data is then fitted with the following expression:

$$\sigma(t) = \sigma_0(1 + \alpha t_a)^{-\beta} \quad [5.8]$$

where σ_0 is the strength at time zero, at the environment of exposure, α and β are empirical constants adjusted to fit the experimental data. A β value of 0.222 is recommended for E-glass/epoxy under water immersion (Barbero and Damiani, 2003). A summary of the constituent terms to Rosen's equation for each case is shown in Table 5-4:

Table 5-4: Parameters for the Rosen's equation.

α	β	Gm (Pa)	L (m)	m	df (μm)
1.67E-03	0.222	1.228E09	0.015	8.89	10

The data obtained from the axial compression test (section: 4.2.4) is used to study this methodology. Classical lamination theory and a finite element method (studied in Section 7.2) were used to distribute the stress on the laminate into the layers and into the appropriate orientations. The laminate was assumed to fail when one of the axial layers reached the predicted failure stress (first ply failure). That is, it was assumed that while the hoop layers contribute to the stiffness, they do not control the ultimate failure of the laminate when it is under compressive load.

Table 5-5 shows the predicted remaining compressive strength for ply 6 for two different fiber diameters (10 μm and 20 μm). Similarly, if the experimental data of unaged coupons and the approach described above are used, a stress of 1054 MPa for layer number six is obtained, as seen in Figure 5-6. Layer number six reaches the predicted failure stress at a strain value near to 0.018.

As the samples are aged at nominal zero stress, caution must be used by designers who may subject their materials to drastically different stress states during service life. The state of stress present in service conditions would also be more aggressive than the zero-stress state.

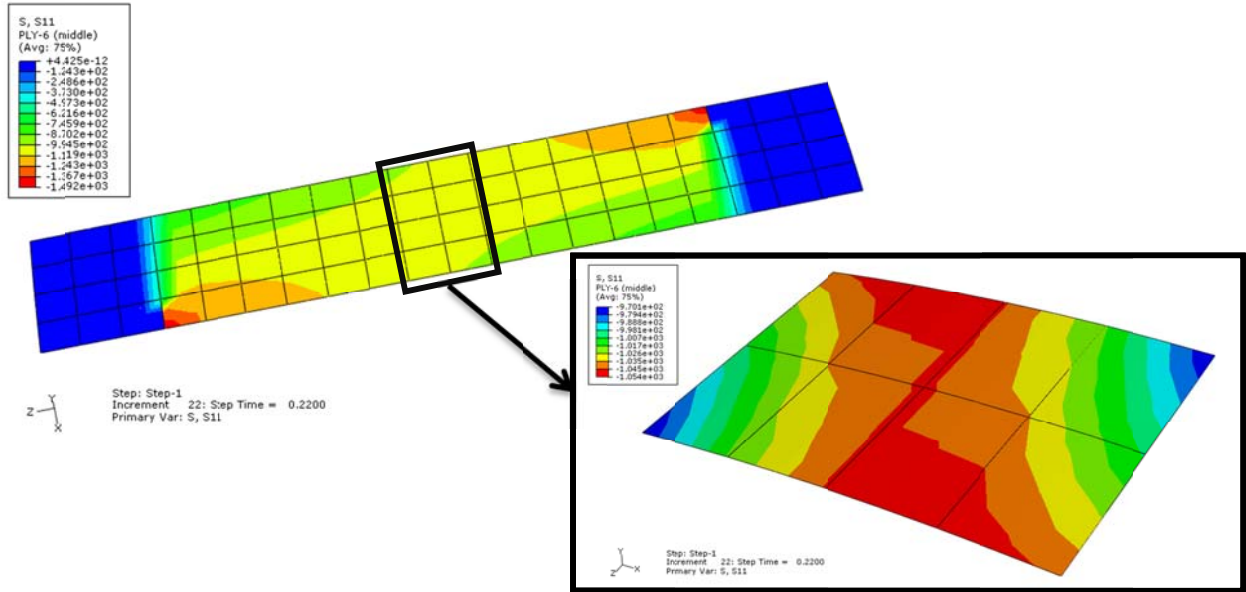


Figure 5-6: Axial stress at failure for ply 6.

Table 5-5: Remaining predicted compressive strength for ply 6.

Time (days)	Strength (MPa)	Strength (MPa)
	$d_f = 10 \mu\text{m}$	$d_f = 20 \mu\text{m}$
1 - unaged	1126.40	1041.91
10	1119.23	1036.86
100	1082.25	1004.07
1,000	897.98	834.29
10,000	588.39	547.40

Figure 5-7 shows the remaining strength obtained for ply 6 between 1 to 1000 days of aging using the methodology developed by Barbero and Damiani (2003). This methodology shows a strength reduction of 20% for the ply 6 after 1000 days of aging.

This methodology shows good agreements when extrapolated to the composite and compared with the shifted compression strength data obtained in the previous section, as seen in Figure 5-8. The trend obtained using this methodology agrees better with experimental data than the trend obtained in the previous section when Arrhenius approach was used.

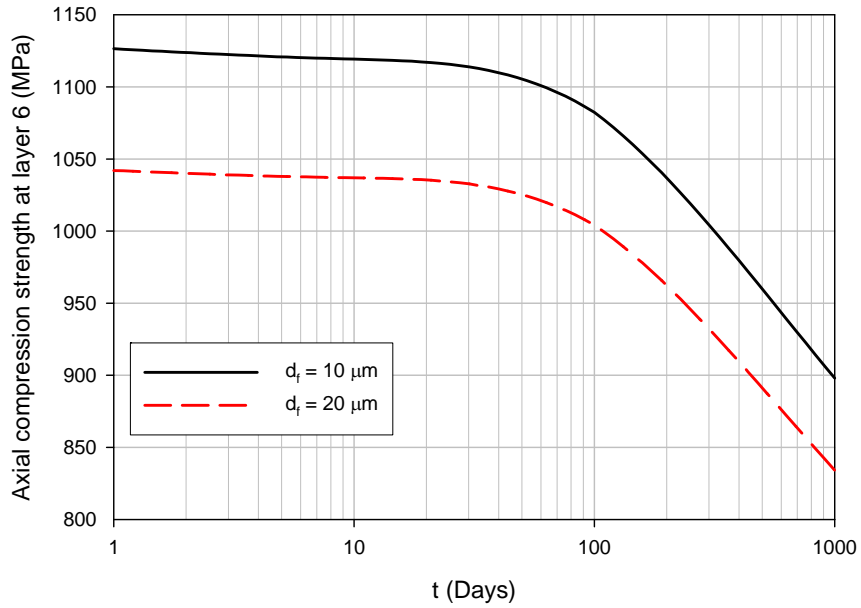


Figure 5-7: Predicted axial strength for ply 6 at different aging states.

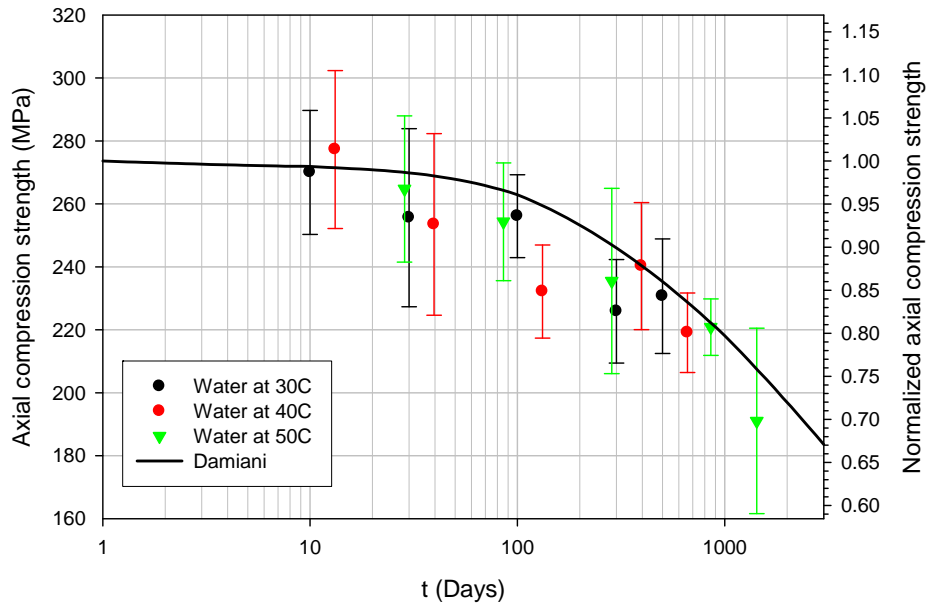


Figure 5-8: Shifted axial strength plot compared with Damiani methodology.

Zero-stress aging, which is negligible for short time and for low moisture content, becomes important at long times and high moisture. In addition, time and moisture degrade the fiber/matrix interphase, which results in longer debonding lengths and consequent further reduction of composite strength (Barbero and Damiani, 2003). The model presented by Barbero and Damiani (2003) and studied in this chapter incorporates the degradation of the fiber and interphase. Based on the results presented in this chapter, this model is also recommended to predict the long-term axial compression strength of composites.

CHAPTER 6

2-D NON-LINEAR FEM OF CFFT

6.1 Introduction

The model developed in the present study was generated and analyzed using ABAQUS[®] V6.6. The symmetry conditions of the system were considered, therefore axisymmetric elements were used. The model considers no friction between the two materials and uses the mechanical properties obtained from the experimental program for the specimen's FRP tube and concrete.

A monotonic compression load was applied to obtain the load-strain response. To simulate the rigid plate action exerted by the testing machine, a displacement constraint to the top nodes was used. Using probe elements located at the corresponding strain gauge position on the experimental specimens, field deformations from the model were acquired. The prediction of the system response for the FRP tube specimens is obtained and compared with the experimental data.

6.2 Constitutive Modeling of Concrete

Because the tests were performed under load control, the stress-strain data of unconfined concrete obtained from experiments have information only up to failure stress. Therefore it was necessary to understand the behavior of the concrete after peak stress levels.

The mechanical behavior of concrete after peak stress can exhibit two possible behaviors: nonlinear softening, or perfectly plastic. These two possible behaviors were analyzed in the finite element model (FEM) developed and are explained in this section.

6.2.1 Concrete constitutive model with softening

The independent continuum damage model (Faria, et al., 1998) was adopted to model the mechanical behavior of concrete when it experiences softening after peak strength. According to this method, the elastic properties of the material are uniformly degraded using a scalar damage variable “ d ”. Loss of secant stiffness in the material is represented by this variable, and it can take values from 0 (material without damage) to 1 (completely damaged material). This model has the following advantages:

- Represents the non-linear behavior of concrete with hardening and softening
- Considers separately the local damage due to tension and compression
- Lack of convergence problems in the integration process of the constitutive expression in finite element packages.

The model uses two internal variables of damage to characterize the local damage as traction (d^+) and compression (d^-) respectively. Therefore if a crack opens in tension and later the model is subjected to compression, the crack is closed and the concrete behaves as if it is uncracked.

The stress along the stress-strain curve is calculated with the following expression:

$$\sigma = (1 - d^-) \bar{\sigma}^- + (1 - d^+) \bar{\sigma}^+ \quad [6.1]$$

where $\bar{\sigma}^-$ and $\bar{\sigma}^+$ are the compression and tension effective stress tensors respectively. And d^- and d^+ are damage variables. The constitutive relationship for a general case is defined as:

$$\sigma = (1 - d^\pm) \bar{\sigma} = (1 - d^\pm) E \varepsilon = E_d \varepsilon \quad [6.2]$$

where E_d is the degraded secant modulus.

The explicit function of damage can be determined from the uniaxial response of the concrete in the hardening state using Equation 6.2. This response show a parabolic behavior as seen in Figure 6-1. The slope of the curve between O and P_1 is the initial concrete modulus E , and the point P_2 coincides with the concrete compressive strength f_p and ultimate axial strain ε_p . The following values were obtained from experimental stress-strain curves: elastic limit, $f_e = 3.50 \text{ MPa}$, $f_p = 17.50 \text{ MPa}$, and $\varepsilon_p = 0.028$.

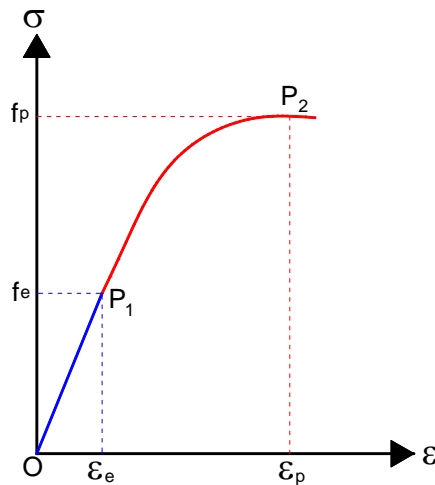


Figure 6-1: Parameters of stress-strain curve of concrete.

The following expression is used to obtain the value of the damage for a specimen of concrete subjected to compression load. The damage value d in the elastic zone ($\sigma < f_e$) is zero.

$$d^\pm = 1 - \frac{r_e^-}{r^-} \exp \left[\frac{1}{Bd^-} \left(\frac{1 - r_p^-}{r_e^-} \right) \right] \quad \forall r^- > r_e^- \quad [6.3]$$

where:

$$Bd^- = \frac{1}{2} \frac{r_p^-}{r_e^-} - E \frac{G_c}{(f_e^-)^2} + \bar{B}d^- \quad [6.4]$$

$$\bar{B}d^- = Ad^- \frac{\left[(r_p^-)^3 - 3r_p^- + \frac{2}{3} \right]}{6r_e^- (r_p^- - 1)^2} \quad [6.5]$$

$$Ad^- = \frac{r_p^- - r_e^-}{r_e^-} \quad [6.6]$$

$$r_e^- = \frac{f_p^-}{f_e^-} \quad [6.7]$$

$$r_p^- = \frac{E \cdot \varepsilon_p^-}{f_e^-} \quad [6.8]$$

Variable r^- is current damage threshold, which controls the size of the expanding damage surface. Therefore, this variable is a function of the strain level in the concrete, where r_e^- is the damage threshold when the ultimate strength of the concrete is reached.

The curve shown in Figure 6-2, $r^- = f(\varepsilon_{axial})$, was adjusted to obtain reasonable agreement between the model and the experimental data. This comparison between the curves is shown in Figure 6-3.

Using the expression 6.9 the calibration parameter G_c is varied gradually so that for a specific deformation of 10% ($d = 0.999$) the concrete reaches a strength similar to compacted gravel. An initial value of 0.014 for G_c^0 is recommended by Gerbaudo and Prato (2004).

$$G_c = G_c^0 + \frac{G_c^0(r^- - r_e^-)}{1 + \frac{G_c^0(r^- - r_e^-)}{3.5}} \quad \forall \quad r^- > r_e^- \quad [6.9]$$

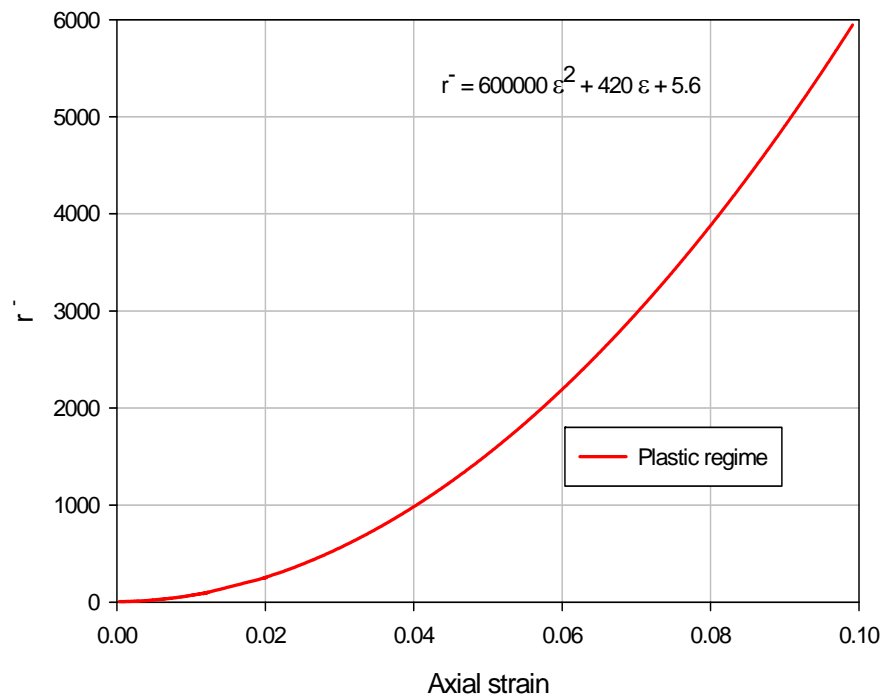


Figure 6-2: Damage threshold curve.

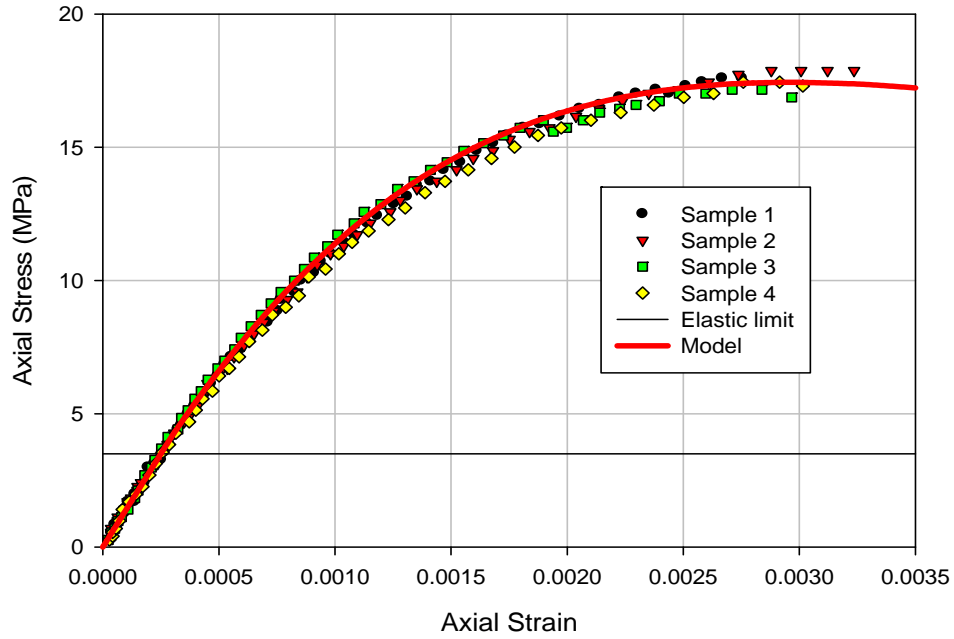
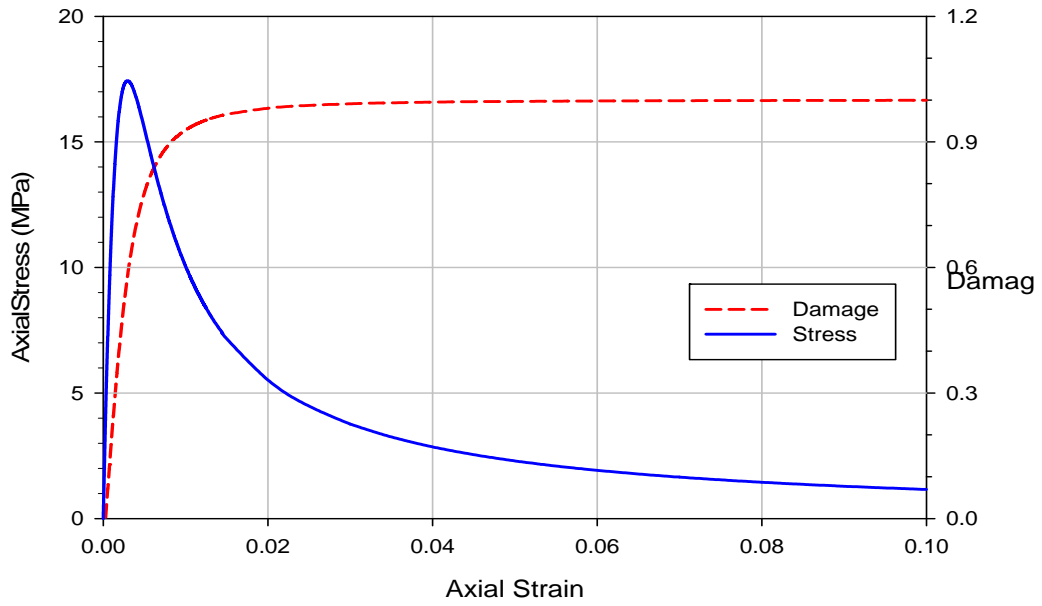
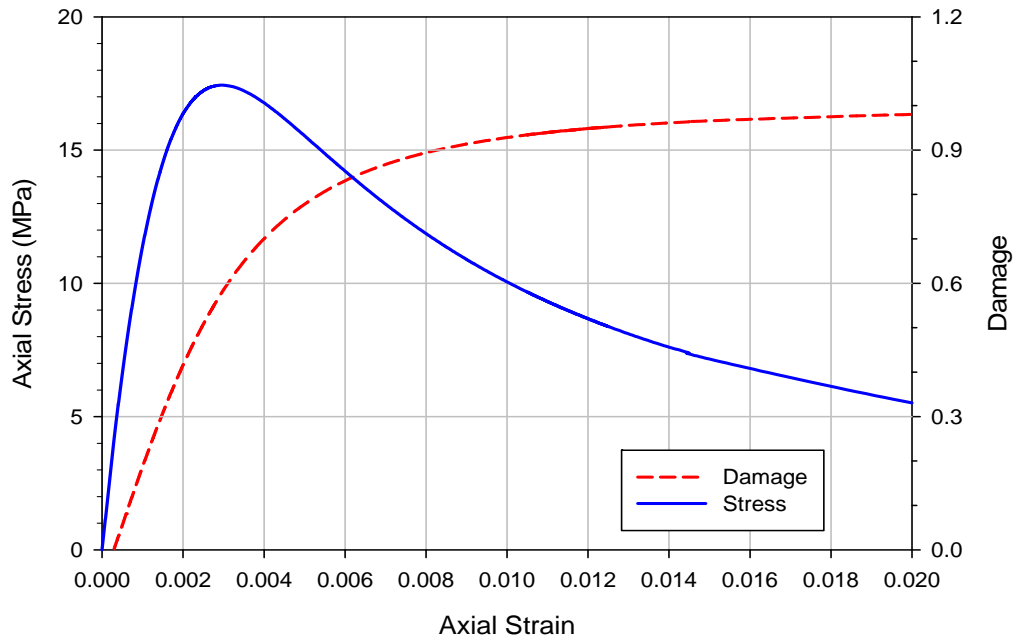


Figure 6-3: Comparison of experimental data and the analytical model.

Figure 6-4 shows the analytical stress-strain curve for concrete. This curve also includes the damage in the concrete core as a function of the axial strain. The damage value is approximately equal to 1.0 for an axial strain of 0.10 on the concrete. The damage value, d in the elastic zone ($\sigma < f_e=3.5$) is zero.



(a) Complete curves.



(b) Enlargement of the initial part of the curves.

Figure 6-4: Analytical curve for concrete with softening.

6.2.2 Concrete constitutive model with perfect plasticity

The stress-strain behavior of the concrete was modeled using the analytical model discussed previously up to peak stress ($f_p^- = 17.50\text{MPa}$), followed by a segment of perfectly plastic material (without degradation) up to failure (Figure 6-5). This assumption implies that the confined concrete will have a damage maximum value of approximately 0.6 once its peak strength is reached.

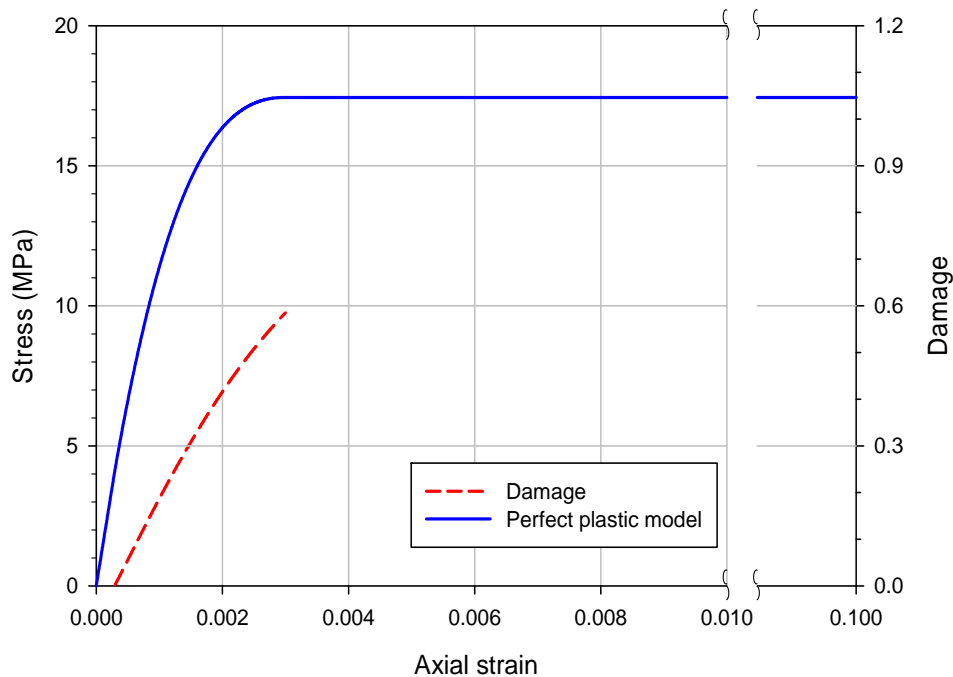


Figure 6-5: Analytical curve for concrete with perfect plasticity behavior.

Elastic-perfectly plastic model was used in the present study, based on results obtained by Patsch et al. (2002), and Bruneau and Marson (2004). This model assumes that the tube is capable of confining the concrete to a level such that the stress coincides with the unconfined stress in the concrete f'_c . After that point, this stress is sustained through large deformations until the tube fails.

6.2.3 Drucker-Prager model in ABAQUS

A linear elasticity model was used for the initial stage of the concrete compressive behavior. The elastic properties are completely defined from the Young's modulus, E , and the Poisson's ratio, ν . These properties were obtained from uniaxial compression test for the unconfined concrete used to fill the FRP tubes.

The initial stage is defined as the zone where the stress-strain curve of the concrete is linear. This zone was established for a stress below 3.5 GPa and with an initial modulus of 14 GPa. Figure 6-6 shows the values obtained using the experimental stress-strain curve.

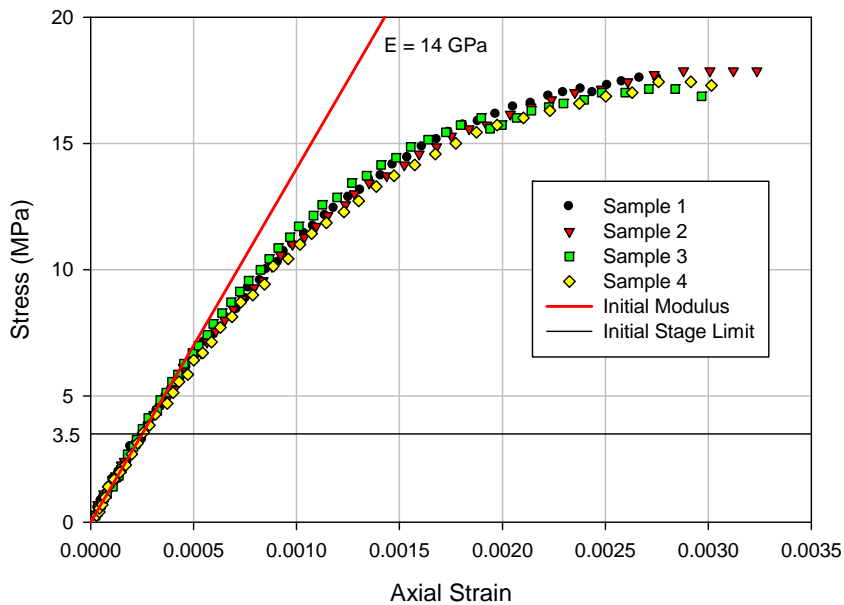


Figure 6-6: Initial modulus for unaged concrete.

Once the maximum stress of the linear range is reached, the Drucker-Prager model becomes active for the non-linear portion. Drucker-Prager (DP) is an isotropic plasticity model composed of a yield criterion and a plastic flow rule that controls the behavior beyond the elastic limit. DP is useful to model the stress-strain behavior of the confined concrete which exhibits pressure-dependent yield (the material becomes stronger as the pressure

increases). Its formulation is relatively simple because it only two parameters are necessary to define the yield surface and one more to define the plastic flow rule. Because of its simplicity, this model is widely used by engineers and it is implemented in many commercial finite-element codes (Lopez, 2002).

Additionally, there are three main concrete constitutive models available in ABAQUS. Each can be used for modeling concrete at low confining pressures in all types of elements. Smearred crack concrete model is intended for applications “in which the concrete is subjected to essentially monotonic straining”. Brittle cracking model is intended for applications in which “the concrete behavior is dominated by tensile cracking and compressive failure is not important”. Concrete damaged plasticity model “takes into consideration the degradation of the elastic stiffness induced by plastic straining both in tension and compression. It also accounts for stiffness recovery effects under cyclic loading.”

The data from triaxial testing for the concrete used in this study is available in Flores (2009). The study performed by Flores (2009) includes stress-strain curves at different levels of confinement. The internal friction angle reported in this study was 34.5° using the failure criteria of Mohr-Coulomb. The Mohr-Coulomb failure model is based on plotting Mohr's circle for states of stress at failure in the plane of the maximum and minimum principal stresses.

In order to match triaxial data, one stress data point at failure from each stress-strain curve at different level of confinement is plotted in the meridional stress plane ($p-t$ plane). This technique calibrates the shape and position of the yield surface, as shown in Figure 6-7, and is adequate to define a model if it is to be used as a perfect plasticity failure surface

(ABAQUS, 2006). From Figure 6-7 the material angle of friction was established, $\beta=53^\circ$, in the $p-t$ plane.

The Drucker-Prager models are also available with isotropic hardening, in which case hardening data are required to complete the calibration. In an isotropic hardening model plastic flow causes the yield surface to change size uniformly; in other words, the stress-strain curves depicted in Figure 6-6 can be used to represent hardening. Figure 6-8 shows the Drucker-Prager hardening curve given to the ABAQUS model for a concrete constitutive model with perfect plasticity.

The hardening curve used in the DP model should be established in terms of true stress and absolute plastic strain. These values can be calculated using the following equations respectively (ABAQUS, 2006):

$$\sigma_{true} = \sigma_{nominal} (1 + \varepsilon_{nominal}) \quad [6.10]$$

$$\varepsilon_{abs}^{pl} = \ln(1 + \varepsilon_{nominal}) - \frac{\sigma_{true}}{E} \quad [6.11]$$

Where the nominal values are measured from the experimental tests and E is the initial modulus of the concrete.

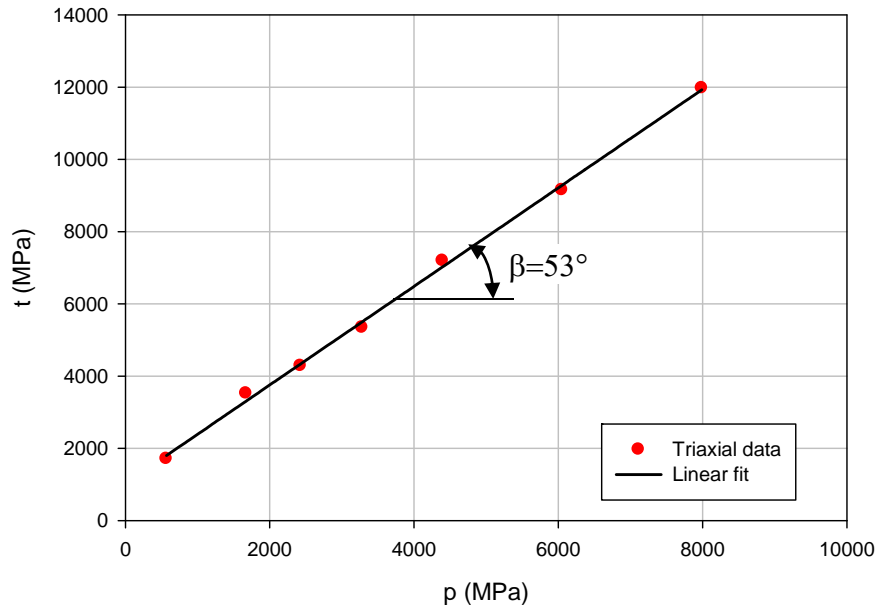


Figure 6-7: Yield surface in meridional plane for unaged concrete.

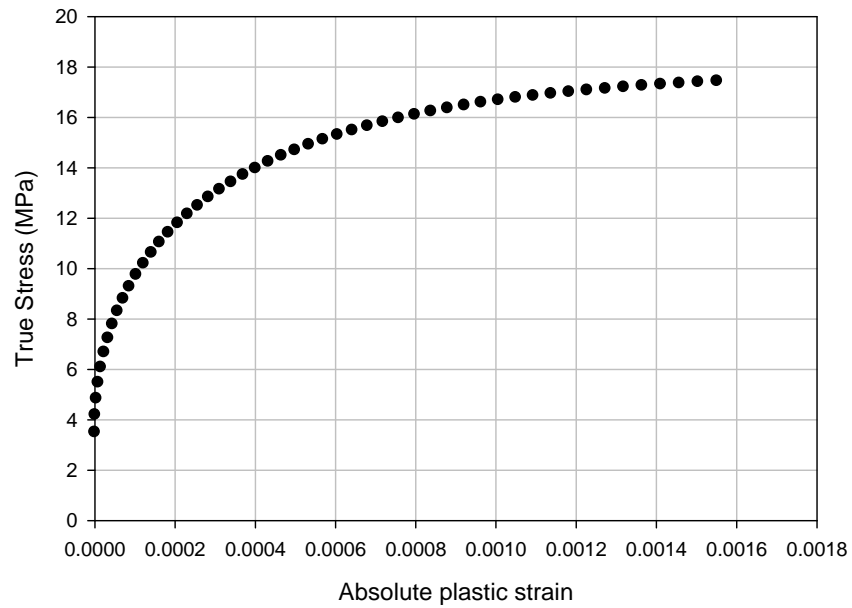


Figure 6-8: Drucker - Prager hardening curve.

6.3 FRP Tube

The FRP material was modeled as an equivalent orthotropic layer in two orthogonal principal directions with linear elastic behavior. Table 6-1 shows the mechanical properties of the material that were used as the “engineering constants” for the three modulus E_1 , E_2 , E_3 ; the poisson’s ratios ν_{12} , ν_{13} , ν_{23} ; and the shear modulus G_{12} , G_{13} , G_{23} , associated with the principal directions of the material. Where E_1 , E_2 , ν_{12} , G_{12} , correspond to the experimental values measured in the present study for the FRP tube. The other properties were assumed since they are not used in the analysis but required by the software.

Table 6-1: Experimental engineering constants for GFRP tubes.

E_1 (MPa)	E_2 (MPa)	E_3 (MPa)	ν_{12}	ν_{13}	ν_{23}	G_{12} (MPa)	G_{13} (MPa)	G_{23} (MPa)
20000	30000	30000	0.26	0.26	0.26	3219	3219	3219

6.4 Concrete Filled FRP tubes (CFFT)

Figure 6-9 shows the actual finite element mesh used to model the concrete-filled FRP tube system. Due to the axisymmetry of the system, only a planar area projection for the concrete core and a wire for the FRP tube were used to model the continuum solid and shell of revolution.

The mesh part for concrete core and FRP shell were created in the model to define an output history in any element of the mesh. Probe elements were defined to extract the results through the analysis history.

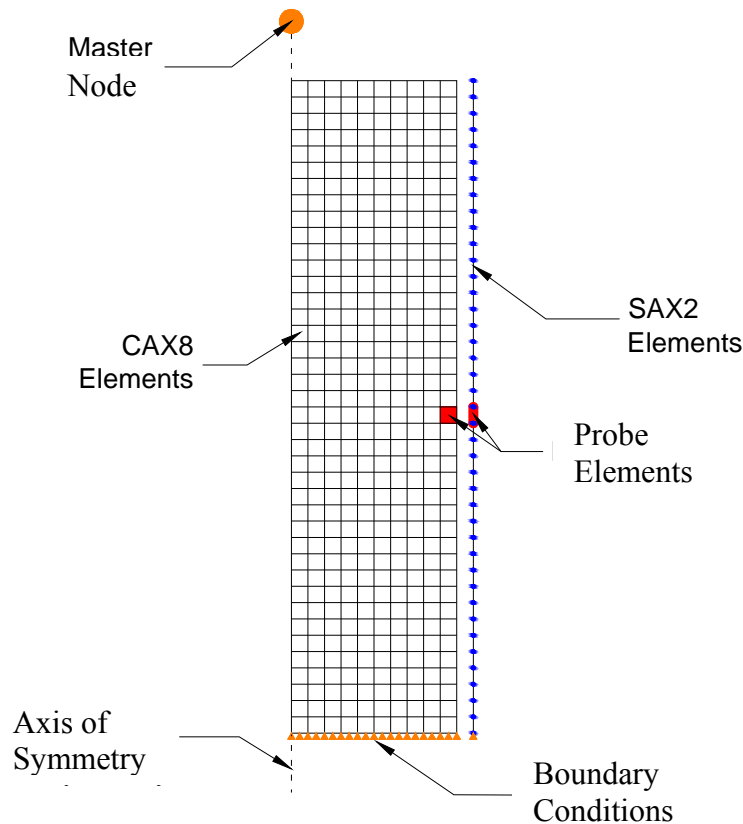


Figure 6-9: Axisymmetric finite element mesh used for the concrete-filled FRP model.

Friction and initial gap between the concrete core and tube was ignored. To account for the possibility of separation of the concrete and the tube, surface to surface contact rule was used. Master and slave surfaces were defined, having the concrete core as master surface and the FRP tube as the slave surface.

Abaqus has two definitions in the interaction module for the mechanical contact: Tangential Behavior and Normal Behavior. The tangential behavior includes different friction formulations, the formulation used in this study was *frictionless*. This formulation is selected for surfaces that are to slide freely without friction. In addition, the node of each surface can have different degrees of freedom. Therefore the contact surfaces were defined *frictionless* in the model with a formulation of *small sliding*.

For geometrically nonlinear analyses, *small sliding* formulation assumes that the surfaces may undergo arbitrarily large rotations but that a slave node will interact with the same local area of the master surface throughout the analysis. For geometrically linear analyses, the small-sliding approach reduces to an infinitesimal-sliding and rotation approach, in which it is assumed that both the relative motion of the surfaces and the absolute motion of the contacting bodies are small (ABAQUS, 2006).

The axial compression test was modeled using a displacement control method. This consists of the application of user defined displacement amplitude to a master node from which the reaction load of the system can be obtained. This node is linked to the top nodes of concrete core and FRP shell to allow an equal displacement of both edges. This method allows to simulate the effect of the rigid loading surfaces of the compression test machine used in the experiments.

The FRP tube was modeled using shell SAX2 elements with 3-node quadratic axisymmetric formulation. The concrete core was modeled using continuous quadrilateral CAX8 elements with 8-node biquadratic axisymmetric formulation. The CAX8 element allows the incorporation of the nonlinear material properties of the concrete including plastic deformations and creep. The FRP SAX2 allows either thin or thick shell behavior with a homogeneous section.

6.5 Results

Results of the FE Analysis, in terms of axial load versus axial and lateral strain are presented in Figure 6-10. These results are compared with experimental data of unaged specimens. The experimental data presented in the figure for the concrete filled FRP tubes

corresponds to tests of the experimental program. Good agreement between finite element model and the unaged experimental results was found using the friction angle ($\beta=53^\circ$) obtained from the test developed by Flores (2009). Three different dilation angles ($\delta=20^\circ, 10^\circ$ and 5°) were used to obtain the response of the system under compressive load. The responses using the three different dilation angles (δ) were practically the same, having all curves one on top of each other.

Figure 6-10 also shows a softening behavior near the compressive strength of the unconfined concrete when the softening curve shown in Figure 6-4 is used. This is because the curve that represents hardening most accurately over the range of loading conditions anticipated should be selected (usually the curve presented in Figure 6-5). FE models with degraded properties are studied in the next chapter.

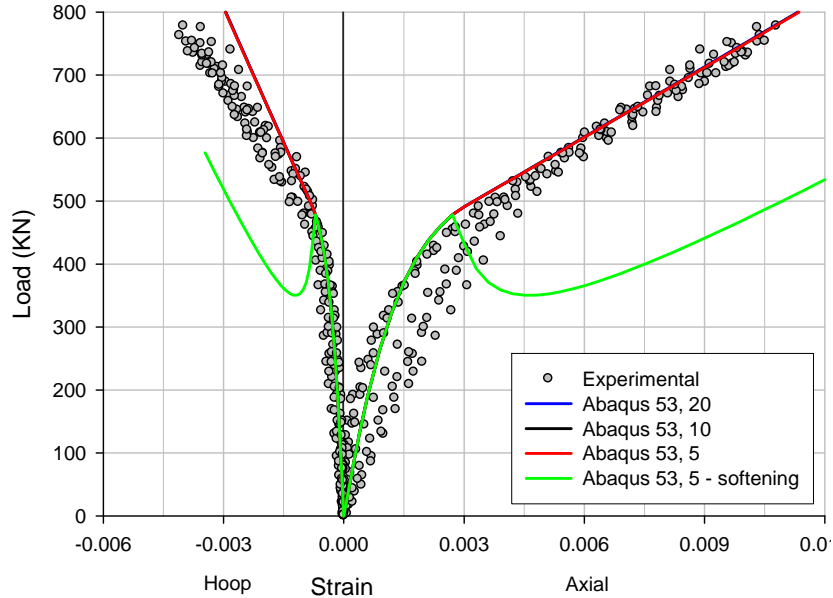


Figure 6-10: FEM and experimental results for unaged concrete filled FRP tubes.

CHAPTER 7

3-D NON-LINEAR FEM OF CFFT

7.1 Introduction

The model developed in the present chapter was generated and analyzed using ABAQUS® V6.6. The FRP shell was modeled as laminated; therefore, it was necessary to provide the mechanical properties of every lamina. These properties were presented in Table 3-3. Figure 7-1 shows the ply stack plot obtained for the composite shell once the properties for each lamina are provided to ABAQUS.

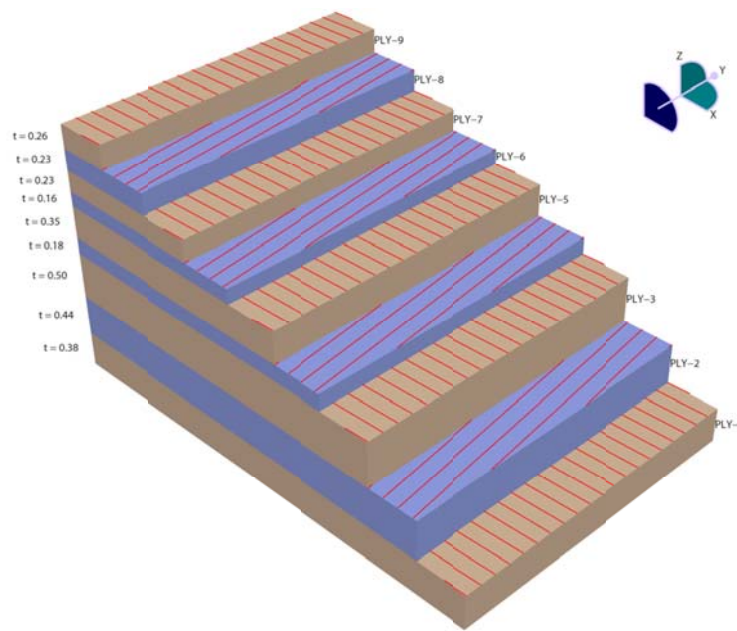


Figure 7-1: Ply stack plot from Abaqus.

7.2 FRP Tubes Modeling

Hoop tension test, axial tension test, axial compression test and axial compression tube test were simulated using 3-D linear FE models in Abaqus. The laminated properties reported in Table 3-3 were validated comparing the experimental data with the results from the simulation. After the validation, the properties were used with the confidence to perform the 3-D FE model of CFFT.

7.2.1 Hoop test

The model generated in Abaqus had the same geometry as the real specimens. The mechanical properties applied to each layer are the ones reported in Table 3-3. Thickness of each layer is as reported in Table 3-2.

The mesh used to simulate the hoop test is shown in Figure 7-2. This ring was modeled as a multilayered shell with three integration points per layer through the entire shell thickness. The shell was exposed to internal pressure and the response was monitored in specific elements in order to obtain the stress-strain curve presented in the Figure 7-3.

Figure 7-3 compares the predicted stress-strain curve from the FE Model with the experimental data. These results show the typical fiber-dominated linearity at the beginning of the test, followed by a slight nonlinearity. The nonlinearity is principally attributed to: the fiber strength is not uniform and some fibers fail at stresses well below the ultimate composite strength (Gibson, 1994). The predicted hoop stiffness is 31.4 GPa.

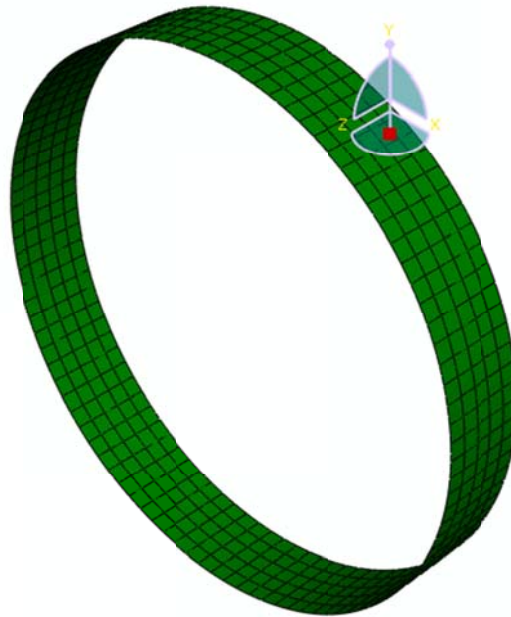


Figure 7-2: Finite element mesh used for the Hoop test model.

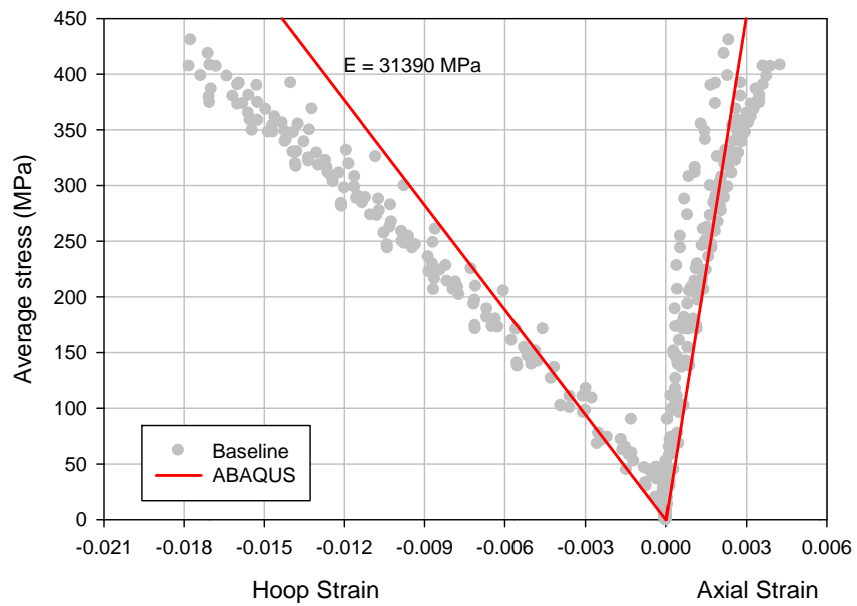


Figure 7-3: Comparison of FEA and experimental results from axial hoop test.

7.2.2 Axial test

The FE Model was dimensioned based on the coupon sizes, including the given curvature. The mechanical properties applied to each layer are the ones reported in Table 3-3 and the thickness reported in Table 3-2.

Figure 7-4 shows the mesh used to simulate the axial test. Shell elements were used with three integration points per layer through the entire shell thickness. The shell was subjected to axial load and the response was monitored in specific elements at the center of the coupon. The predicted stress-strain curves and the experimental data are presented in Figure 7-5 and Figure 7-6.

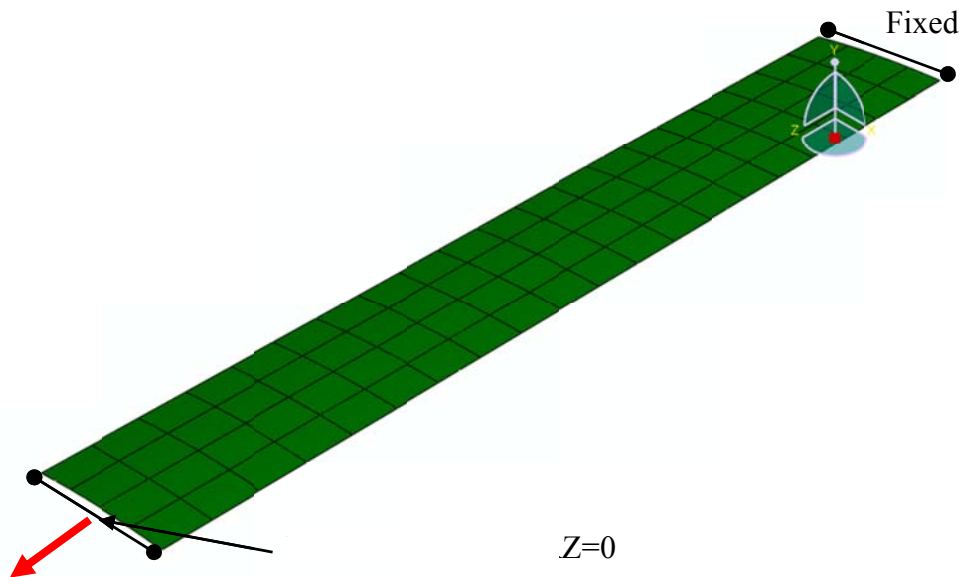


Figure 7-4: Finite element mesh used for the axial test model.

Figure 7-5 shows the stress-strain curve generated from the FE Model compared with the experimental data obtained from the axial tension test. Figure 7-6 shows the stress-strain curve generated from the FE Model compared with the experimental data obtained from the axial compression test. Again, the initial behavior of the FE model is similar to the

experimental data up to a stress close to 50% of the strength (linear elastic behavior). After this point the experimental data shows a stiffness change principally in the axial tension test. The predicted axial stiffness is 22295 MPa.

Degradation of stiffness can be attributed to material damage. It plays an important role in the analysis of FRP materials because many such materials exhibit elastic-brittle behavior. Damage in these materials is initiated without significant plastic deformation. The failure modes considered are fiber rupture in tension and fiber buckling and kinking in compression (Gibson, 1994).

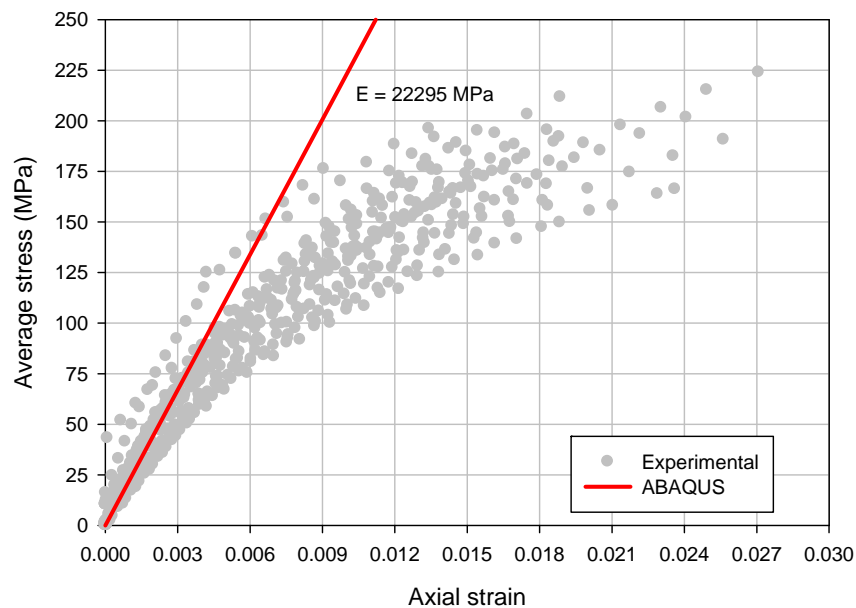


Figure 7-5: Comparison of FEA and experimental results from axial tension test.

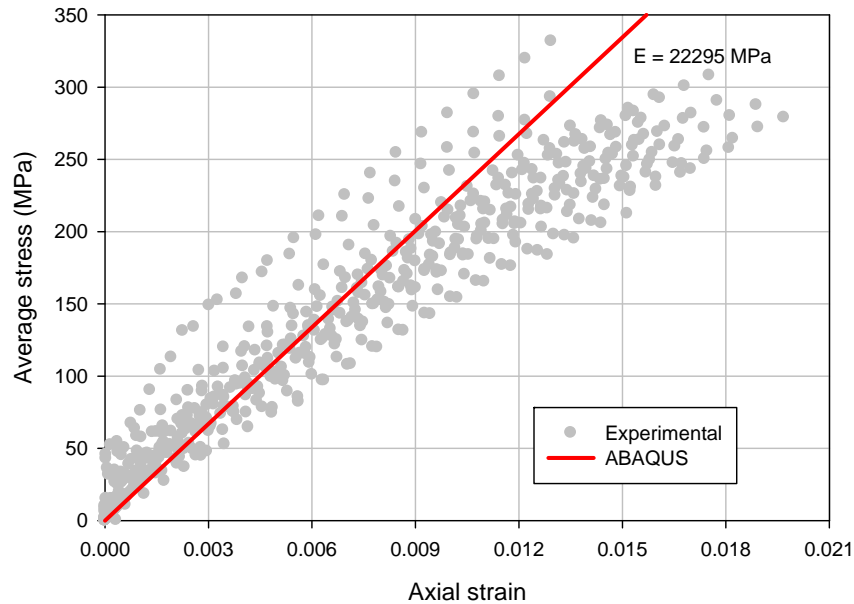


Figure 7-6: Comparison of FEA and experimental results from axial compression test.

7.2.3 FRP tube compression test

Similar to the previous models, full size mesh was generated matching the specimen geometry with the material properties and layout reported in Tables 3-2 and 3-3.

Figure 7-7 shows the model generated in Abaqus. Shell elements were used with three integration points per layer through the entire shell thickness. Monotonic compressive load was applied to generate the load-strain response in the FRP tube. In order to simulate the rigid plate action exerted by the testing machine, a displacement constraint to the top nodes of the tube was used. Results were extracted from probe elements located at the position of the strain gauge on the specimens.

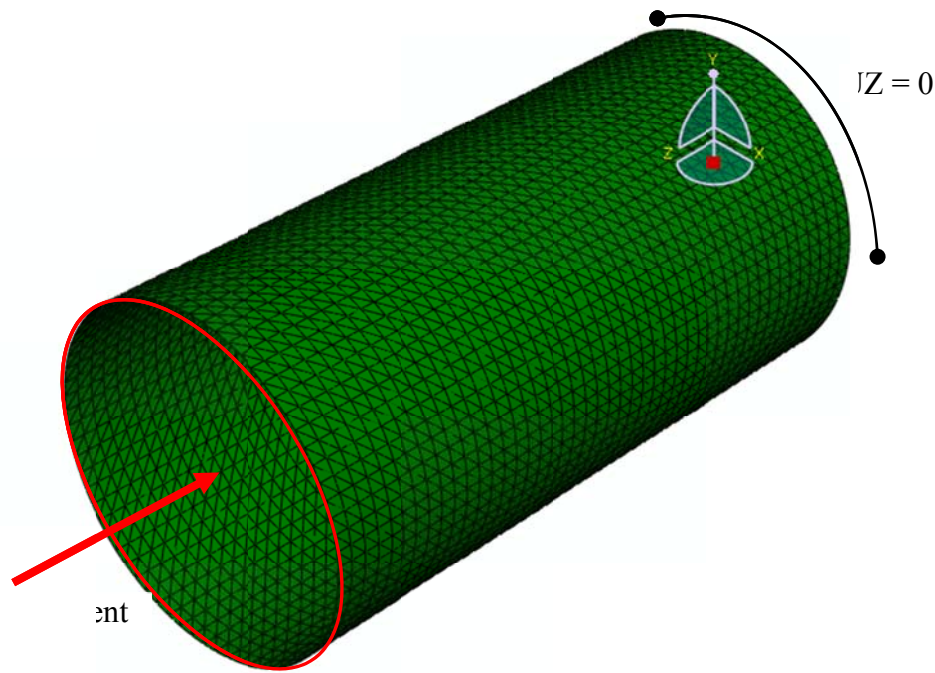


Figure 7-7: Finite element mesh used for the FRP tube model.

Prediction of the response for the FRP tube specimens were obtained and compared to the experimental data in Figure 7-8. The behavior of the FE model is similar to that obtained experimentally. This time the experimental data showed a linear behavior of the FRP through the test.

Figure 7-9, 7-10, 7-11 and 7-12 show the stress for those plies where the fiber is oriented along the tube at experimental failure load. Additionally, the FE model predicts stress concentration at the ends of the tubes as was observed experimentally by end crushing.

An elastic stability analysis was performed on the FRP tubes to verify if local buckling was an issue to consider. A buckling load of 560 KN was predicted from a geometrical non-linear FE analysis developed as seen on Figure 7-13. This figure shows the deformed shape for the tube when the buckling load is reached. It was found that the buckling load is higher

than the failure load. This means that material failure is reached before buckling as observed in the experiments.

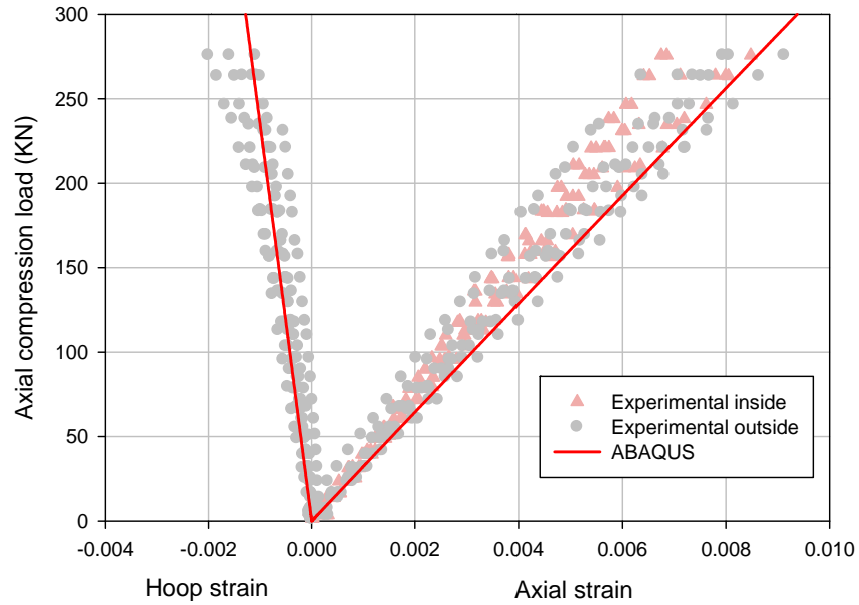


Figure 7-8: Comparison of FEA and experimental results from FRP tube test.

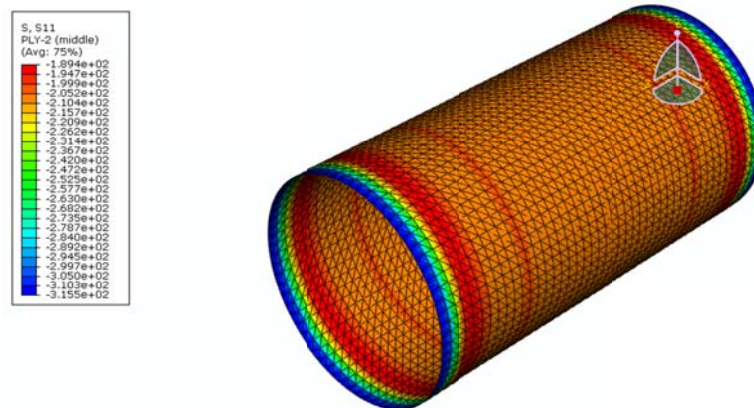


Figure 7-9: Stress S1 on Ply 2 (8°) at experimental failure load.

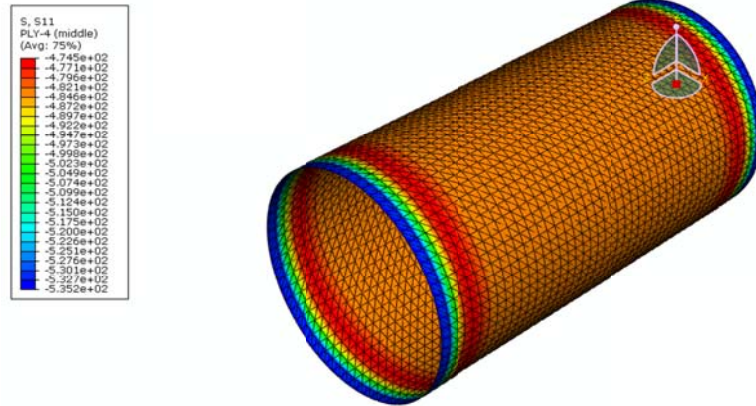


Figure 7-10: Stress S1 on Ply 4 (8°) at experimental failure load.

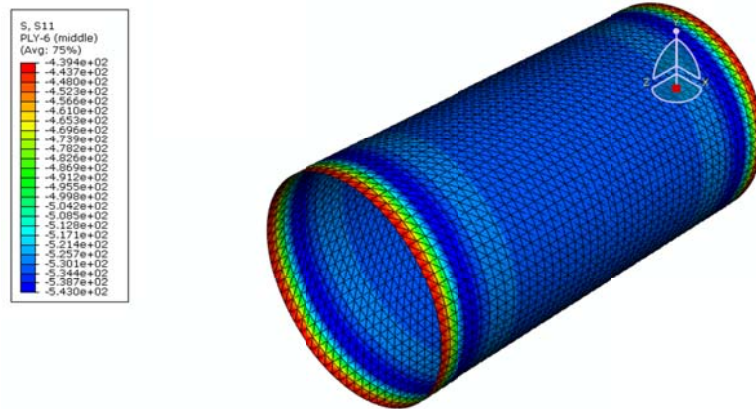


Figure 7-11: Stress S1 on Ply 6 (8°) at experimental failure load.

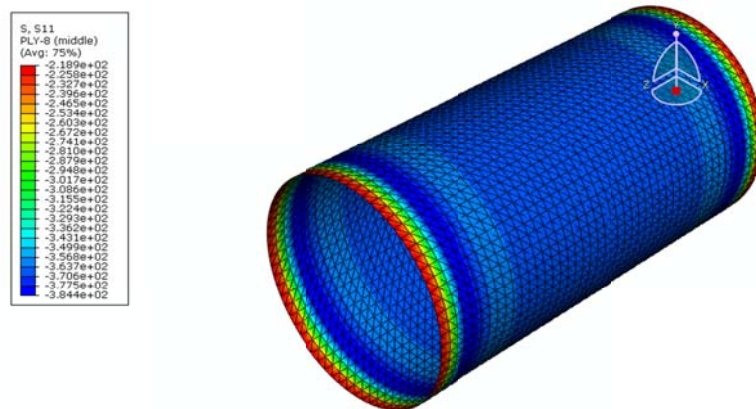


Figure 7-12: Stress S1 on Ply 8 (8°) at experimental failure load.

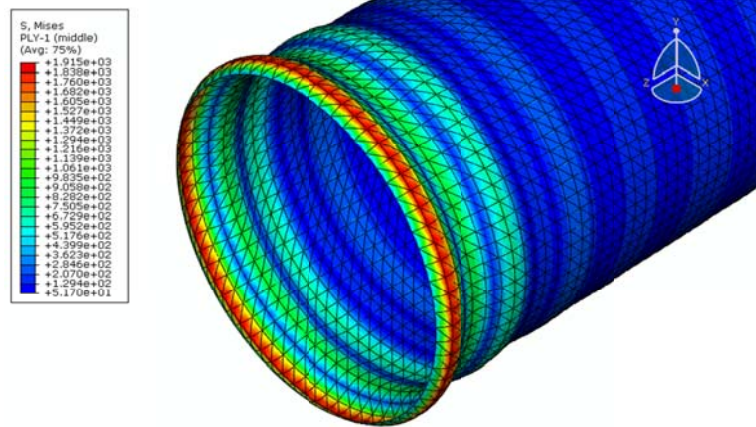


Figure 7-13: Deformed shape at buckling load.

7.3 Concrete filled FRP tubes (CFFT)

A 3-D FE model was developed for the concrete filled FRP tubes. Figure 7-14 and Figure 7-15 show meshes for the FRP tube and concrete core respectively. The tube was modeled with triangle shell elements with the same characteristics of the coupon models, including layers and material properties from Table 3-2 and 3-3. These properties are the same for the unaged (baseline) and for aged (500 days) tubes because the composite showed negligible change in modulus with aged time (presented in Chapter 4). The boundary conditions are the same as presented in Chapter 6 for the 2-D model.

The FRP tube was modeled using STRI65 elements: 6-node triangular thin shell, using five degrees of freedom per node. The concrete core was modeled using continuous quadrilateral C3D20 elements, 20-node quadratic brick. The C3D20 element allows the incorporation of the nonlinear material properties of the concrete including plastic deformations and creep. The FRP STRI65 allows the thin shell behavior with a composite section.

Both meshes shown in Figure 7-14 and Figure 7-15 were analyzed together. To account for the possibility of separation between the concrete core mesh and the FRP tube mesh, a surface to surface contact was established between these two materials. Master and slave surfaces were defined, having the surface of the concrete core as the master surface and the internal surface of the FRP shell as the slave surface. Friction between the concrete core and tube was ignored. A *frictionless* formulation without initial gap was defined.

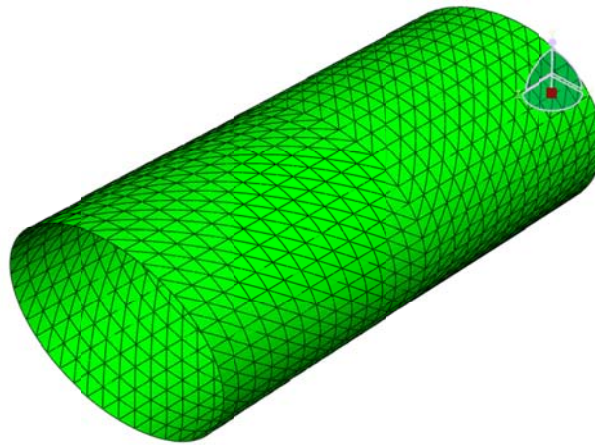


Figure 7-14: FRP tube mesh.

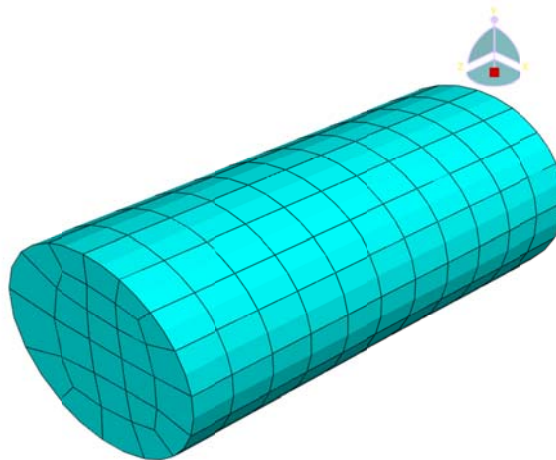


Figure 7-15: Concrete core mesh.

Also *small sliding* formulation was used in the contact definition between the tube and the concrete core. For geometrically nonlinear analyses, this formulation assumes that the surfaces may undergo arbitrarily large rotations but that a slave node will interact with the same local area of the master surface throughout the analysis (ABAQUS, 2006).

The concrete non-linearity was modeled using the Drucker-Prager (DP) linear model as mentioned in Chapter 6. For granular materials the linear Drucker-Prager model is normally used with nonassociated flow in the $p-t$ plane, in the sense that the flow is assumed to be normal to the yield surface in the π -plane but at an angle δ to the t -axis in the $p-t$ plane, where usually $\delta < \beta$. β is the slope of the linear yield surface in the $p-t$ stress plane and is also commonly referred to as the friction angle of the material. Associated flow results from setting in Abaqus $\delta = \beta$. The original Drucker-Prager model is also available in Abaqus by setting $\delta = \beta$. Nonassociated flow is also generally assumed when the model is used for $\delta = 0$, the inelastic deformation is incompressible; if $\delta > 0$, the material dilates. Hence, δ is referred to as the dilation angle.

Force and axial and hoop deformation were extracted from the FE model to be compared with the experimental data. This comparison is reported in Figure 7-16. Good agreement between finite element model and the experimental data is observed using the friction angle 35.5° (ϕ) reported by Flores (2009) using Mohr-Coulomb failure model and dilation angle (δ) desired for this particular case.

The FEM results for unaged specimens were obtained from a parametric study performed to evaluate the sensibility of the response to the effect of the dilation angles. This procedure consists in using several dilation angles for the given friction angle in order to

obtain the best axial and lateral response. The best friction angle (β) and dilation angle (δ) combination found was 53° and 5° for the axial and lateral response.

Similarly, The FEM results presented in Figure 7-17 for concrete filled FRP tubes (CFFT) after being submerged for 500 days in water were obtained. For this case the best friction angle (β) and dilation angle (δ) combination found was 53° and 50° respectively.

The average peak strength unconfined concrete (unaged) obtained by Flores (2009) was 11.8 MPa. This value is similar to that obtained in this study for unconfined concrete after 500 days of aging. Unfortunately, triaxial test was not performed for submerged specimens in the study developed by Flores (2009). Results show a better predictions of lateral response for the 500 days aged CFFT.

The axial response obtained for both, aged and unaged models show higher susceptibility to the dilation angle (δ) than the lateral response. Similar results were obtained by Mirmiran, et al. (2000). This susceptibility is higher for the unaged than for aged specimens (higher concrete strength). Additionally, the results show good agreement with the experimental data using dilation angle (δ) higher than zero, $0 < \delta < \beta$. The results presented by Mirmiran, et al. (2000) showed that for the range of concrete strengths in his study (29.6 - 32.0 MPa), best results can be expected by setting dilation angle to 0° (incompressible). The conclusion presented by Mirmiran, et al. (2000) for these results was: “it appears that the Drucker-Prager plasticity cannot fully capture all facets of the response of FRP-confined concrete, and further improvements on the modeling of the yielding surfaces are necessary”. The yield surface was improved in this study by adding a hardening curve to the Drucker-Prager plasticity model.

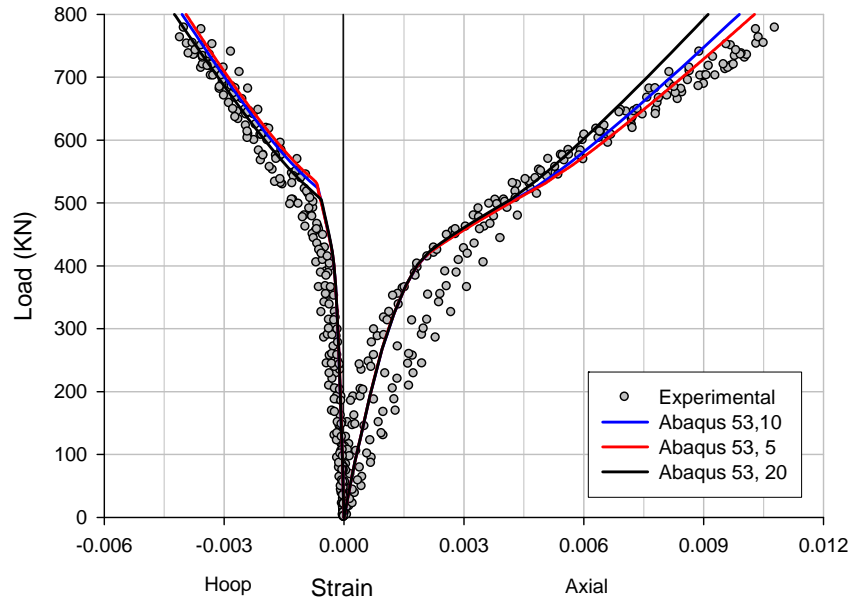


Figure 7-16: Comparison of FEA and unaged experimental results for CFFT.

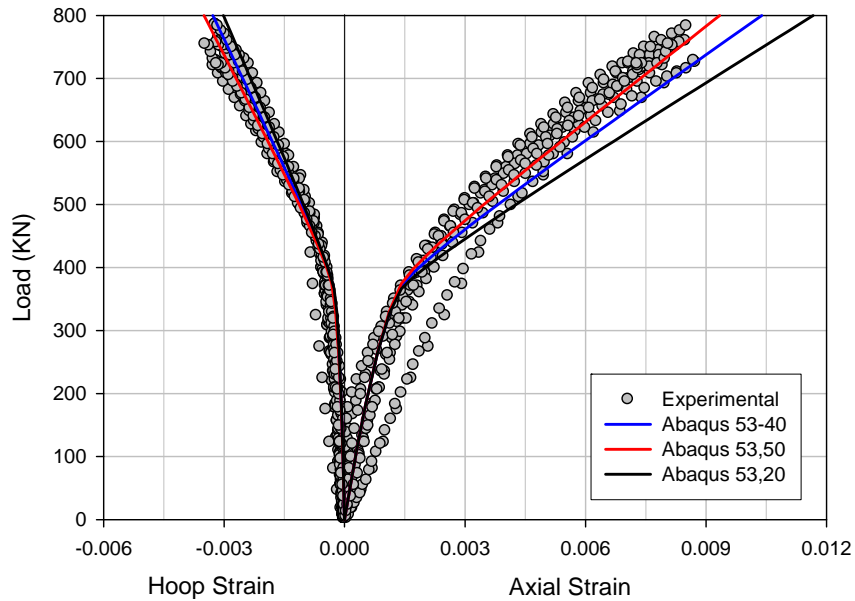


Figure 7-17: Comparison of FEA and 500 days aged experimental results for CFFT.

The good agreement between finite element model and the experimental results were obtained also thanks to use of contact elements between the concrete core and the FRP shell. This methodology adds an additional non linearity to the model. The time taken to solve the FE model is increased due to the convergence problems caused for this non-linearity. If contact is used to model this type of structural system, real values for the properties of both materials can be used. Additionally, it is not necessary to use high Poisson ratios or lower elastic modulus for the concrete in order to adjust the results. The number of iterations needed in order to find the correct value for friction angle (ϕ) and dilation angle (δ) are very low, and similar results were obtained for typical values used for concrete.

Additionally, the FE model allows to identify when the confinement effect of the FRP tube is activated. As the concrete core can sustain additional compression load beyond the unconfined compression strength thanks to the confinement provided by the FRP shell, the model also can predict the confinement pressure on the concrete for any interest point. All the information obtained from these calibrated FE models is helpful because it allows to understand behaviors that are not easy measurable experimentally, for example as the variable confinement pressure can be obtained at different loads.

CHAPTER 8

CONFINEMENT MODEL OF CFFT

8.1 INTRODUCTION

Over the last decades, the traditional steel jacketing showed to be an effective technique for retrofitting of conventional reinforced concrete columns and it has been widely used in practice. Experimental works have demonstrated that, in concrete filled circular steel columns, very little interaction exists between concrete and steel (Furlong, 1967). This behavior occurs because the concrete has a smaller Poisson's ratio than steel. Due to this effect, the steel jacket and the concrete core are separated if both materials are submitted to the same axial strain. As a result, such a column can fail by longitudinal yielding of the steel.

Recently, the use of composite materials, especially fiber-reinforced polymers (FRP), has been recognized as a reliable retrofit technique for reinforced concrete elements. This material can be used to provide confining to circular columns of concrete because, when the composite member is put under concentric compression, the circumferential stiffness of the FRP casing inhibits lateral strains and microcracking in the concrete core.

The separation between the concrete core and the FRP jacket in this case can be avoided if the FRP is designed with a Poisson's ratio below 0.2 (concrete Poisson's ratio).

Additionally, low Poisson's ratio in the FRP produces a better confinement to the concrete. The expected failure mode of these systems is fracture of the FRP in the circumferential direction due to high hoop stress as result of the concrete expansion.

As shown in previous chapters, the tendency in the behavior of the CFFT systems is bilinear. Figure 8-1 shows an example of experimental load-strain curve for axial and lateral (hoop) directions. Even though both the concrete and the FRP core are loaded simultaneously, the first part of the curve coincides with the curve of the concrete without FRP due to low expansion of the concrete at this level, as show on Figure 4-37. Then from this state, the expansion of the concrete is quickly increased and tension in the hoop direction of the FRP is generated up to failure.

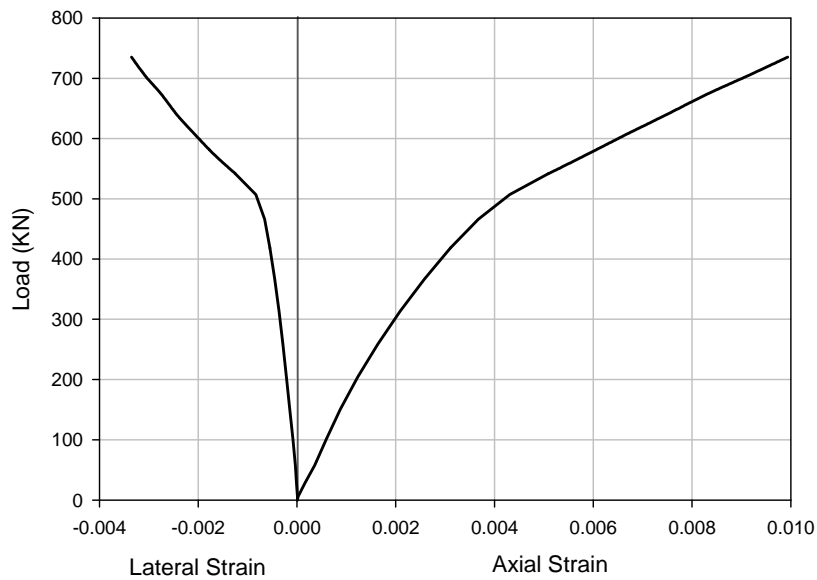


Figure 8-1: Typical Load-Strain Curves for Concrete-Filled FRP Tube.

Although several experimental studies on unreinforced concrete confined with FRP have been carried out, those aiming at obtaining reliable and accurate numerical models of its behavior are still in the development phase (Fam and Rizkalla, 2001b). In the literature there

are several models available to predict the behavior of short circular columns of concrete confined with FRP (Davila, 2008).

The models are primordially based on the confined concrete formulation suggested by Richart, et al. (1928) or by Newman and Newman (1972). The formulation is shown in Equations 8.1 and 8.2 respectively. Both formulations were developed for steel confined concrete as a function of the unconfined concrete strength f'_c :

$$f'_{cc} = f'_c \left(1 + 4.1 \left(\frac{f_l}{f'_c} \right) \right) \quad [8.1]$$

$$f'_{cc} = f'_c \left(1 + 3.7 \left(\frac{f_l}{f'_c} \right)^{0.86} \right) \quad [8.2]$$

where f_l is the confinement pressure. Therefore, these models assume a constant confinement pressure along the concrete core. The strength values predicted by the above expressions are very similar when they are evaluated for confinement pressures under 25 MPa, as seen on Figure 8-2.

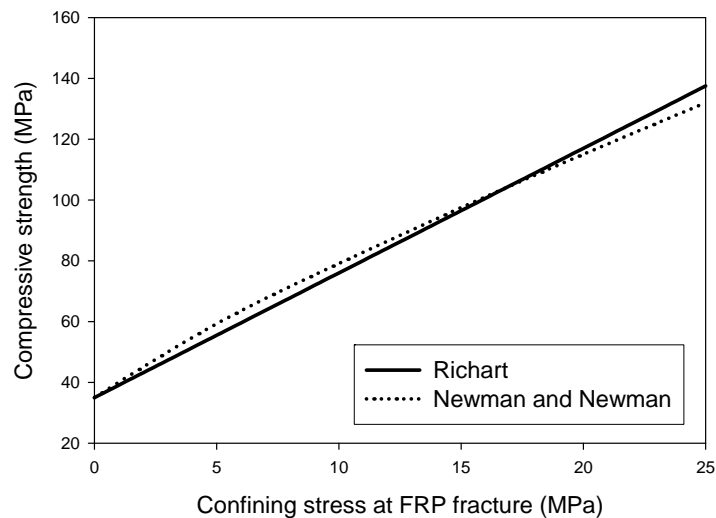


Figure 8-2: Compressive Strength of Confined Concrete.

The expressions can be used if it is assumed that fracture of the FRP and concrete crushing occurs essentially simultaneously. The implication of this is that failure is by fracture of the FRP in the circumferential direction only, because the strength of the circumferential fibers is unaffected by the presence of compression in the axial direction.

Recently, additional models have been developed as was reported in the revision included in the work by Davila (2008). Some of those models were developed from tests where the confining was provided only by the tubes, as in the studied performed by Fam and Rizkalla (2001); Mirmiran and Shahawy (1997); Saafi et al. (1999); and Samaan et al. (1998). In the work performed by Fam and Rizkalla (2001), the wall of the tube and the concrete core were axially loaded simultaneously applying the same axial strain. Differently, in the tests developed by Samaan, Mirmiran and Shahawy (1998) the FRP tubes were cut at the ends, thus loading only on the concrete core. Finally, in the work presented by Saafi et al. (1999) it is unclear if both the tube and the concrete core were loaded axially with the same axial deformation.

In general, the different models developed for the case when only the concrete core is loaded axially provide acceptable predictions of strength with simple expressions. If the FRP shell is axially loaded with the concrete core, it behaves as a biaxially-loaded membrane under axial compression and hoop tensile stresses. The presence of axial compression in this case weakens the shell in the hoop direction.

Studies from Fam and Rizkalla (2001), Mirmiran and Shahawy (1997), and Spoelstra and Monti (1999) adopted the confinement model developed by Mander et al. (1988a), but the lateral strain was determined by different means. Although, these three different models were studied, the methodology proposed by Fam and Rizkalla (2001a) was selected for its easy

applicability and good predictions. This methodology was studied and modified using the experimental data and the predicted results obtained from the FE models.

8.2 Fam and Rizkalla (2001a) modified model

The stress-strain model developed by Fam and Rizkalla (2001a) is based on the model developed by Mander, et al. (1988b), and it is based an equation suggested by Popovics (1973). Popovics assumes that for a slow (quasi-static) strain rate and monotonic loading, the longitudinal compressive concrete stress f_{cc} is given by:

$$f_{cc} = \frac{f'_{cc} x \cdot r}{r - 1 + x^r} \quad [8.3]$$

where:

$$x = \frac{\varepsilon_{cc}}{\varepsilon'_{cc}} \quad [8.4]$$

for any given strain, ε_{cc} , can be related to the ultimate confined strength, f'_{cc} :

$$\varepsilon'_{cc} = \varepsilon'_c \left[1 + 5 \left(\frac{f'_{cc}}{f'_c} - 1 \right) \right] \quad [8.5]$$

$$r = \frac{E_c}{E_c - E_{sec}} \quad [8.6]$$

$$E_{sec} = \frac{f'_{cc}}{\varepsilon'_{cc}} \quad [8.7]$$

ε'_{cc} is the ultimate axial strain of confined concrete. The confined peak strength f'_{cc} is expressed by Mander, et al. (1988a) in terms of the confining pressure σ_R :

$$\frac{f'_{cc}}{f'_{co}} = 2.54 \sqrt{1 + 7.94 \frac{\sigma_R}{f'_{co}} - 2 \frac{\sigma_R}{f'_{co}}} - 1.254 \quad [8.8]$$

For the case when both the concrete core and FRP shell are axially loaded with the same strain level (ϵ_{cc}), Fam and Rizkalla (2001a) suggest the following expression to evaluate the radial confinement pressure σ_R :

$$\sigma_r = \frac{\nu_c - \nu_{FRP}}{\frac{R}{E_s t} + \frac{1 - \nu_c}{E_c}} \epsilon_{cc} \quad [8.9]$$

where E_s is the elastic modulus of the shell in the hoop direction, R is the radius of the shell, and t is the wall thickness. Additionally, in order to obtain the variable Poisson's ratio ν_{co} , the following expression is proposed:

$$\frac{\nu_c}{\nu_{co}} = C \frac{\epsilon_{cc}}{\epsilon'_{cc}} + 1 \quad [8.10]$$

where ϵ'_{cc} is the strain at the peak strength, and C can be obtained using the following expression:

$$C = 1.914 \frac{\sigma_r}{f'_c} + 0.719 \quad [8.11]$$

The results from Gardner and Jacobson (1967) are used by Fam and Rizkalla (2001a) in order to correlate the constant C with three different confinement ratios (σ_r/f'_c) using a simple linear relationship (equation 8.11). The data reported by Gardner and Jacobson (1967) were selected by Fam and Rizkalla (2001a) mainly due to the fact that the range of the hydrostatic pressures used by Gardner and Jacobson (1967) in the experimental program are very similar to that experienced by concrete confined by FRP tubes.

Flores (2009) compared his experimental data and the experimental data reported by Gardner and Jacobson (1967) with the expression proposed by Fam (2000). This comparison showed that the expression proposed by Fam (2000) is accurate for low confinement ratios. Flores (2009) determined that Fam's expression fails to capture the change in the value of constant "C" when the confinement ratio increases.

The Poisson's ratios obtained using the equation 8.10 are very close to the ratios obtained from the 3D FE model developed in the present work for unaged systems. Basically the difference is because Fam and Rizkalla (2001a) use a linear relationship and only use the linear part of the graphics of axial stress vs. instantaneous Poisson's ratios obtained by Gardner and Jacobson (1967).

The lateral strain is evaluated using the follow expression:

$$\varepsilon_l = \frac{(\sigma_{FRP})_i}{E_{FRP}} + \nu_{FRP}(\varepsilon_{cc})_i \quad [8.12]$$

where:

$$\sigma_{FRP} = \frac{\sigma_R D}{2t} \quad [8.13]$$

and D and t are the diameter and thickness of the tube respectively.

In the initial development of FRP confined concrete models, the stress-strain model of Mander, et al. (1988a) for steel-confined concrete was directly used to analyze FRP-confined concrete columns. However, subsequent studies showed that this direct use is inappropriate. This is because in the model developed by Mander, et al. (1988a), a constant confining pressure is assumed, which is the case for steel-confined concrete when the steel is in plastic flow, but is not the case for FRP-confined concrete.

A modification of the model developed by Fam and Rizkalla (2001a) is proposed. Although the value of the constant C can be improved, only the equation 8.8 proposed by Mander, et al. (1988a) for confined concrete with spiral or circular steel hoops is updated. In order to include the effect of continue confining pressure and the confining effectiveness, the following expression is proposed:

$$\frac{f'_{cc}}{f'_{co}} = 2.54 \sqrt{1 + 7.94 \frac{\sigma_R}{f'_{co}}} - \mu \frac{\sigma_R}{f'_{co}} - 1.254 \quad [8.14]$$

where μ is a variable that depends of the confinement effectiveness.

For our case a value of 6 for unaged concrete and 4 for 500 days aged concrete was used for μ , as seen in Figure 8-3 and Figure 8-4. This value multiplies the relation between the confinement pressure σ_R and the unconfined peak strength f'_{co} . The effectiveness of the confinement was studied by Richart, et al. (1928) and by Newman and Newman (1972) (see expressions 8-1 and 8-2). They suggested values for confinement effectiveness of 4.1 and 3.7, respectively. Values of $\mu = 2$ can be used for higher strength concrete (about 30 MPa) when pressure confined is provided by FRP tubes as was reported by Fam and Rizkalla (2001b). Moran and Pantelides (2002) reported different values of confinement effectiveness when the confinement is provided by FRP jackets or FRP tubes. In order to avoid overestimated results, the response of these systems should be evaluated using values for μ from 2 to 6. Conservative results are obtained if a value of $\mu = 6$ is used.

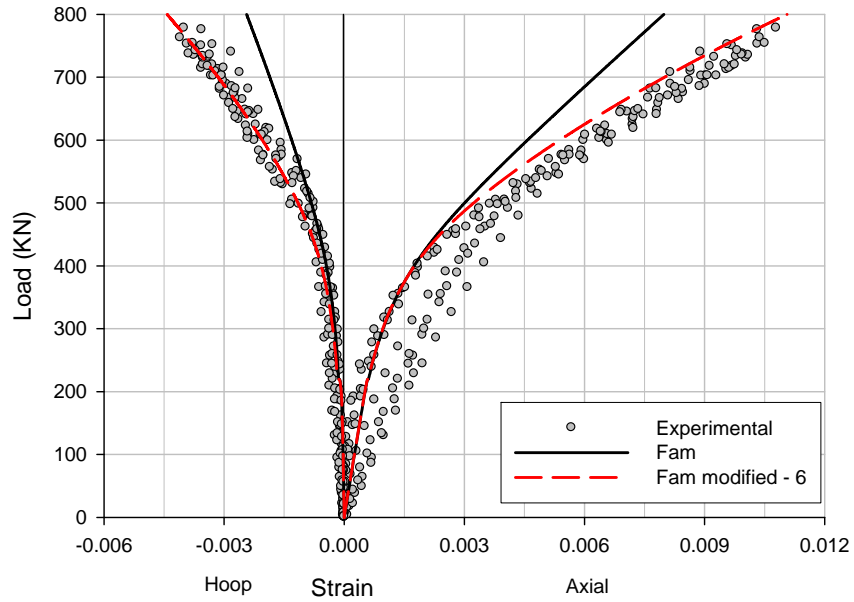


Figure 8-3: Experimental unaged data and proposed model.

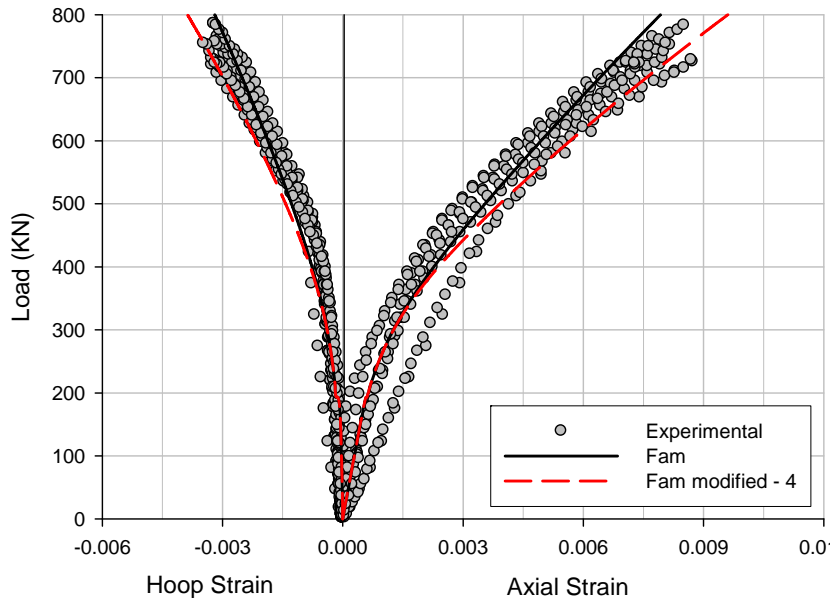


Figure 8-4: Experimental 500 days aged data and proposed model.

CHAPTER 9

CONCLUSIONS

9.1 Main Conclusions

This research developed a multi-year experimental program to characterize the nature of the strength degradation in cylindrical E-glass/epoxy composites as a function of time and hygrothermal state for moderate temperatures in order to predict the long-term behavior of CFFT under compression load.

The accelerated aging by means of hygrothermal process was conducted on FRP material to predict the long-term behavior of CFFT. Additionally the concrete cylinders were submerged in water at 30°C. The submerged concrete after prolonged curing in air had lower compression strength when compared with the baseline results which were cured on air only. Both concretes reached strength over f'_c .

Average moisture uptake measurements for the FRP over 200 days were performed on FRP material. Over this period, saturation was not reached. The Fickian diffusion model was used to predict the moisture absorption of composite material. The results showed an increase

in the saturation moisture due to an increase in the water temperature. The predicted saturation moisture of composite material was below 1% for the three studied temperatures.

Similarly to other studies, the following conclusions were reached based on compression tests of CFFT:

- The capacity of CFFT exceeds the sum of capacities of the concrete and the tube individually. The tube confines the concrete and increases its strength and ductility, while the concrete supports the tube, preventing local buckling failure.
- Stress-strain response of concrete confined using FRP shells is almost bi-linear. Up to the unconfined peak strength, near this state, the behavior is similar to that of unconfined concrete. Beyond this stage, a strain hardening behavior is observed.
- The ultimate capacity of CFFT is governed by the strength of the tube. Once the shell is fractured, the column fails. The first failure occurs at the end of the tube due to a stress concentration on this zone. After this state, the concrete expands excessively reaching the hoop capacity of the shell.
- The predicted confined strength of concrete in CFFT systems can be highly overestimated if the axial compressive stress developed in the tube is ignored.
- The crushing strength of the CFFT systems was not degraded after 500 days of hygrothermal exposure.
- A reduction in the ultimate strength of approximately 20 % was observed in the composite material and in the CFFT systems after 500 days of hygrothermal exposure at 30°C.

- Experimentally, the initiation of the confinement mechanism can be detected from the bi-linear axial-lateral strain behavior of the shell. A change of slope in the stress-strain curve occurs when concrete expands, producing more lateral strains in the shell.

The strength degradation was modeled using an Arrhenius relationship, as this has been found to be useful by others investigating hygrothermal strength degradation of glass fiber reinforced polymer composites (FRP) (Bank and Gentry, 1995, Chin, et al., 1997, Bank, et al., 1998, Buck, et al., 1998, Liao, et al., 1998, Ferrier and Hamelin, 2002). Arrhenius fit proved to be effective in modeling both the axial compression and hoop tension data over extended periods. This study showed an axial compression strength reduction in the FRP of 18% after 500 days of aging in water at 30°C and it predicts a reduction of 22 % at 1000 days. Similarly, it showed a hoop tension strength reduction of 17 % after 500 days of aging in water at 30°C and it predicts a reduction of 19 % at 1000 days.

The micromechanical model proposed by Barbero and Damiani (2003) provides a reasonable interpretation of the available data while using nominal values, taken from literature. This methodology showed good agreement when the analytical results were compared with the experimental data. This methodology predicts a compressive strength loss of 25 % percent for the FRP after 1000 days of aging in water at 30°C.

A 2D FEM was developed as an initial approach to study the behavior of CFFT system. In this case, the non-linearity of the contact between the concrete core and the FRP shell was considered. Good agreements between finite element model and experimental data were obtained. The FRP was modeled as an equivalent orthotropic layer in two orthogonal

principal directions with linear elastic behavior. The stress-strain curves obtained for the confined concrete using different dilatation angles were practically the same.

A 3D FE model was also performed. In this case, the FRP shell was modeled as laminate allowing the introduction of each lamina mechanical properties. The model developed to study the behavior of the FRP tube under compression load predicted the experimentally observed high stress concentration at the ends of the tube. This FE model also was used to predict the buckling load of the tube.

The good agreement between 3D FE model of CFFT and the experimental results were obtained thanks to the use of contact elements between the concrete core and the FRP shell. The use of high Poisson's ratios or lower modulus for the concrete was not necessary in order to adjust the results. The number of iterations needed in order to find the correct dilatation angle (δ) were very low. The values of the angles obtained in this study are typical for the concrete used.

In order to include the effect of a continued confining pressure and the confining effectiveness, this work proposes a modification of the model developed by Fam updating the expression proposed by Mander, et al. (1988b) for confined concrete. For our case, the a value of 6 for unaged concrete and 4 for 500 days aged concrete was used for μ . Values of $\mu = 2$ can be used for higher strength concrete (about 30 MPa) when pressure confined is provided by FRP tubes as was reported by Fam and Rizkalla (2001b). In order to avoid overestimated results, the response of these systems should be evaluated using values for μ from 2 to 6. Conservative results are obtained if a value of $\mu = 6$ is used.

9.2 Original Contributions of this Dissertation

The main original contributions are:

1. Multi-year experimental program to characterize the nature of the strength degradation in cylindrical E-glass/epoxy.
2. The understanding of structural behavior of FRP tubes used for composite piles under hygrothermal conditions.
3. The understanding of structural behavior of concrete filled FRP tubes under hygrothermal conditions.
4. The implementation of degradation models for the reinforcement fibers and the interphase region through the modification of Rosen's model for concrete filled FRP tubes.
5. The implementation of contact surface elements between concrete core and FRP tubes using a general purpose finite element code.
6. The understanding of the confinement effectiveness in concrete filled FRP tubes.
7. The implementation of the confinement effectiveness in the expression developed by Mander, et al., (1988b).

9.3 Recommendations for Future Work

More work in related areas actually is being studied or needs to be conducted. Areas that need additional studies to complete the development of CFFT (concrete filled FRP tubes) as a product ready to be used by the industry and expand the understanding of the behavior are:

- Examine the behavior under combined axial load and bending moment and establish interaction diagrams for sections. The 3D FE model developed can be useful for this study.
- Examine the slenderness effect for long columns. The 3D model can be modified for this goal.
- Investigate the shear behavior of CFFT.
- Improve stress-strain models for FRP-confined concretes under axial cyclic compression.
- Establish practical, standard, and reliable methods of material testing of FRP tubes and its constitutive materials in order to obtain their effective mechanical properties.

REFERENCES

ABAQUS (2006). *User's Manual*, Vol. II. Version 6.6.

Abdel-Magid, B., Ziaee, S., Gass, K., and Schneider, M. (2005). "The combined effects of load, moisture and temperature on the properties of E-glass/epoxy composites." *Composite Structures*, 71(3-4), 320-326.

ACI (1996). "State of the art report of fiber reinforced plastic reinforcement for concrete structures." American Concrete Institute, Detroit.

Adams, P. B. (1984). "Glass corrosion A record of the past? A predictor of the future?" *Journal of Non-Crystalline Solids*, 67(1-3), 193-205.

Aindow, A. J., Oakley, D. R., and Proctor, B. A. (1984). "Comparison of the weathering behaviour of GRC with predictions made from accelerated ageing tests." *Cement and Concrete Research*, 14(2), 271-274.

ASTM (1995). *Standard Test Method for Compressive Properties of Polymer Matrix Composite Materials with Unsupported Gage Section by Shear Loading*, ASTM International, D3410.

ASTM (2000a). *Standard Test Method for Apparent Hoop Tensile Strength of Plastic or Reinforced Plastic Pipe by Split Disk Method*, ASTM International, D2290.

ASTM (2000b). *Standard Test Method for Tensile Properties of Polymer Matrix Composite Materials*, ASTM International, D3039.

ASTM (2006). *Standard Test Method for Short-Beam Strength of Polymer Matrix Composite Materials and Their Laminates*, ASTM International, ASTM D2344.

ASTM (2007). *Standard Practice for Making and Curing Concrete Test Specimens in the Laboratory*, ASTM International, ASTM C192.

Bakis, C. E., Bank, L. C., Brown, V. L., Cosenza, E., Davalos, J. F., Lesko, J. J., Machida, A., Rizkalla, S. H., and Triantafillou, T. C. (2002). "Fiber-Reinforced Polymer Composites for Construction---State-of-the-Art Review." *Journal of Composites for Construction*, 6(2), 73-87.

Balmer, G. G. (1949). "Shearing strength of concrete under high triaxial stress-computation of Mohr's envelope as curve." US Bureau of Reclamation, Denver, Co.

Bank, L. C., and Gentry, T. R. (1995). "Accelerated Test Methods to Determine the long-Term Behavior of FRP Composite Structures: Enviromental Effects." *Journal of Reinforced Plastics and Composites*, 14, 558-587.

Bank, L. C., Gentry, T. R., Barkatt, A., Prian, L., Wang, F., and Mangla, S. R. (1998). "Accelerated Aging of Pultruded Glass/Vinyl Ester Rods." *Proc., International Conference on Fibre Composites in Infrastructure ICCI'98*, 423-437.

Barbero, E. J., and Damiani, T. M. (2003). "Phenomenological Prediction of Tensile Strength of E-Glass Composites from Available Aging and Stress Corrosion Data." *Journal of Reinforced Plastics and Composites*, 22(4), 373-394.

Barton, J. M., and Greenfield, D. C. L. (1986). "The Use of Dynamic Mechanical Methods to Study the Effect of Absorbed Water on Temperature-Dependent Properties of an Epoxy Resin--Carbon Fibre Composite " *British Polymer Journal*, 18(1), 51-56.

Bellotti, R., and Rossi, P. (1991). "Cylinder tests: experimental technique and results." *Materials and Structures*, 24(1), 45-51.

Bodner, G. M. (2011). "Chemical Education Division Groups." *Activation energy*, <chemed.chem.purdue.edu/genchem/topicreview>. (November, 2011).

Bradshaw, R. D., and Brinson, L. C. (1997). "Physical aging in polymers and polymer composites: An analysis and method for time-aging time superposition." *Polymer Engineering & Science*, 37(1), 31-44.

Bruneau, M., and Marson, J. (2004). "Seismic Design of Concrete-Filled Circular Steel Bridge Piers." *Journal of Bridge Engineering*, 9(1), 24-34.

Buck, S. E., Lischer, D. W., and Nemat-Nasser, S. (1998). "The Durability of E-Glass/Vinyl Ester Composite Materials Subjected to Environmental Conditioning and Sustained Loading." *Journal of Composite Materials*, 32(9), 874-892.

Burgoyne, C. J. (1999). "Advanced composites in civil engineering in Europe." *International Journal for Numerical Methods in Engineering*, 9(4), 267-272.

Burr, W. H. (1912). "Composite columns of concrete and steel." *Proc., Proceedings of the Institution of Civil Engineers*, 114-126.

Caceres, A., Jamond, R. M., Hoffard, T. A., and Malvar, L. J. (2000). "Accelerated testing of Fiber Reinforced Polymer Matrix Composites-Test Plan." NFESC Special Publication SP-2091-SHR.

Cain, J., Post, N. L., Lesko, J. J., Case, S. W., Lin, Y. N., J.S., R., and P.E., H. (2006a). "Post-Curing Effects on Marine VARTM FRP Composite Material Properties for Test and Implementation." *J. Engineering Materials and Technology, ASME*, 34-40.

Cain, J., Santiago, k., Case, S. W., Lesko, J., Pando, M. A., and Acosta, F. J. (2006b). "The Effect of Hygrothermal Aging on Cylindrical E-glass/Epoxy Composites." *Proc., 23rd Southeastern Conference on Theoretical and Applied Mechanics*,

Charoenphan, S., Plesha, M. E., and Bank, L. C. (2004). "Simulation of crack growth in composite material shell structures." *International Journal for Numerical Methods in Engineering*, 60(14), 2399-2417.

Chateauminois, A., Vincent, L., Chabert, B., and Soulier, J. P. (1994). "Study of the interfacial degradation of a glass-epoxy composite during hygrothermal ageing using water diffusion measurements and dynamic mechanical thermal analysis." *Polymer*, 35(22), 4766.

Chen, W.-F., and Han, D. J. (1988). *Plasticity for structural engineers*, Springer-Verlag, New York.

Chin, J. W., Nguyen, T., and Aouadi, K. (1997). "Effects of Environmental Exposure on Fiber-Reinforced Plastic (FRP) Materials Used in Construction." *Journal of Composites Technology and Research*, 19(4), 205-213.

Costa, M. L., Almeida, S. F. M. d., and Rezende, M. C. (2005). "Hygrothermal effects on dynamic mechanical analysis and fracture behavior of polymeric composites." *Materials Research*, 8(3), 335-340.

Cusson, D., and Paultre, P. (1995). "Stress-Strain Model for Confined High-Strength Concrete." *Journal of Structural Engineering*, 121(3), 468-477.

d'Almeida, J. R. M. (1991). "Effects of distilled water and saline solution on the interlaminar shear strength of an aramid/epoxy composite." *Composites*, 22(6), 448-450.

Davila, J. F. (2008). "Comportamiento mecánico de tubos de material compuesto rellenos de hormigón bajo carga axial en compresión." Msc thesis, University of Puerto Rico, Mayaguez, PR.

Davila, J. F., Lammoglia, V. A., Acosta, F. J., and Pando, M. A. (2006). "Compressive Stress-Strain Behavior of Concrete with Variable Confinement." *Proc., 23rd Southeastern Conference in Theoretical and Applied Mechanics*,

Day, R. L. (1992). *The Effect of Secondary Ettringite Formation on the Durability of Concrete: A Literature Analysis* Portland Cement Association, Skokie, Illinois.

De Lorenzis, L., and Tepfers, R. (2003). "Comparative Study of Models on Confinement of Concrete Cylinders with Fiber-Reinforced Polymer Composites." *Journal of Composites for Construction*, 7(3), 219-237.

Di Tomaso, A., and Ghinelli, F. (1998). *New materials: FRP-confined concrete columns*, FIB, Treviso, Italy.

Eckold, G. (1994). *Design and manufacture of composite structures*, McGraw-Hill; Woodhead Publishing, New York; Cambridge.

Ellobody, E., and Young, B. (2006). "Nonlinear analysis of concrete-filled steel SHS and RHS columns." *Thin-Walled Structures*, 44(8), 919-930.

Ellobody, E., Young, B., and Lam, D. (2006). "Behaviour of normal and high strength concrete-filled compact steel tube circular stub columns." *Journal of Constructional Steel Research*, 62(7), 706-715.

Ellyin, F., and Maser, R. (2004). "Environmental effects on the mechanical properties of glass-fiber epoxy composite tubular specimens." *Composites Science and Technology*, 64(12), 1863-1874.

Emmons, P. H., Vaysburd, A. M., and Thomas, J. (1998). "Strengthening concrete structures, PartII, Advanced composites." *Concrete International*, 20(4), 56-60.

Faber, O. (1956). "Savings to be effected by the more rotational design of cased stanchions as a result of recent full size test." *Structural Engineering*.

Fam, A. (2000). "Concrete-Filled Fiber-Reinforced Polymer tubes for axial and Flexural Structural members." PhD, University of Manitoba, Canada.

Fam, A., and Rizkalla, S. H. (2001a). "Behavior of Axially Loaded Concrete-Filled circular Fiber-Reinforced Polymer Tubes." *ACI Structural Journal*, 98(3), 280-289.

Fam, A., and Rizkalla, S. H. (2001b). "Confinement model for axially loaded concrete confined by FRP tubes." *ACI Structural Journal*, 98(4), 251-461.

Fam, A., Schnerch, D., and Rizkalla, S. H. (2002). "Moisture content effect on durability of Concrete-Filled GFRP Tubular Piles." NCSU-CFL

Fardis, M. N., and Khalili, H. (1981). "Concrete Encased in Fiberglass-Reinforced Plastic." *ACI Journal*, 78(6), 440-446.

Faria, R., Oliver, J., and Cervera, M. (1998). "A strain-based plastic viscous-damage model for massive concrete structures." *International Journal of Solids and Structures*, 35(14), 1533-1558.

Ferrier, E., and Hamelin, P. (2002). "Effect of Water Absorption on the durability of Carbon FRP reinforcement." *Proc., CDCC'2002 - International Conference on Durability of FRP Composites for Construction*, 99-111.

Flores, O. G. (2009). "Triaxial compression experiemnts on plain concrete." Master of Engineering in Civil Engineering Degree of Master of Engineering, University of Puerto Rico, Mayaguez, PR.

France, P., Duncan, W., Smith, D., and Beales, K. (1983). "Strength and fatigue of multicomponent optical glass fibres." *Journal of Materials Science*, 18(3), 785.

Fukujama, H. (1999). "FRP composites in Japan." *Concrete International*, 21(10), 29-32.

Furlong, R. W. (1967). "Strength of steel-encased concrete beams." *Structural Engineering*, 93(5), 113-124.

Gardner, N. J., and Jacobson, E. R. (1967). "Structural behavior of concrete filled tubes." *ACI Journal*, 64(7), 404-412.

Gerbaudo, G., and Prato, C. A. (2004). "Análisis numérico no-lineal de tubos de acero rellenos de hormigón para grandes deformaciones." Magister en ciencias de la ingeniería, Universidad Nacional de Córdoba, Córdoba, Argentina.

Gibson, R. F. (1994). *Principles of composite material mechanics*, McGraw-Hill, Inc., New York.

Han, L.-H., Liu, W., and Yang, Y.-F. (2008). "Behavior of thin walled steel tube confined concrete stub columns subjected to axial local compression." *Thin-Walled Structures*, 46(2), 155-164.

Harmon, T., Slattery, K., and Ramakrishnan, S. (1995). "The effect of confinement stiffness on confined concrete nonmetallic (FRP) reinforcement for concrete structures." *Proc., Second International RILEM Symposium*, 584-592.

Harmon, T. G., Ramakrishnan, S., and Wang, E. H. (1998). "Confined concrete subjected to uniaxial monotonic loading." *Engineering Mechanics*, 124(12), 1303-1309.

Harper, J. F., and Naeem, M. (1989). "The moisture absorption of glass fibre reinforced vinylester and polyester composites." *Materials & Design*, 10(6), 297.

Harries, K. A., and Kharel, G. (2003). "Experimental investigation of the behavior of variably confined concrete." *Cement and Concrete Research*, 33(6), 873-880.

Hayes, M. D., Garcia, K., Verghese, N., and Lesko, J. (1998). "The Effects of Moisture on the Fatigue Behavior of a Glass/Vinyl Ester Composite." *Proc., International Conference on Fibre Composites in Infrastructure ICCI'98*, 1-13.

Hognestad, E. (1951). "A study of combined bending and axial load in reinforced concrete members " *Bulletin series No. 339*, University of Illinois, Urbana.

Hollaway, L. (1990). *Polymers and polymer composites in construction*, T. Telford, London.

Hollaway, L. C., and Head, P. R. (2001). *Advanced polymer composites and polymers in the civil infrastructure*, Elsevier Science, Ltd., New York.

Hollaway, L. (1993). *Polymer composites for civil and structural engineering*, Blackie Academic, London ; New York.

Imran, I. (1994). "Applications of non-associated plasticity in modelling the mechanical response of concrete." PhD, University of Toronto, Toronto, Canada.

Imran, I., and Pantazopoulou, S. J. (1996). "Experimental study of plain concrete under triaxial stress." *Aci Materials Journal*, 93(6), 589-601.

Jayaraman, K., Gao, Z., and Reifsnider, K. L. (1994). "The Interphase in Unidirectional Fiber-Reinforced Epoxies: Effect on Local Stress Fields." *Journal of Composites Technology and Research*, 16(1), 11.

Jones, F. R., and Risk, A. (1963). "An investigation on the behaviour of encased steel columns under load." *Structural Engineering*, 1.

Kajorncheappungam, S. (1999). "The Effects of Environmental Aging on the Durability of Glass/Epoxy Composites." Ph.D, West Virginia University, Morgantown.

Karbhari, V. M., and Eckel, D. A. (1993). "Strengthening of concrete column stubs through resin infused composite wraps." *Journal of Thermoplastic Composite Materials*, 6(2), 92-107.

Karbhari, V. M., and Gao, Y. (1997). "Composite Jacketed Concrete Under Uniaxial Compression – Verification of Simple Design Equations." *Materials in Civil Engineering*, 9(4), 185-192.

Karbhari, V. M., and Seible, F. (1999). "Fiber-reinforced polymer composites for civil infrastructure in the USA." *Fiber-reinforced polymer composites for civil infrastructure in the USA*, 9(4), 274-281.

Karbhari, V. M., and Seible, F. (2000). "Fiber Reinforced Composites – Advanced Materials for the Renewal of Civil Infrastructure." *Applied Composite Materials*, 7, 95-124.

Kasei, m. (1993). *Carbon fiber reinforced earthquake-resistant retrofitting*, Mitsubishi Kasei Corporation, Tokio, Japan.

Katsumata, H., and Kimura, K. (1990). "Applications of retrofit method with carbon fiber for existing reinforced concrete structures." *Proc., 22nd. Joint UNJR Panel Meeting*, Gaithersburg, Md., 1-28.

Katsumata, H., Kobatale, Y., and Takeda, T. (1987). "A study on the strengthening with carbon fiber for earthquake-resistance capacity of existing reinforced previous termconcretenext term columns. ." *Proc., Seminar on Repair and Retrofit of Structures, US-Japan Panel on Wired and Seismic Effects*, UJNR

Tsukuba, Japan, 18.11–18.23.

Kelly, K. W., and Barbero, E. (1998). "The Effect of Fiber Damage on the Longitudinal Creep of a CFMMC."

Khennane, A., and Melchers, R. E. (2003). "Durability of Glass Polymer composites Subject to Stress corrosion." *Journal of Composites for Construction*, 7(2), 109.

Kotsovos, M. D., and Newman, J. B. (1978). "Generalized stress-strain relations for concrete." *Journal of Engineering Mechanics*, 104(4), 845-856.

Kupfer, H., Hilsdorf, H. K., and Rusch, H. (1969). "Behavior of concrete under biaxial stresses." *ACI Journal*, 66(8), 656-666.

Lampo, R., Nosker, T., Barno, D., Busel, J., Maher, A., Dutta, P., and Odello, R. (1998). "Development and Demonstration of FRP Composite Fender, Loadbearing and Sheet Piling Systems." USACERL.

Lange, D. A. (1994). "Long-Term Strength Development of Pavement Concretes." *Journal of Materials in Civil Engineering*, 6(1), 78-87.

Larralde, J. (1997). "Compressive Strength of Small Concrete Specimens Confined with Fiberglass Laminates." *Cement and Concrete*.

Lemasçon, A., Castaing, P., and Mallard, H. (1996). "Failure investigation of polymer and composite material structures in the mechanical engineering industry." *Materials Characterization*, 36(4-5), 309-319.

Li, Q., and Ansari, F. (1999). "Mechanics of damage and constitutive relationships for high-strength concrete in triaxial compression." *Journal of Engineering Mechanics*, 125(1), 1-10.

Liao, K., Schultheisz, C. R., and Hunston, D. L. (1998). "Long-term Durability of Fiber-Reinforced Polymer-Matrix Composite Materials for Infrastructure Applications: A Review " *Journal of Advanced Materials*(4).

Litherland, K. L., Oakley, D. R., and Proctor, B. A. (1981). "The use of accelerated ageing procedures to predict the long term strength of GRC composites." *Cement and Concrete Research*, 11(3), 455-466.

Lopez-Anido, R. A., Naik, T. R., Fry, G. T., Lange, D. A., and Karbhari, V. M. (2000). *Emerging materials for civil infrastructure : state of the art*, American Society of Civil Engineers, Reston, Va.

Lopez, J. J. (2002). "Material Identification Procedure for Elastoplastic Drucker--Prager Model." *Journal of Engineering Mechanics*, 128(5), 586-591.

Lu, G., and Yu, T. (2003). "Energy Absorption of Structures and Materials." Woodhead Publishing.

Mander, J., Priestly, M., and Park, R. (1988a). "Observed stress-strain behavior of confined concrete." *Journal of Structural Engineering*, 114(8), 1827-1849.

Mander, J. B., Priestley, M. J. N., and Park, R. (1988b). "Theoretical stress-strain model for confined concrete." *Journal of Structural Engineering*, 114(8), 1804-1826.

Marson, J., and Bruneau, M. (2000). "Cyclic testing of concrete-filled circular steel bridge piers having ebcased fixed-based detail." *Ottawa Carleton Earthquake Eng. Re. Center*, University of Ottawa, Ottawa.

Matsuda, T., Sato, H., Fujiwara, H., and Higashira, N. (1990). "Effect of carbon fiber reinforcement as a strengthening measure for reinforced concrete bridge piers." *Proc., 1st. U. S. Japan Workshop on Seismic Retrofit of Bridges*, Tsukuba, Japan,

McKague, E. L., Reynolds, J. D., and Halkias, J. E. (1978). "Swelling and glass transition relations for epoxy matrix material in humid environments." *Journal of Applied Polymer Science*, 22(6), 1643-1654.

Metcalfe, A. G., and Schmitz, G. K. (1972). "Mechanism of stress corrosion in E glass filaments." *Glass Technology*, 13(1), 5-16.

Mijovic, J. (1985). "Interplay of physical Chemical Aging in Graphite/Epoxy composites." *Journal of Composite Materials*, 19, 178-191.

Mijovic, J., and Lin, K.-F. (1985). "The effect of hygrothermal fatigue on physical/mechanical properties and morphology of neat epoxy resin and graphite/epoxy composite." *Journal of Applied Polymer Science*, 30(6), 2527-2549.

Mirmiran, A., and Shahawy, M. (1997). "Behavior of Concrete Columns Confined by Fiber Composites." *Journal of Structural Engineering*, 123(5), 583-590.

Mirmiran, A., Zagers, K., and Yuan, W. (2000). "Nonlinear finite element modeling of concrete confined by fiber composites." *Finite Elements in Analysis and Design*, 35(1), 79-96.

Miyauchi, K., Nishibayashi, S., and Inoue, S. (1997). "Estimation of strengthening effects with carbon fiber sheet for concrete columns." *Proc., Proceedings, 3rd International Symposium, Non-Metallic (FRP) Reinforcement for concrete structures*, 217-224.

Moran, D. A., and Pantelides, C. P. (2005). "Damage-Based Stress-Strain Model for Fiber-Reinforced Polymer-Confined Concrete." *Structural Journal*, 102(1), 54-61.

Nanni, A. (1995). "Concrete repair with externally bonded FRP reinforcement: examples in Japan." *Concrete International*, 17(6), 22-26.

Nanni, A. (1997). "CFRP strengthening: new technology becomes mainstream." *Concrete International*, 19(6), 19-23.

Nanni, A., and Gold, W. (1998). "Strength assesment of external FRP reinforcement, in situ load testing." *Concrete International*, 20(6), 39-42.

Nanni, A., Norris, M. S., and Bradford, N. M. (1994). "Lateral confinement of concrete using FRP reinforcement." *Proc., ACI SP-138 American Concrete Institute, Fiber Reinforcement Plastic for Concrete Structures*, Farmington Hills, Mich, 193-209.

Neale, K. W., and Laboussi re, P. (1998). "Fiber composite sheets in cold climate rehab." *Concrete International*, 20(6), 22-24.

Neville, A. M. (1995). *Properties of concrete*, Longman Group, Harlow.

Newman, K., and Newman, J. B. (1972). "Failure theories and design criteria for plain concrete." *Proc., International Engineering Materials Conference on structure, solid Mechanics and Engineering Design, (Southampton, 1969)*, Wiley Interscience, 963-995.

Nystrom, H. E., Watkins, S. E., Nanni, A., and Murray, S. (2003). "Financial Viability of Fiber-Reinforced Polymer (FRP) Bridges." *Journal of Management in Engineering*, 19(1), 2-8.

O'Shea, M., and Bridge, R. (2000). "Design of circular thin-walled concrete filled steel tubes." *Structural Engineering*, 126(11), 1295-1303.

Otto, W. H. (1965). "The Effects of Moisture on the Strength of Glass Fibers – A Literature Review." *Whittaker Corp., NARMCO R & D Div., U.S. Naval Research Lab, Contract No. 4522 (00) (X)*, San Diego, CA.

Pando, M. A., Lesko, J., Fam, A., and Rizkalla, S. (2002). "Durability of Concrete-Filled Tubular FRP Piles." *Proc., Third International Conference on Composites in Infrastructure*, San Francisco, CA,

Pantazopoulou, S. J. (1995). "Role of Expansion on Mechanical Behavior of Concrete." *Journal of Structural Engineering*, 121(12), 1795-1805.

Pantazopoulou, S. J., and Mills, R. H. (1995). "Microstructural aspects of the mechanical response of plain concrete." *ACI Materials Journal*, 92(6), 605-616.

Pantuso, A., Spadea, G., and Swamy, R. (1998). "An Experimental study on the Durability of GFRP Bars." *Proc., International Conference on Fibre Composites in Infrastructure ICCI'98*, Tucson, AZ, 476-487.

Patsch, A., Gerbaudo, C. F., and Prato, C. A. (2002). "Analysis and Testing of Piles for Ship Impact Defenses." *Journal of Bridge Engineering*, 7(4), 236-244.

PCA (2001). *Ettringite Formation and the Performance of Concrete*, Portland Cement Association.

Phani, K. K. (1988). "Strength distribution and gauge length extrapolations in glass fibre." *Journal of Materials Science*, 23(4), 1189-1194.

Picher, F., Rochete, P., and Labossière, P. (1996). "Confinement of concrete cylinders with CFRP." *Proc., First International Conference on composites in Infrastructure*, 829-841.

Popovics, S. (1973). "A numerical approach to the complete stress strain curve for concrete." *Cement and Concrete Research*, 3(5), 583-599.

Porter, M. L., and Barnes, B. A. (1998). "Accelerated Aging Degradation of Glass Fiber Composites." *Proc., International Conference on Fibre Composites in Infrastructure ICCI'98*, 446-459.

Priestley, M. J., Seible, F., and Fyfe, E. (1992). "Column seismic retrofit using fibreglass/epoxy jackets " *Proc., First International Conference on Advanced Composite Material in Bridges and Structures*, Quebec, Canada, 287-298.

Priestley, M. J. N., and Seible, F. (1991). *Seismic assessment and retrofit of bridges*, University of California at San Diego, California,.

Pritchard, G., and Speake, S. D. (1987). "The use of water absorption kinetic data to predict laminate property changes." *Composites*, 18(3), 227.

Rao, R. M. V. G. K., Swaminadham, M., and Rajanna, K. (1981). "Effect of moisture and glass contents on the poisson's ration of FRP plates as determined by laser interferometry." *Fibre Science and Technology*, 15(3), 235.

Ray, B. C. (2005). "Hydrothermal Fatigue on Interface of Glass-epoxy Laminates." *Journal of Reinforced Plastics and Composites*, 24(10), 1051-1056.

Razvi, S. R., and Saatcioglu, M. (1999). "Confinement model for high strength concrete." *Structural Engineering*, 125(3), 281-289.

Richart, F. E., Brandtzaeg, A., and Brown, R. L. (1928). "A Study of the Failure of Concrete Under Combined Compressive Stresses." University of Illinois Engineering Experimental Station, Champaign, IL.

Rizkalla, S., and Labossière, P. (1999). "Structural engineering with FRP-in Canada." *Concrete International*, 2(10), 25-28.

Rosen, B. W. (1964). "Tensile failure of fibrous composites." *American Institute of Aeronautics and astronautics*, 2(11), 1985-1991.

Roy, R., Sarkar, B. K., and Bose, N. R. (2001). "Effects of moisture on the mechanical properties of glass fibre reinforced vinylester resin composites " *Bulletin of Materials Science*, 24(1), 87.

Ruiz, M., Pando, M. A., and Acosta, F. J. (2004). "Non-linear Finite Element Analysis of Concrete-Filled FRP Composite Piles." *Proc., Developments in Theoretical and Applied Mechanics*, jjj, 352-361.

Saadatmanesh, H., Ehsani, M. R., and Li, M. W. (1994). "Strength and ductility of concrete columns externally reinforced with fiber composite straps." *ACI Structural Journal*, 91(4), 434-477.

Saafi, M., Toutanji, H. A., and Li, Z. (1999). "Behavior of concrete columns confined with fiber reinforced polimer tubes." *Aci Materials Journal*, 96(3), 397-404.

Saatcioglu, M., and Razvi, S. R. (1992). "Strength and ductility of confined concrete." *Journal of Structural Engineering*, 118(6), 1590-1607.

Saenz, N., and Pantelides, C. P. (2007). "Strain-Based Confinement Model for FRP-Confined Concrete." *Journal of Structural Engineering*, 133(6), 825-833.

Samaan, M. (1997). "Concrete filled FRP tubes." PhD, University of Central Florida, FL.

Samaan, M., Mirmiran, A., and Shahawy, M. (1998). "Model of Concrete Confined by Fiber Composites." *Journal of Structural Engineering*, 124(9), 1025-1031.

Schutte, C. L. (1994). "Environmental durability of glass-fiber composites." *Materials Science and Engineering: R: Reports*, 13(7), 265.

Schutte, C. L., McDonough, W., Shioya, M., McAuliffe, M., and Greenwood, M. (1994). "The use of a single-fibre fragmentation test to study environmental durability of interfaces/interphases between DGEBA/mPDA epoxy and glass fibre: the effect of moisture." *Composites*, 25(7), 617.

Seible, F., and Karbhari, V. M. (1996). "Advanced composites for civil engineering applications in the United States." *Proc., 1st. International Conference on Composites in Infrastructure*, 21-37.

Seible, F., and Priestley, M. J. N. (1993). "Retrofit of rectangular flexural columns with composite fiber jackets." *Proc., 2nd. Annual Seismic Res. Workshop*, Sacramento, California,

Sfer, D., Carol, I., Gettu, R., and Etse, G. (2002). "Study of the Behavior of Concrete under Triaxial Compression." *Journal of Engineering Mechanics*, 128(2), 156-163.

Sheard, P., Clarke, J., Dill, M., Hammersley, G., and Richardson, D., (1997). "Eurocrete-Taking Account of Durability for Design of FRP Reinforced Concrete Structures." *Proc., Third International Symposium on Non-Metallic (FRP) Reinforcement for Concrete Structures*, Japan, 75-82.

Shehata, E., Rizkalla, S., and Stewart, D. (1998). "Roof retrofit." *Concrete International*, 20(6), 44-46.

Shen, C.-H., and Springer, G., S. (1976). "Moisture Absorption and Desorption of Composite Materials." *Composite Materials*, 10(1), 2-20.

Sih, G. C., and DiTommaso, A. (1985). *Fracture mechanics of concrete: structural application and numerical calculation*, M. Nijhoff ; Distributor for the U.S. and Canada, Kluwer Academic Publishers, Dordrecht ; Boston Hingham, MA, USA.

Smith, S. S., William, K. J., Gerstle, K. H., and Sture, S. (1989). "Concrete over the top, or: Is there life after peak?" *ACI Materials Journal* 86(5), 491-497.

Spoelstra, M. R., and Monti, G. (1999). "FRP-Confined Concrete Model." *Journal of Composites for Construction*, 3(3), 143-150.

Steckel, G. L., Hawkins, G. F., and Bauer, J. L. (1998). "Environmental Durability Of Composites for Seismic Retrofit of Bridges Columns." *Proc., Nist workshop on standards*

Development for the Use of Fiber Reinforced Polymers for the Rehabilitation of concrete and Masonry Structures, 83-96.

Stevens, R. F. (1959). "Encased steel stanchions and BS449." *Engineering*, October.

Subramanian, S., Reifsnider, K. L., and Stinchcomb, W. W. (1995). "Tensile Strength of Unidirectional Composites: The Role of Efficiency and Strength of Fiber-Matrix Interface " *Journal of Composites Technology and Research*, 17(4), 12.

Susantha, K. A. S., Ge, H., and Usami, T. (2001). "Uniaxial stress-strain relationship of concrete confined by various shaped steel tubes." *Engineering Structures*, 23(10), 1331-1347.

Taerwe, L. R., and Matthys, S. (1999). "FRP for concrete construction: Activities in Europe." *Concrete International*, 21(10), 33-36.

Teng, J. G., and Lam, L. (2004). "Behavior and Modeling of Fiber Reinforced Polymer-Confined Concrete." *Journal of Structural Engineering*, 130(11), 1713-1723.

Teng, J. G., Yu, T., Wong, Y. L., and Dong, S. L. (2007). "Hybrid FRP-concrete-steel tubular columns: Concept and behavior." *Construction and Building Materials*, 21(4), 846-854.

Theocaris, P. S., Papanicolaou, G. C., and Kontou, E. A. (1983). "Interrelation between moisture absorption, mechanical behavior, and extent of the boundary interphase in particulate composites." *Journal of Applied Polymer Science*, 28(10), 3145-3153.

Thomas, W. F. (1960). "The Strength and Properties of Glass Fibers." *Physics and Chemistry of Glasses*, 1(1), 4-18.

Toutanji, H. A. (1999). "Durability characteristics of concrete columns confined with advanced composite materials." *Composite Structures*, 44(2-3), 155-161.

Tuakta, C. (2005). "Use of fiber reinforced polymer composite in bridge structures." Thesis M. Eng. , Massachusetts Institute of Technology.

Tuttle, M. E. (1996). "Framework for long-term durability predictions of polymeric composites." *Proc., DURACOSYS 95 International Conference*, 169-176.

van Mier, J. G. M. (1986). "Fracture of concrete under complex stress." *Heron*, 31(3), 1-90.

Wang, C.-z., Guo, Z.-h., and Zhang, X.-q. (1987). "Experimental investigation of biaxial and triaxial compressive concrete strength." *ACI Materials Journal* 84(2), 92-100.

Whitney, J. M. (1991). "Failure Modes in Compression Testing of composite Materials." *Proc., How Concept Becomes Reality - proceedings of 36th International SAMPE Symposium*, Society for Advancement of Material and Process Engineering, Covina, CA, 1069-1078.

Wolff, G. E. (1993). "Moisture Effects on Polymer Matrix Composite." *SAMPE Journal*, 29(3), 11-19.

Wood, S. L. (1992). "Evaluation of the Long-Term Properties of Concrete,," Portland Cement Association, Skokie, Illinois.

Xiao, Y., and Ma, R. (1997). "Seismic retrofit of RC circular columns using prefabricated composite jacketing." *Journal of Structural Engineering*, 123(10), 1357-1364.

Xiao, Y., Martin, G. R., Yin, Z., and Ma, R. (1996). "Seismic retrofit of existing reinforced concrete bridge columns using a prefabricated composite jacketing system." *Proc., 1st. Conference on Composites in Infrastructure*, 903-916.

Xiao, Y., and Wu, H. (2000). "Compressive behavior of concrete confined by carbon fiber composites jackets." *Materials in Civil Engineering*, 12(2), 139-146.

Appendix A

CONCRETE CURVES

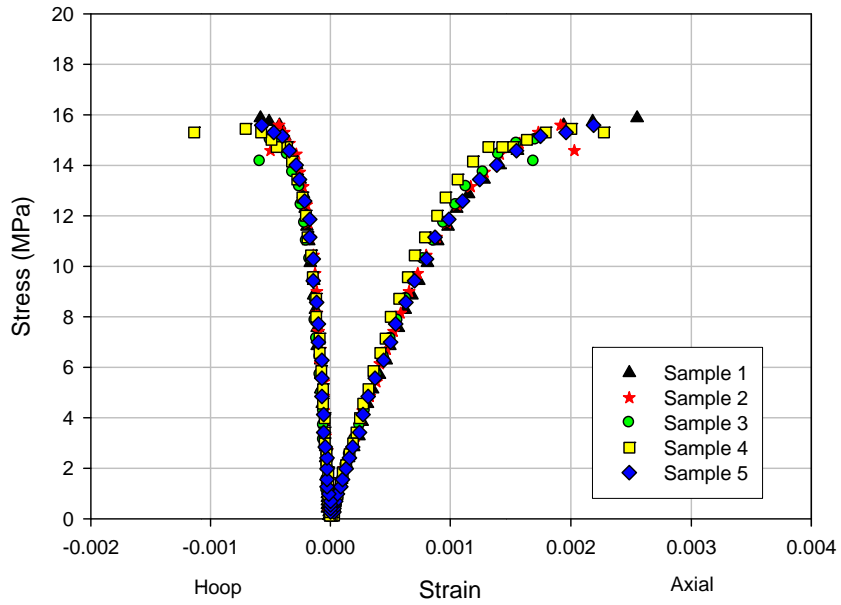


Figure A-1: 30 Days aged unconfined concrete.

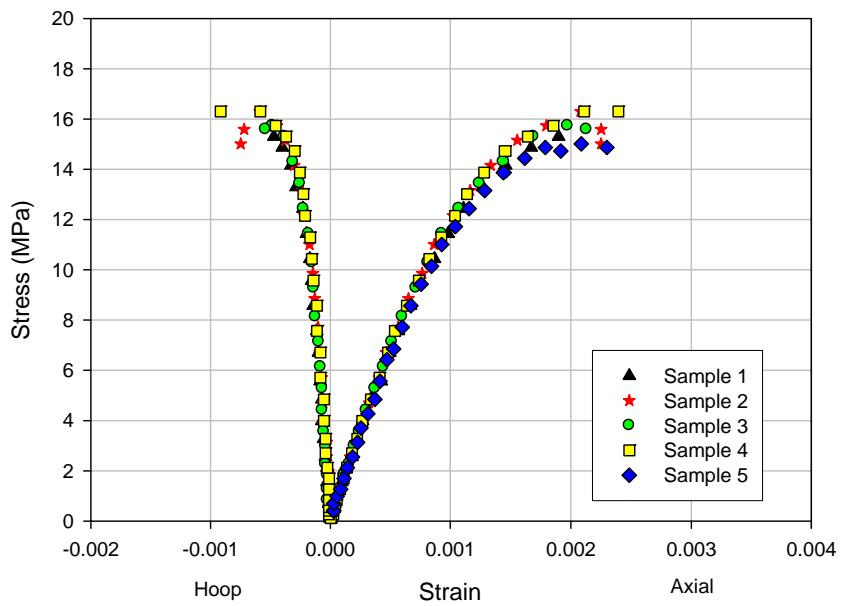


Figure A-2: 100 Days aged unconfined concrete.

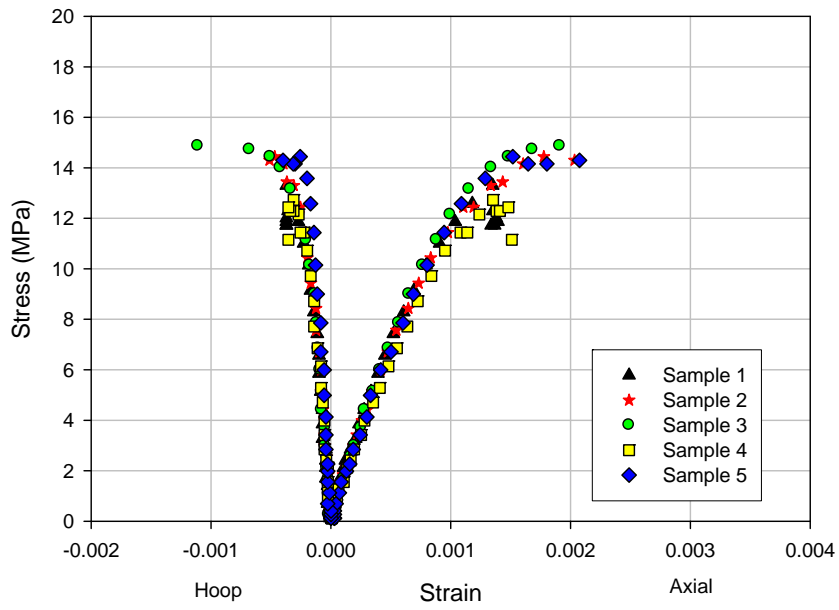


Figure A-3: 300 Days aged unconfined concrete.

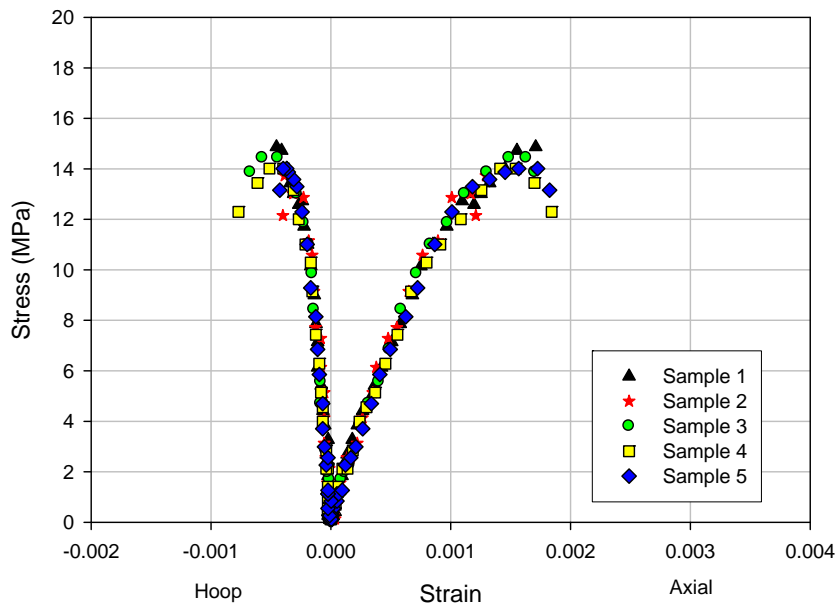


Figure A-4: 500 Days aged unconfined concrete.

Appendix B

COMPOSITE BURST CURVES

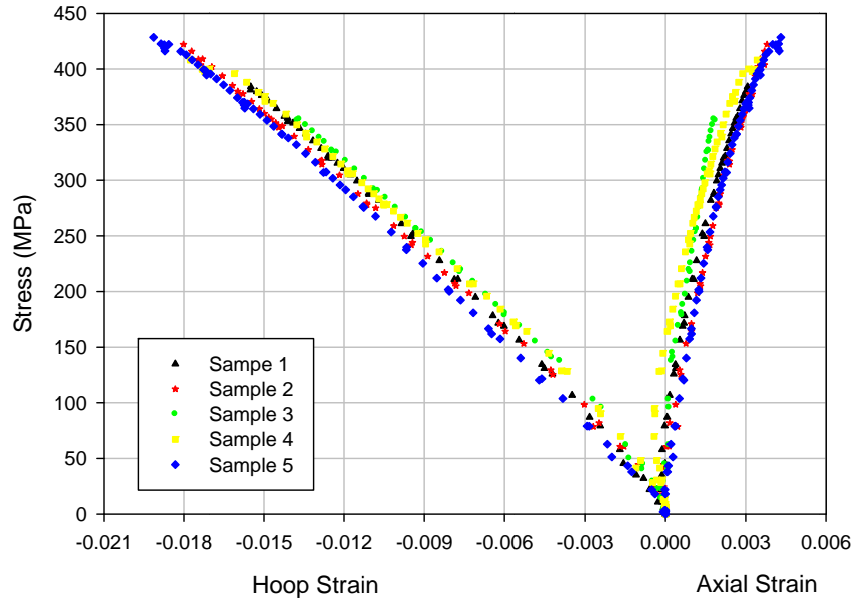


Figure A-5: Burst 10 days 30°C

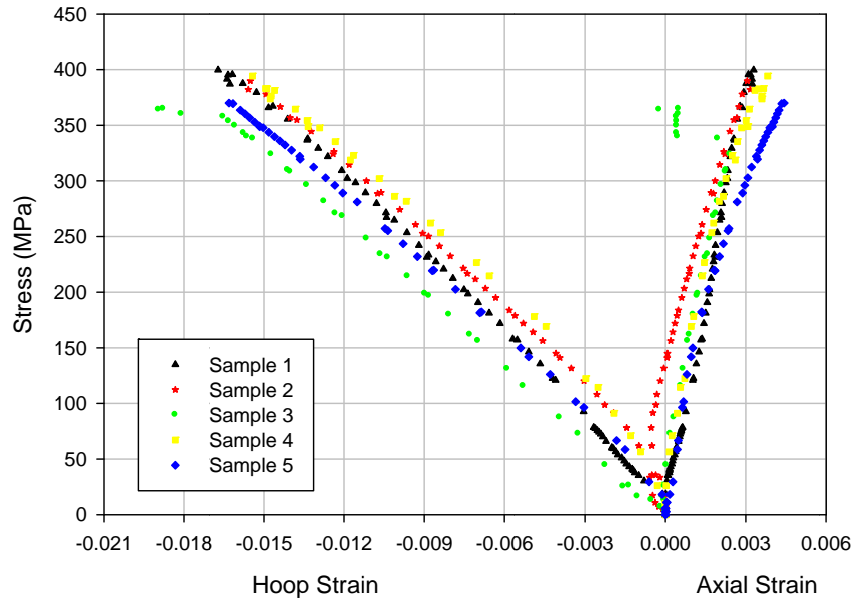


Figure A-6: Burst 100 days base line.

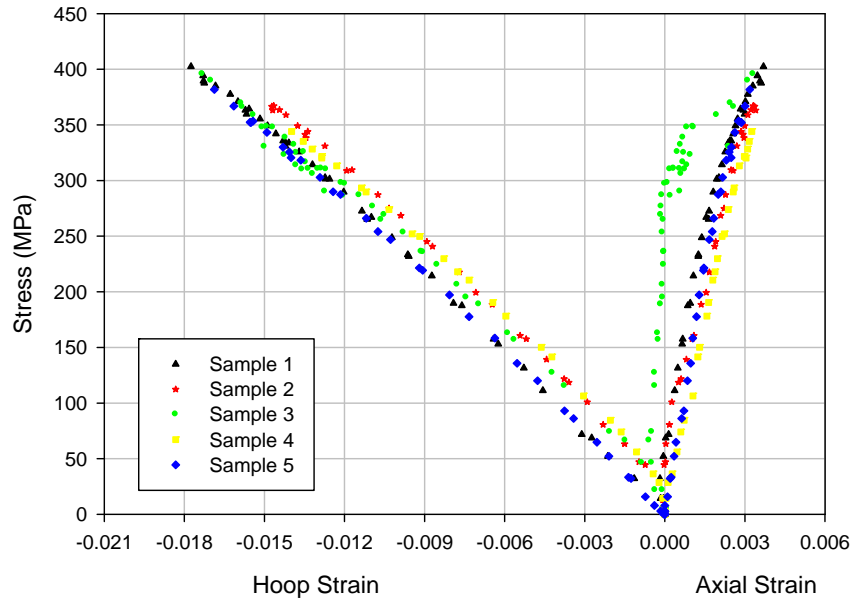


Figure A-7: Burst 100 days 30°C

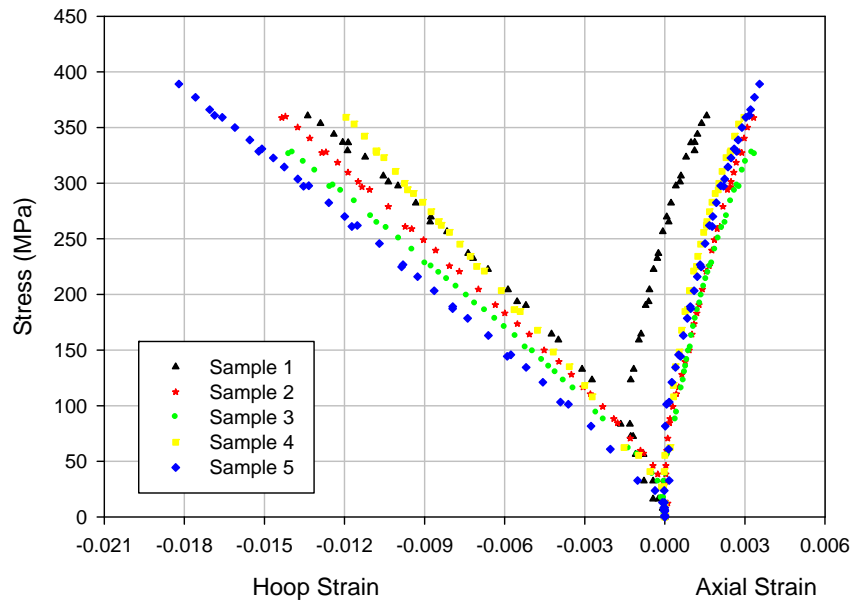


Figure A-8: Burst 100 days 40°C

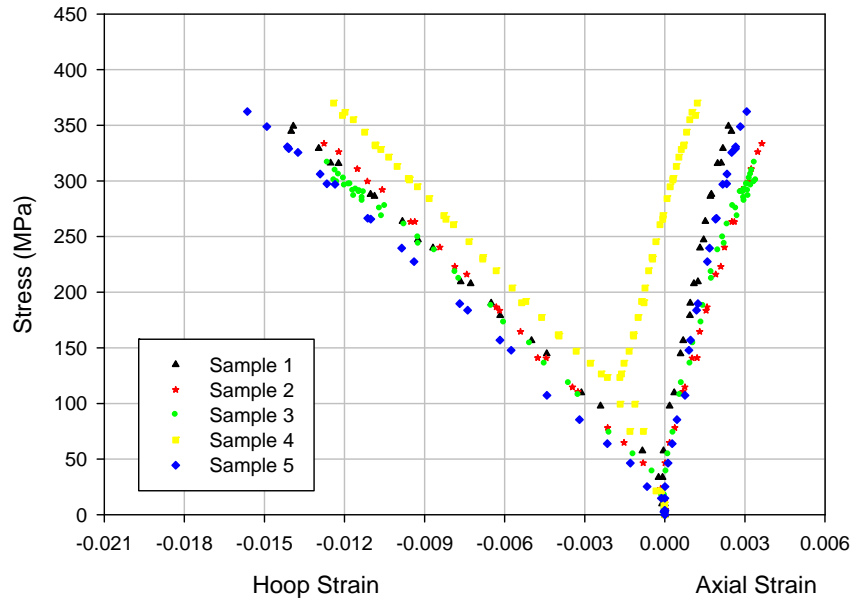


Figure A-9: Burst 100 days 50°C

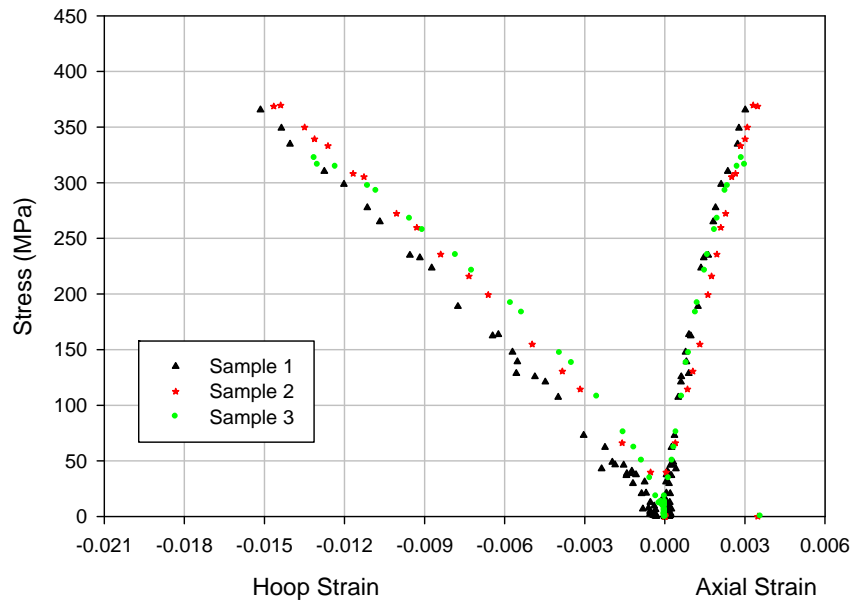


Figure A-10: Burst 300 days 30°C

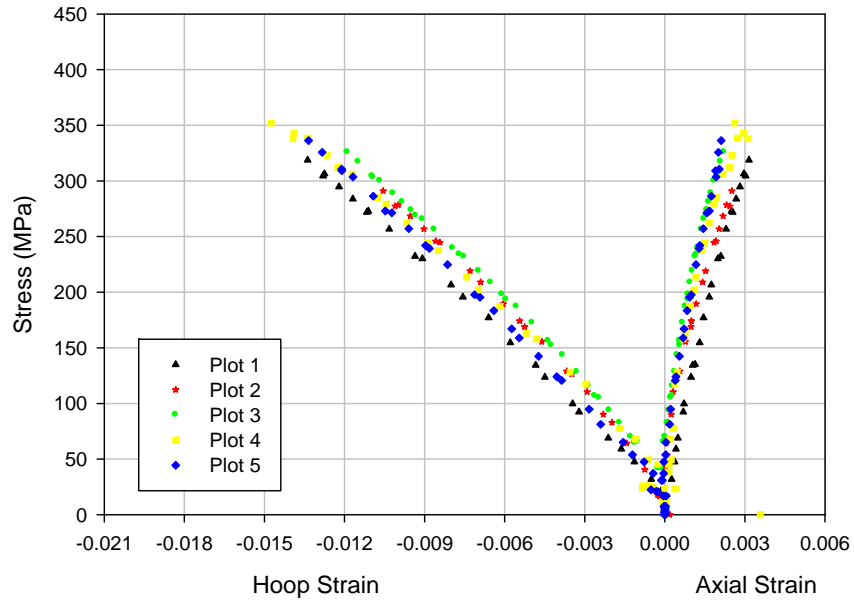


Figure A-11: Burst 300 days 40°C

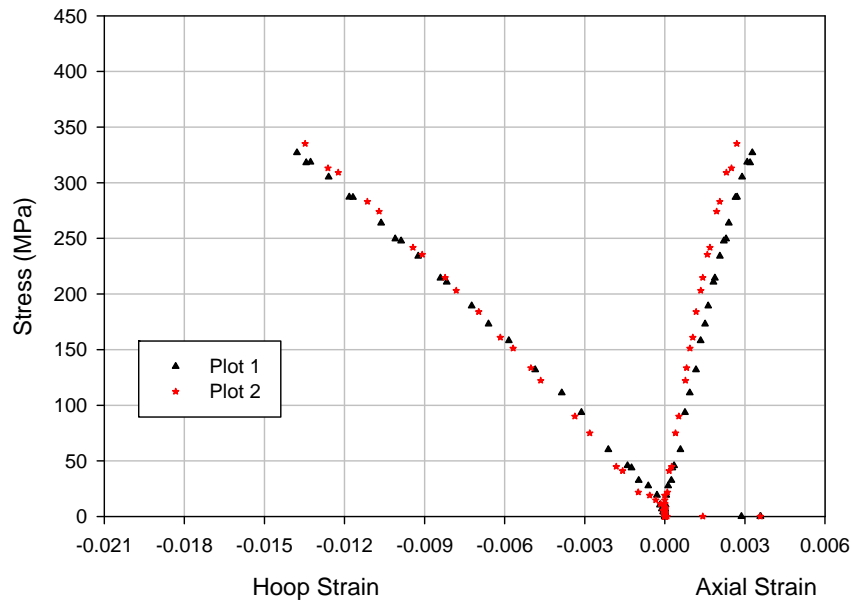


Figure A-12: Burst 300 days 50°C.

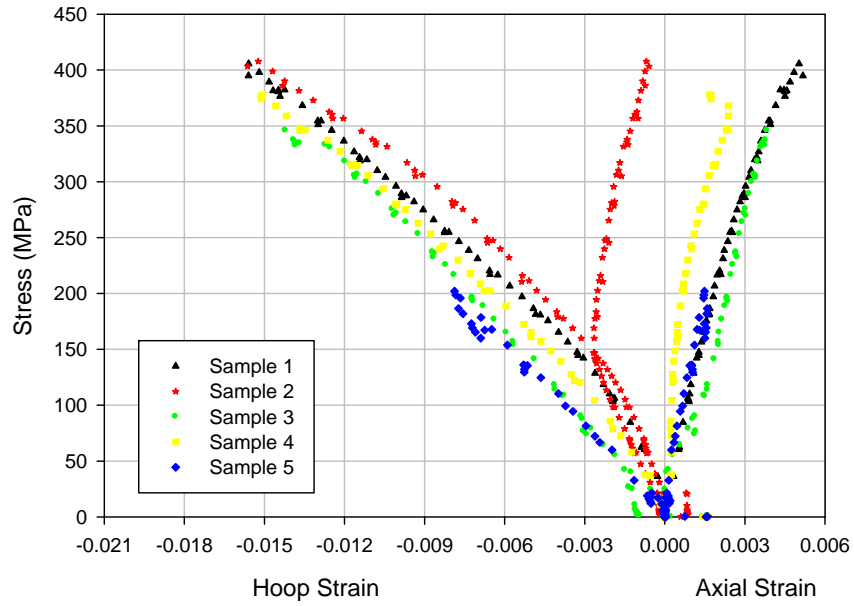


Figure A-13: Burst 500 days base line

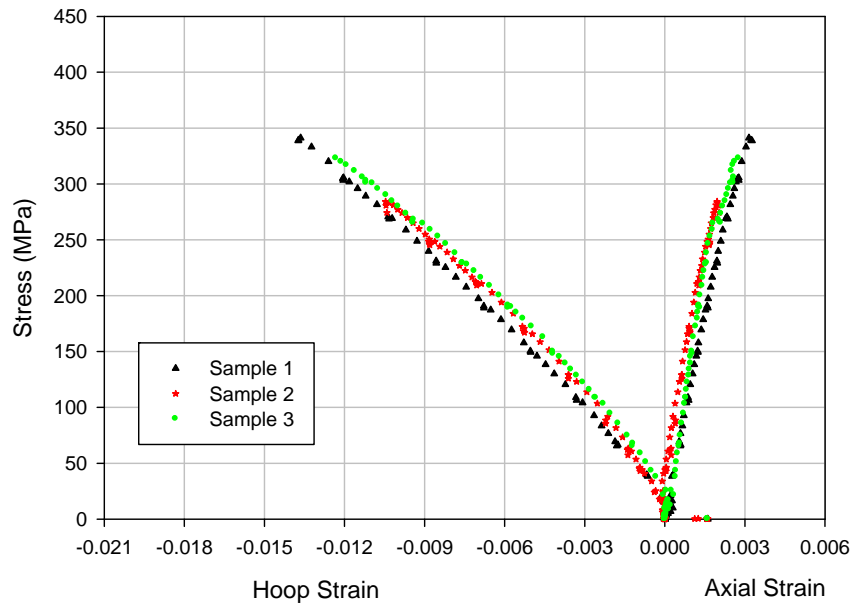


Figure A-14: Burst 500 days 30°C.

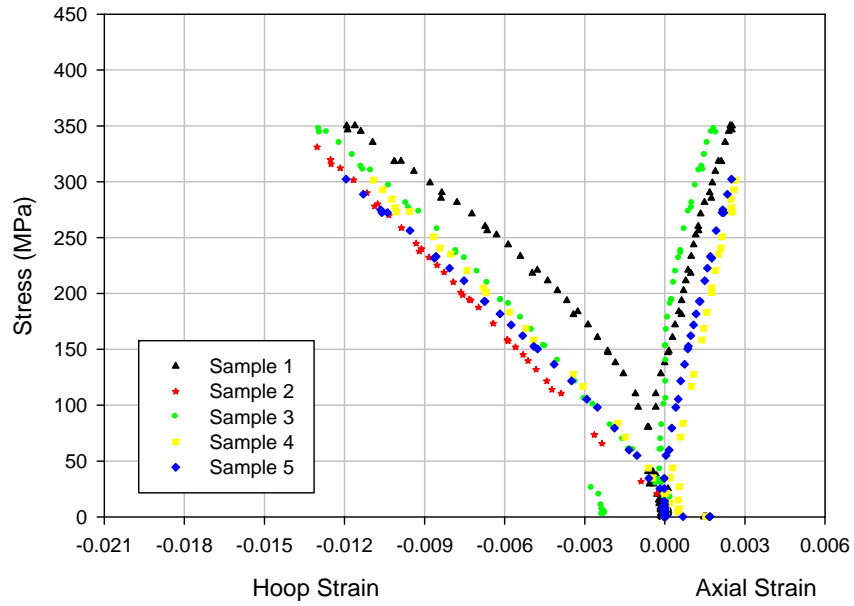


Figure A-15: Burst 500 days 40°C

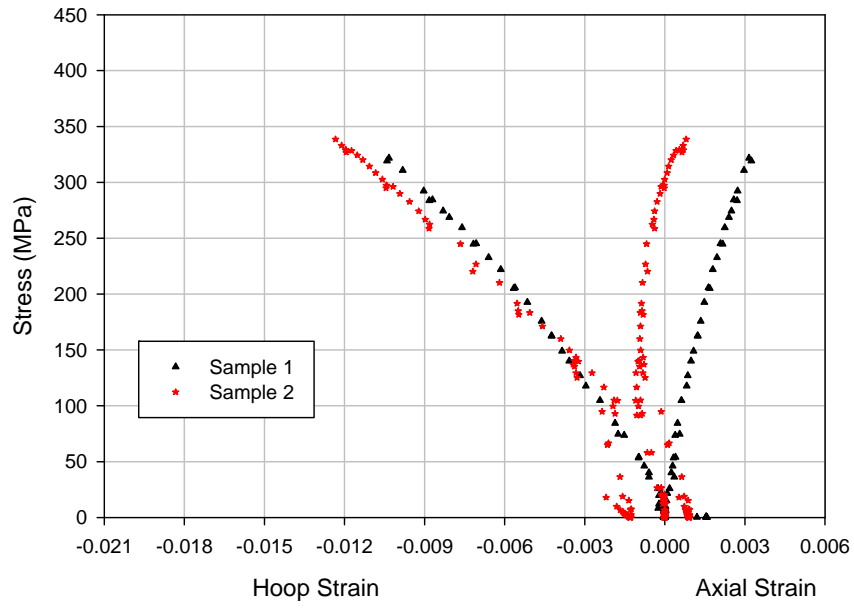


Figure A-16: Burst 500 days 50°C.